



Technische
Universität
Braunschweig



IFAS Institut für Flugantriebe
und Strömungsmaschinen

Master Thesis

Benchmarking Numerical CFD Simulation of Hydrogen Combustion with FLOX[®] based Burner Technology

Nikhil Shinde

Matrikelnummer:- 5180868

Examiner 1: Jun.-Prof. Dr.-Ing. Federica Ferraro
Examiner 2: Prof. Dr.-Ing. Jens Friedrich
Supervisor: M.Sc. Karl Planke

Institut für Flugantriebe und Strömungsmaschinen
Technische Universität Braunschweig
19 April 2024

Declaration of Academic Integrity

Hereby, I, Nikhil Shinde, born on 02 August 1998, declare that I have written the presented thesis independently on my own and without any other resources than the ones indicated. All formulations and concepts taken verbatim or in substance from printed or unprinted material or from the Internet have been cited according to the rules of good scientific practice and indicated by footnotes or other exact references to the original source. This thesis has neither been previously submitted to another authority nor has it been published yet.

A handwritten signature in black ink, reading "N Shinde..", slanted upwards to the right.

Stuttgart, April 19, 2024



Benchmarking Numerical CFD Simulation of Hydrogen Combustion with FLOX® based Burner Technology

Masterthesis

The goal of the thesis is to perform time-averaged 3D CFD simulations with combustion chemistry models in order to benchmark DLR hydrogen combustion simulation tools for further design works. As a case study, existing experimental data of a single nozzle FLOX® based combustor is used. The baseline CFD setup and reference calculations are available. Combustion CFD simulations will be carried out with the DLR finite volume inhouse code THETACom.

After checking modeling plausibility by grid studies, different hydrogen combustion reaction mechanisms are tested for different aspects, including computational efficiency, flame shape and lift-off prediction, and emissions reproduction. This large benchmark study includes well established literature mechanisms and novel DLR mechanisms. Results are to be documented thoroughly.

The work consists of the following steps:

1. Establishment of a time schedule
2. Familiarization with the topics numerical modeling, CFD simulation, and combustion theory and modeling
3. Training based on the software to be used (ANSYS Workbench for preprocessing and grid generation, THETACom for CFD simulation, and suitable post-processing tools)
4. Identification of reference cases for the study from experimental investigation matrix
5. Conduction of grid studies based on reference cases including grid generation
6. Extensive numerical studies with various reaction mechanisms and CFD RANS
 - a. Coverage of different operation points
 - b. Inclusion of sub-models for emissions (NO_x and CO) modeling
 - c. Comparison and validation with experimental data (flame shape and location, emissions)
7. Analysis and documentation of obtained results

This thesis is in cooperation with the DLR Stuttgart in the group of Dr.-Ing. Felix Grimm, where the work will be conducted. Supervision of this thesis will be done by DLR Stuttgart and TU Braunschweig.

Remarks:

The scope and duration of this thesis is based on the currently valid Master's examination regulations for the Computational Sciences in Engineering program at the Technical University of Braunschweig.

The examiners reserve the right to change the task.

Shortly before or after submission of the written work, the results of the work are to be presented to the examiners in a lecture. Date by arrangement (within 2 weeks before or after submission).

Three copies of the thesis remain the property of the participating institutes. The thesis must also be submitted in digital form (PDF file format).

Communication with parties outside the participating ones or with companies about the subject of the work is allowed only with the permission of the undersigned.

A paper that was created in collaboration with a company and is classified as secret may not be stored on the Docoloc server for further plagiarism checking.

Text passages, diagrams, illustrations, numerical values, etc. that have been taken over are to be provided with a complete reference to the source. The *Hinweise für die Anfertigung von studentischen Arbeiten* am IFAS must be considered.

Further agreements between student and institute:

Insofar as the Institute provides me with the Institute's own - expressly designated as confidential - know-how (including drawings, calculations, software) for the purpose of carrying out my study/final thesis, I undertake with my signature to treat this know-how as confidential. Publication and/or utilization of the subject matter of my work, as far as the mentioned know-how is concerned, will only be carried out within the framework of a prior written agreement with the institute and the participating parties.

I will only use the work equipment provided to me for the performance of my work (such as keys) for the intended purpose and will return it promptly and properly upon completion of the work. In particular, I undertake not to make any copies of the software available at the institute for private use during the activities I perform at the institute, to generally make copies only in accordance with the manufacturer's licensing conditions, and to observe the statutory provisions on copyright protection. Furthermore, I will not store any data made accessible to me by the institute in the course of my work on private data carriers.

I am aware that the work to be submitted by me and, if applicable, further copies are usually placed in the institute library or university library and are thus publicly accessible. In case of justified interest (e.g., patent application), the institute will, if I submit a written request in due time beforehand, defer the first publication of my work until a date to be agreed upon with the institute. If, in an exceptional case, this should not be possible, I will be informed of this in writing by the Institute without delay, together with an appropriate justification.

I grant all the parties involved the right to use the results of my work for research and teaching purposes. In this context, I agree to make available to the Institute for inspection and copying all documents, materials, laboratory tests and interim results produced in the course of my work - insofar as these are necessary for the understanding and comprehensibility of my work - as well as software and software listings, including the source code. In case of utilization of my work results in the

copyright sense (e.g., distribution, duplication, further development), I will be designated as the author by mentioning my name, unless I explicitly waive this right.

Braunschweig, 18th September 2023



Jun.-Prof. Dr.-Ing. Federica Ferraro

DLR Stuttgart



M.Sc. Karl Planke



Dr.-Ing. Felix Grimm



Signature of the student

Date of release: 04th October 2023

Date of submission: 19th April 2024

Abstract

Hydrogen is a promising alternative to fossil fuels for future gas turbines, since it can be produced using renewable energy sources and benefits from CO₂ free combustion. However, due to its higher reactivity (when compared to natural gas) it cannot be used with the state-of-the-art premixed combustors optimized for natural gas. Besides the risks of flame flashback and auto-ignition, high hydrogen content fuels tend to produce significantly elevated NO_x emissions due to the higher flame temperature. To seamlessly incorporate hydrogen into gas turbine technology, it is essential to develop advanced combustion solutions that ensure both low emissions and operational reliability. This thesis investigates the combustion dynamics of a single-nozzle FLOX[®] burner under fuel and load flexibility investigations, focusing on hydrogen content and premixing strategies. The goal is to benchmark DLR's hydrogen combustion simulations by validating RANS models against experimental data. To ensure the accuracy and reliability of the computational model, a mesh dependence study was conducted by leveraging the GCI methodology, which also helped identify the optimal mesh refinement level within the reaction zone. Results from RANS simulations offer a detailed comparative analysis, revealing that varying hydrogen volume fraction from 0 to 100vol.% H₂ at constant equivalence ratio and thermal power significantly diminishes LOH, resulting in more compact and anchored flames, while premixed configurations enhance flame stability and reduce LOH compared to non-premixed cases, providing a potential approach for NO_x mitigation. Leaner mixtures result in lower NO_x emissions due to reduced flame temperatures. Analysis of velocity fields demonstrates the influence of LF, FF and premixing on flow recirculation zone and jet stabilization. Temperature distributions highlight the location of reaction zones and illustrate that premixing leads to early combustion onset and yields more compact reaction zones, suggesting the potential to design compact combustors with a broad operability range. While RANS simulations effectively verify trends in emissions and LOH, they may underestimate flame width near the lean blow-off limit, recognizing certain limitations.

Keywords: FLOX[®], load flexibility, fuel flexibility, hydrogen combustion, gas turbine, NO_x emissions, Lift-off height(LOH)

Kurzfassung

Wasserstoff ist eine vielversprechende Alternative zu fossilen Brennstoffen für zukünftige Gasturbinen, da er aus erneuerbaren Energiequellen hergestellt werden kann und eine CO₂-freie Verbrennung ermöglicht. Aufgrund seiner höheren Reaktivität (im Vergleich zu Erdgas) kann er jedoch nicht uneingeschränkt in heutigen, für Erdgas optimierten Vormischbrennern, für Erdgas entwickelten Vormischbrennern verwendet werden. Neben eines Flammenrückschlags oder einer unkontrollierten Selbstentzündung führen Brennstoffe mit hohem Wasserstoffgehalt aufgrund der höheren Flammentemperatur tendenziell zu deutlich erhöhten NO_x-Emissionen. Um Wasserstoff nahtlos in die Gasturbinentechnologie einzubinden, müssen fortschrittliche Verbrennungslösungen entwickelt werden, die sowohl niedrige Emissionen als auch Betriebssicherheit gewährleisten. In dieser Arbeit wird die Verbrennungsdynamik eines eindüsigen FLOX[®]-Brenners hinsichtlich Brennstoff- und Lastflexibilität untersucht, wobei der Schwerpunkt auf dem Wasserstoffgehalt sowie verschiedenen Vormischungsstrategien liegt. Ziel ist es, die Wasserstoffverbrennungssimulationen des DLR auf Basis von RANS-Modellen durch den Vergleich mit experimentellen Daten zu validieren. Um die Genauigkeit und Zuverlässigkeit des Berechnungsmodells zu gewährleisten, wurde eine Studie zur Gitterabhängigkeit unter Verwendung der GCI-Methodik durchgeführt, wodurch der optimale Gitterverfeinerungsgrad innerhalb der Reaktionszone ermittelt werden konnte.

Die Ergebnisse der durchgeführten RANS-Simulationen bieten eine detaillierte vergleichende Analyse und zeigen, dass die Steigerung des Wasserstoffanteils im Brennstoff von 0 bis 100% H₂ bei konstantem Äquivalenzverhältnis und thermischer Leistung zu kompakteren und weniger abgehobenen Flammen führt. Im Weiteren verbessern vorgemischte Konfigurationen die Flammenstabilität und verringern die Abhebehöhe im Vergleich zu nicht vorgemischten Fällen, was einen potenziellen Ansatz zur NO_x-Minderung darstellt. Magerere Gemische führen aufgrund der geringeren Flammentemperaturen zu niedrigeren NO_x-Emissionen. Die Analyse der Geschwindigkeitsfelder zeigt den Einfluss von Last, Brennstoff und Vormischung auf die Strömungsrezirkulationszone und die Jetstabilisierung. Die Temperaturverteilungen verdeutlichen die Lage der Reaktionszonen und zeigen, dass die Vormischung zu einem früheren Verbrennungsbeginn führt und kompaktere Reaktionszonen ergibt, was auf das Potenzial zur Konstruktion kompakter Brennkammern mit einem breiten Betriebsbereich hindeutet. Während RANS-Simulationen die Trends bei den Emissionen und der Abhebehöhe effektiv vorhersagen können, sind insbesondere hinsichtlich der Unterschätzung der Flammenausbreitung" in der Nähe der mageren Verlöschgrenze gewisse Einschränkungen erkennbar.

Schlüsselwörter: FLOX[®], Lastflexibilität, Brennstoffflexibilität, Wasserstoffverbrennung, Gasturbine, NO_x-Emissionen, Abhebehöhe

Acknowledgment

A great deal of appreciation is extended to my supervisor, Mr. Karl Planke and Dr.-Ing. Felix Grimm from DLR Institute of Combustion Technology (VT) at Stuttgart, for giving me such a remarkable opportunity to work on this challenging topic for my Masters thesis. This work would never be possible without their continuous guidance and support.

I would like to express my gratitude to Jun.-Prof. Dr.-Ing. Federica Ferraro and Prof. Dr.-Ing. Jens Friedrich for being a part of my thesis committee. Also, I would like to thank the colleagues from MGT-BKA, who supported me with their knowledge and always gave me advice when I had questions during meetings.

In addition to my supervisors, I would like to take this opportunity to express my appreciation to Professor Dr. Andreas Huber, the head of the Institute and Dr. Peter Kutne, head of the MGT Department, for providing the necessary resources to carry out this research.

My deepest thanks to my parents for believing and supporting me during my Masters studies at TU Braunschweig. Finally, I want to thank my friends for their help, love, and care during my Masters studies.

Nikhil Shinde
Stuttgart, April 2024

Contents

Task description	viii
Abstract	xiii
Nomenclature	xv
List of Figures	xxiii
List of Tables	xxiv
1 Introduction	1
1.1 Motivation	1
1.2 Objectives and Scope	3
1.3 Literature survey and previous studies	4
1.4 Structure of the Thesis	6
2 Fundamentals of Combustion modelling	7
2.1 Governing Equations for Compressible Reactive Flows	7
2.2 Turbulence modelling	9
2.2.1 The k - ε Turbulence Model	12
2.2.2 The k - ω Turbulence Model	13
2.3 Combustion modelling	16
2.3.1 Modes of Combustion	17
2.3.2 Turbulent Premixed Combustion	17
2.3.3 Pollutant Formation	19
2.3.4 Chemical reaction kinetics	20
2.3.5 Modelling of the Chemical Source Term	21
2.4 Spatial and Temporal Discretization	23
2.5 Numerical flow and combustion code - ThetaCOM	25
3 Single-nozzle FLOX[®] burner	27
3.1 Combustor Design	27
3.1.1 Operational Principles	27
3.1.2 Flame Stabilisation	29
3.2 Hydrogen as a gas turbine fuel	32
3.2.1 Thermophysical properties	32
3.2.2 Fundamental flame characteristics	33
3.2.3 Standardization of NO _x emissions	35
3.3 Effects on combustion stability	36
3.3.1 Lean blow-off	36

3.3.2	Flame Flashback	37
3.3.3	Dynamic instabilities	38
4	Numerical model description	40
4.1	Computational domain	40
4.2	Operating conditions	41
4.3	Mesh generation	43
4.3.1	Unstructured meshing for reactive flows	43
4.3.2	Meshing procedure	43
4.3.3	Quality criteria	44
4.4	Simulation workflow	45
4.5	Mesh dependence study	46
4.5.1	Grid Convergence Index	46
4.5.2	Graphical illustration and flow visualization	51
5	Results and Discussion	56
5.1	Flame Shape and Lift-off Height	56
5.1.1	Qualitative evaluation	56
5.1.2	Quantitative Evaluation	60
5.2	Quantitative analysis of NO _x emissions	62
5.2.1	Variations in NO _x emissions relative to hydrogen volume fraction	62
5.2.2	Variations in NO _x emissions relative to Equivalence Ratio	63
5.2.3	Relation between NO _x and CO emissions	64
5.3	Flow recirculation and velocity profiles	66
5.3.1	Streamlines and velocity field	66
5.3.2	Velocity profiles for fuel flexibility investigations	69
5.4	Evaluation of Temperature field	70
6	Summary and outlook	74
	Bibliography	87
A.1	Parameter file structure	88
A.1.1	Parameter file for phase 6	88
A.1.2	Boundary mapping file	90
A.2	Contour plots	92
A.3	Tecplot macros	94
A.3.1	Post-processing script for NO _x emissions	94
A.3.2	Line of sight integration to visualize OH*-CL	95
	Appendix	88

Nomenclature

Latin Symbols

Symbol	Meaning	Unit
A	Empirical Combustion model constant	-
a_1	Constant of the k - ω SST turbulence model	-
A_r	Arrhenius prefactor	<i>variable</i>
B	Empirical combustion model constant	-
c	Speed of sound	m/s
C_1, C_2	Constants of the Standard k - ε turbulence model	-
$CD_{k\omega}$	Cross-Diffusion term of the k - ω turbulence model	-
c_p	Specific heat capacity at constant pressure	$J/(kgK)$
C_μ	Constant of the Standard k - ε turbulence model	-
C_τ	Constant of the EDC combustion model	-
C_ζ	Constant of the EDC combustion model	-
\underline{D}	Diffusion coefficient	m^2/s
D_k	Diffusion of turbulent kinetic energy	m^2/s
D_t	Turbulent diffusion coefficient	m^2/s
e^a	Approximate relative error	-
$E_{\alpha,r}$	Activation energy for reaction r	J/kg
\mathbf{F}	Cartesian flux vector	<i>variable</i>
\mathbf{f}	Vector of external forces	m/s^2
f	Frequency	$1/s$
f	Autocorrelation function	-
F_1, F_2	Blending functions of the k - ω SST turbulence model	-
\mathbf{G}_Ω	Flux vector normal to the cell surface	<i>variable</i>
\mathbf{G}_k	Mean flux vector	<i>variable</i>
h	Specific enthalpy	J/kg
$h^0_{f,\alpha}$	Standard formation enthalpy, species α	J/kg
\mathbf{I}	Identity matrix	-
\underline{j}	Diffusion mass flux	$kg/(m^2 s)$
k	Turbulent kinetic energy	m^2/s^2

k_b	Rate constant of the backward reaction	$1/s$
k_f	Rate constant of the forward reaction	$1/s$
L_t	Turbulent timescale	s
l_t	Turbulent length scale	m
M_α	Molar mass of a species	kg/mol
\dot{m}	Mass flow rate	kg/s
M_{tr}^*	Transfer rate of the EDC model	$1/s$
n	Dimension	-
n_i	Surface normal vector	-
N_r	Number of elementary reactions	-
N_s	Number of species in the mixture	-
O	Order	-
\mathbf{P}	Iteration matrix	<i>variable</i>
p	Pressure	Pa
p_{abs}	Absolute Pressure	Pa
p_{ref}	Reference Pressure	Pa
P_k	Production of Turbulent Kinetic Energy	$kg/(m \cdot s^3)$
\tilde{P}_k	Production Term in the k - ω SST Turbulence Model	$kg/(m \cdot s^3)$
P_{therm}	Thermal Power	W
R	Specific Gas Constant	$J/(kg \cdot K)$
\dot{R}_α	Mass Transfer Rate of Species α	$kg/(m^3 s)$
RH	Reaction Heat/Integrated Heat Release/Thermal Power	J/s
R_m	Universal Gas Constant	$J/(mol \cdot K)$
RR_r	Reaction Rate of Reaction r	$mol/(m^3 s)$
S_α	Chemical Source Term	$kg/(m^3 s)$
S_{ij}	Strain rate Tensor	$1/s$
S_L^0	Local Flame speed	m/s
T	Temperature	K
T_0	Temperature under atmospheric reference conditions	K
t	Time	s
\mathbf{u}	Velocity vector	m/s
U_t	Turbulent velocity scale	m/s
u, v, w	Velocity components	m/s
V	Control volume/Cell volume	m^3
V	Velocity magnitude	m/s
x, y, z	Cartesian coordinates	m
y	Wall distance in the k - ω SST turbulence model	m
\mathbf{Y}_α	Species vector	-
Y_α	Mass fraction of species α	-
Y_α^*	Mass fraction of species α within the fine structures	-

Greek Symbols

Symbol	Meaning	Unit
α	Species index	-
α	Constant of the k - ω SST turbulence model	-
α_1	Constant of the k - ω SST turbulence model	-
α_2	Constant of the k - ω SST turbulence model	-
β	Constant of the k - ω SST turbulence model	-
β_1	Constant of the k - ω SST turbulence model	-
β_2	Constant of the k - ω SST turbulence model	-
β^*	Constant of the k - ω SST turbulence model	-
β_r	Temperature exponent	-
Γ	Gamma function	-
Δx	Grid spacing	m
Δt	Time step	s
ε	Turbulent dissipation rate	m^2/s^2
ζ^*	Parameter of the EDC combustion model	-
λ	Thermal conductivity	$W/(mK)$
λ_t	Turbulent thermal conductivity	$W/(mK)$
μ	Dynamic viscosity	$kg/(m \cdot s)$
μ_t	Turbulent dynamic viscosity	$kg/(m \cdot s)$
ν	Kinematic viscosity	m^2/s
ν_t	Turbulent kinematic viscosity	m^2/s
$\nu'_{\alpha,r}, \nu''_{\alpha,r}$	Stoichiometric coefficients, reactant ('), product ('')	-
ρ	Density	kg/m^3
σ	Constant of the k - ω SST turbulence model	-
σ^*	Constant of the k - ω turbulence model	-
σ_{k1}	Constant of the k - ω SST turbulence model	-
σ_{k2}	Constant of the k - ω SST turbulence model	-
σ_ε	Constant of the Standard k - ε turbulence model	-
σ_ω	Constant of the k - ω SST turbulence model	-
$\sigma_{\omega 1}$	Constant of the k - ω SST turbulence model	-
$\sigma_{\omega 2}$	Constant of the k - ω SST turbulence model	-
$\underline{\underline{\tau}}$	Shear stress tensor	N/m^2
τ_{ign}	Ignition delay time	s
τ_m	Timescale of the mean flow field	s
τ_t	Turbulence timescale	s
τ^*	Timescale of the fine structures	s
Φ	Equivalence ratio	-
ϕ	Arbitrary flow quantity	<i>variable</i>

π	Pi (mathematical constant)	-
ω	Turbulent frequency	$1/s$
Ω	Cell surface area	m^2
Ω_{ij}	Rotation tensor	-

Indices and Accents

Index/Accent	Meaning
ϕ	Parameter
ϕ_0	Reference state
ϕ_{abs}	Absolute value
ϕ_{initial}	Initial condition
ϕ_{α}	Species
ϕ_b	Backwards
ϕ_{fuel}	Fuel
ϕ_f	Forwards
ϕ_{air}	Air
ϕ_{max}	Maximum value
ϕ_{min}	Minimum value
ϕ_{mod}	Modification
ϕ_r	Elementary reaction
ϕ_{ref}	Reference
ϕ_{stoich}	Stoichiometric ratio
ϕ_t	Turbulence-related quantity
ϕ^*	Dimensionless
$\overline{\phi}$	Mean of a Reynolds-decomposed quantity
$\tilde{\phi}$	Mean of a Favre-decomposed quantity
ϕ'	Fluctuation of a Reynolds-decomposed quantity
ϕ''	Fluctuation of a Favre-decomposed quantity

Operators

Operator	Meaning
ϕ	Scalar
$\boldsymbol{\phi}$	Vector
$\underline{\underline{\phi}}$	Matrix
$\frac{\partial \phi}{\partial x}$	Partial derivative of ϕ with respect to x

$\frac{D\phi}{Dt}$	Material derivative of ϕ with respect to time t
$\int \phi dV$	Integral of ϕ over the volume V
$\int \phi dx$	Integral of ϕ over x
$\sum_{i=1}^n \phi$	Sum of ϕ from $i = 1$ to $i = n$
$\prod_{i=1}^n \phi$	Product of ϕ from $i = 1$ to $i = n$
$\phi \cdot \psi$	Dot product of ϕ and ψ
$\phi \otimes \psi$	Dyadic product of ϕ and ψ
$\underline{\underline{\phi}} : \underline{\underline{\psi}}$	Frobenius inner product of $\underline{\underline{\phi}}$ and $\underline{\underline{\psi}}$
$\nabla \phi$	Gradient of ϕ
$\nabla \cdot \phi$	Divergence of ϕ
$\exp(\phi)$	Exponential function of ϕ
$\max(\phi, \psi)$	Maximum of ϕ and ψ
$\min(\phi, \psi)$	Minimum of ϕ and ψ
$\tanh(\phi)$	Hyperbolic tangent of ϕ

Dimensionless Numbers

Notation	Number
Da	Damköhler Number
Ka	Karlovitz Number
Pr, Pr_t	Prandtl Number, Turbulent Prandtl Number
Re_t, Re_{lt}	Reynolds Number(s)
Sc, Sc_t	Schmidt Number, Turbulent Schmidt Number

Chemical Formulae

Symbol	Meaning
H_2	Hydrogen
N_2	Nitrogen
NO	Nitrogen Monoxide
NO_2	Nitrogen Dioxide
N_2O	Dinitrogen Oxide
O_2	Oxygen
NO_x	Aggregate of nitric oxides NO and NO_2
OH	Hydroxyl Radical (molecular form)
CO_2	Carbon Dioxide
CO	Carbon Monoxide

Abbreviations

Abbreviation	Meaning
ATM	Atmosphere
BOI	Body of Influence
BLI	Boundary Layer Inflation
CDS	Central Difference Scheme
CFD	Computational Fluid Dynamics
CIVB	Combustion-Induced Vortex Breakdown
CPU	Central Processing Unit
DC1S30N18	DLR Concise Reaction Mechanism, specific variant for mixtures of methane and hydrogen as fuel
DLR	Deutsches Zentrum für Luft-und Raumfahrt
DNS	Direct Numerical Simulation
EDC	Eddy Dissipation Concept
EDM	Eddy Dissipation Model
EU	European Union
FDM	Finite Difference Method
FF	Fuel Flexibility
FP	Fully Premixed
FLOX [®]	Flameless Oxidation
FRC	Finite Rate Chemistry
FVM	Finite Volume Method
GCI	Grid Convergence Index
GMRES	Generalised Minimal RESidual
IRZ	Inner Recirculation Zone
LBO	Lean blow-off
LDS	Linear Difference Scheme
LES	Large Eddy Simulation
LF	Load Flexibility
LHV	Lower Heating Value
LOH	Lift-off Height
LOS	Line of Sight
LRZ	Lower Recirculation Zone
MILD	Moderate or Intense Low oxygen Dilution
MGT	Micro Gas Turbine
NP	Non Premixed
NS	Navier-Stokes
PBCGS	Preconditioned Bi-Conjugate Gradient Stabilised
QUDS	Quadratic Upwind Difference Scheme

RANS	Reynolds-Averaged Navier-Stokes
RH	Reaction Heat
RNG	Renormalization Group
RSM	Reynolds Stress Model
SIMPLE	Semi-Implicit Method for Pressure-Linked Equations
THETA	Turbulent Heat Release Extension of the TAU code
SST	Shear Stress Transport
TP	Technically Premixed
UDS	Upwind Difference Scheme
UHC	Unburnt Hydrocarbons
URANS	Unsteady Reynolds-Averaged Navier-Stokes
VT	Institut für Verbrennungstechnik/ Institute of Combustion Technology, DLR Stuttgart

List of Figures

1.1	Germany’s energy consumption by annual share of fuel in 2022 (left) and Electricity generation (right) reported by AG Energiebilanz [1]	1
2.1	Comparison of laminar and turbulent flows	9
2.2	Comparison of the original and Reynolds-averaged flow	10
2.3	Turbulent kinetic energy spectrum vs. Wave number	11
2.4	Borghis and Peters regime diagram	18
2.5	Dependence of emissions on Adiabatic Flame Temperature. Adapted from	20
2.6	Two-dimensional geometrical overview of the dual grid (details available in [2]) used by ThetaCOM	24
3.1	Schematics of the single-nozzle combustor set-up	28
3.2	Swirl-stabilized combustor schematic [3]	30
3.3	Schematic of the jet-stabilized FLOX [®] burner principle [4]	30
3.4	Laminar flame speed comparison of pure and blended CH ₄ and H ₂ at various equivalence ratios at 300 K and 1 atm in air. Points are experimental data, and lines are from the kinetics model, adapted from [5,6]	34
3.5	Adiabatic flame temperature of different fuels in air at 1 atm, adapted from [7]	35
4.1	Computational domain in 3D for the single-nozzle FLOX [®] burner (Technically Premixed configuration), illustrating the applied boundary conditions	41
4.2	Computational mesh for the flow domain (Technically Premixed configuration). The visualization is done on a sectional mid-plane, and the zoom box on the right signifies mesh generated on the inlet.	44
4.3	ThetaCOM simulation workflow with three stages concerning the reactivity of the flow: cold flow, EDM and FRC, with each stage consisting of two phases, implemented by the use of six subsequent parameter files	46
4.4	Convergence behaviour of NO _x emission at the outlet for a range of meshes and operating conditions. Y-axis is the NO _x values and X axis represents the iterations.	51
4.5	Velocity magnitude comparison at 1D probes along combustor width for FF and LF investigations across different mesh resolutions. The figure (b) alongside illustrates the 1D probes selected for extracting and monitoring CFD data.	52
4.6	Temperature distribution along the combustor length for FF and LF investigations at different mesh resolutions.	53
4.7	Mass fraction of OH along the combustor length for FF and LF investigations, showcasing mesh convergence.	53
4.8	OH*-CL visualisation for TP configuration (0 and 100 vol.% H ₂) across different mesh resolutions. LOH of the experimental results are compared with simulations.	54

4.9	Flow field characteristics in TP configuration, showcasing different mesh resolutions for 100 vol.% H ₂ and $\Phi = 0.74$	55
5.1	OH*-CL comparison of simulation and experiment dataset showcasing NP configuration. Left: FF, variation in H ₂ vol.%. Right: LF, variation in $\Phi = 0.49-0.21$	57
5.2	OH*-CL comparison of simulation and experiment dataset showcasing for TP configuration. Left: FF, variation in H ₂ vol.%. Right: LF, variation in $\Phi = 0.49-0.21$	58
5.3	OH*-CL comparison of simulation and experiment dataset showcasing for FP configuration. Left: FF, variation in H ₂ vol.%. Right: LF, variation in $\Phi = 0.49-0.30$	59
5.4	Quantitative representation of flame LOH for FF investigations.	60
5.5	Mass fraction of OH along the combustor length for FF investigations, showcasing the trend in different configurations.	61
5.6	NO _x emissions in parts per million (ppm) as a function of hydrogen volume percentage for NP, FP, and TP configurations. The solid lines represent simulation data and dashed lines are the experimental data.	62
5.7	NO _x emissions in parts per million (ppm) as a function of equivalence ratio (Φ) for NP, FP, and TP configurations. The solid lines represent simulation data and dashed lines are the experimental data.	63
5.8	NO _x and CO emissions versus vol. %H ₂ for NP, TP, and FP configurations.	64
5.9	Flow field characteristics in FP configuration, showcasing the effect of varying vol.% H ₂ and equivalence ratio (Φ) on recirculation zones and velocity magnitude near the nozzle exit.	66
5.10	Flow field characteristics in TP configuration, showcasing the effect of varying vol.% H ₂ and equivalence ratio (Φ) on recirculation zones and velocity magnitude near the nozzle exit.	67
5.11	Flow field characteristics in NP configuration, showcasing the effect of varying vol.% H ₂ and equivalence ratio (Φ) on recirculation zones and velocity magnitude near the nozzle exit.	68
5.12	Velocity profiles at axial distances of 0.1D, 7.5D and 15D for FF investigation on NP, TP and FP configurations. The x-axis represents the combustor width, and the y-axis represents the velocity magnitude.	69
5.13	Temperature distribution for NP, TP, and FP configurations at varying vol.% H ₂	71
5.14	Contours of temperature distribution in NP, TP, and FP configurations under FF and LF investigations.	72
A.1	Flow field characteristics in TP configuration, showcasing different mesh resolutions for the 100 vol.% H ₂ and $\Phi = 0.3$ scenario.	92
A.2	OH*-CL visualisation for TP configuration (60vol.% H ₂ on left and 100vol.% H ₂ on right) across different mesh resolutions. LOH of the experimental results are compared with simulations. The fines meshes are unable to model LOH for leaner conditions.	92
A.3	Contours of heat release in NP, TP, and FP configurations under FF and LF investigations.	93

List of Tables

2.1	Model constants of the Standard $k-\varepsilon$ Model	13
2.2	Model constants of the Standard $k-\omega$ Model	14
2.3	Model constants of the $k-\omega$ SST Model	15
2.4	Zeldovich Mechanism [8]	19
3.1	Fuel properties of hydrogen, natural gas, and methane [9–11]	32
4.1	Operating conditions for the investigation on FF and LF at atmospheric pressure. Specification of \dot{m}_{FP} is the mass flow rate for the FP configuration and \dot{m}_{fuel} , \dot{m}_{air} is valid for both NP and TP	42
4.2	The refinement factor and corresponding mesh resolutions with cell count. Where $h = 0.49028 \times a$	47
4.3	Relative Error and Grid Convergence Index (GCI) for FF and LF. The variable under consideration is Temperature (in K) probed at the outlet surface	49
4.4	Relative Error and Grid Convergence Index (GCI) for 5 different mesh resolutions under FF and LF investigations. The variable under consideration is NO_x (in ppm) probed at the outlet surface (refer subsection A.3.1).	50

Chapter 1

Introduction

1.1 Motivation

World energy consumption is projected to grow by about 30% from 2018 to 2040. It is forecasted that the electrification of energy sectors globally will expand, with electricity production contributing to 40% of the increase in energy usage by 2040. Consequently, the International Energy Agency (2023) [12] anticipates a swift expansion and reduction in the costs of renewable energy solutions. It is expected that by 2040, renewable energy sources will constitute 40% of the worldwide electricity production, playing a significant role in reducing greenhouse gas emissions.

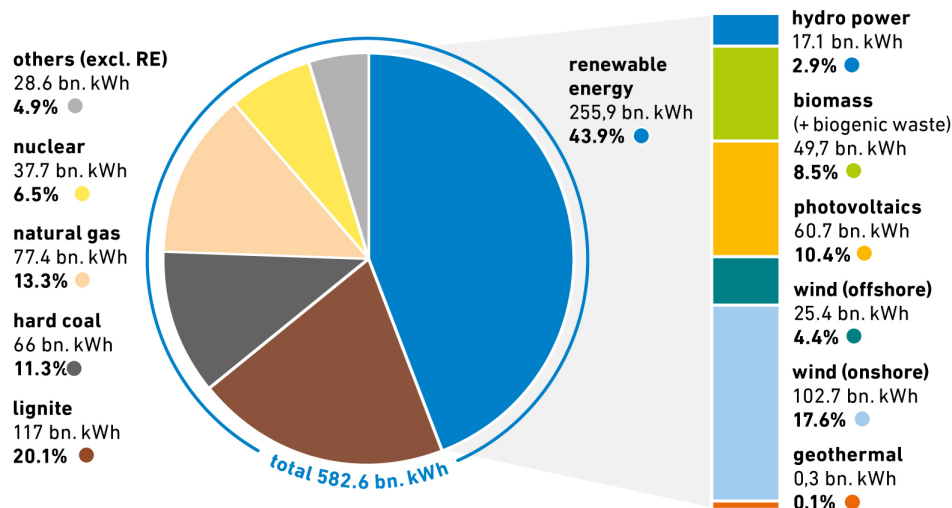


Figure 1.1: Germany's energy consumption by annual share of fuel in 2022 (left) and Electricity generation (right) reported by AG Energiebilanz [1]

The variability inherent in many renewable energy sources, such as wind and solar power, leads to unpredictable energy outputs. As these intermittent renewable energies gain a larger foothold in the energy market, there emerges a critical need for adaptable backup systems to maintain electrical grid stability. In the quest for carbon-neutral electricity, power-to-gas technologies stand out as a viable solution for grid stabilization [13].

Hydrogen is increasingly seen as a viable alternative to fossil fuels, capable of significantly cutting greenhouse gas emissions in the power generation sector. The combustion of

natural gas releases pollutants like carbon dioxide (CO_2), carbon monoxide (CO), unburnt hydrocarbons (UHC), and soot, which are avoided with hydrogen due to its carbon-free composition. Hydrogen production via electrolysis, coupled with its use in distributed energy systems with a high share of renewables, serves as both a negative power reserve and a method for energy arbitrage, supporting grid flexibility [14].

To address the challenge of smoothing out the erratic production of renewable energy and compensating for the intermittent availability of wind and solar power, stationary gas turbines are seen as a solution. Their quick start-up times, high load flexibility, and efficiency in part-load operation make them ideal for bridging gaps in renewable energy supply. Their use in integrated gasification combined cycle (IGCC) power plants represents the most efficient method for electricity generation with optimal thermal efficiency [15].

The next generation of gas turbine combustors is being designed to enhance fuel adaptability and maintain stable combustion across diverse operating conditions. The introduction of hydrogen as a fuel alters the combustion process and impacts the performance of turbine components, due to its higher reactivity and combustion speed. This leads to challenges such as increased risks of flashback and auto-ignition [16]. Consequently, conventional dry low NO_x (DLN) combustion systems, optimized for natural gas, are unsuitable for hydrogen fuel. The higher flame temperatures associated with hydrogen combustion also elevate nitric oxides (NO_x) production rates, prompting the development of mitigation strategies for gas turbines utilizing hydrogen combustion technologies [17]. Fundamentally, the production of NO_x during the combustion process in gas turbines is primarily influenced by insufficient mixing of fuel and oxidizer, prolonged combustion durations, and elevated flame temperatures. The absence of carbon in hydrogen precludes the emergence of fuel-related nitrogenous compounds that are precursors to NO_x .

Additionally, the practice of lean combustion, characterized by a surplus of oxidizer over fuel, inherently restricts the availability of oxygen, curtailing the formation of NO_x [18]. Enhancements in hydrogen combustion, such as the introduction of water injection, serve to lower combustion temperatures further. Meanwhile, the implementation of catalytic converters, through the process of selective catalytic reduction, offers another avenue for the suppressing NO_x emissions [19]. Lastly, the utilization of exhaust gas recirculation to dilute the combustible mixture stands as an effective strategy. Collectively, these factors solidify the role of hydrogen combustion as a superior and ecologically beneficial option for a wide array of applications.

1.2 Objectives and Scope

The primary aim of this thesis is to undertake a detailed benchmark analysis of DLRs hydrogen combustion simulation tools by executing 3D steady state RANS simulations that incorporate combustion chemistry models. This analysis employs a case study methodology, utilizing existing experimental data from a single-nozzle FLOX[®] based combustor [20]. The objectives are as follows:

1. To verify the simulation models applied in the ThetaCOM in-house code through comprehensive grid studies, ensuring their plausibility and accuracy.
2. To refine the accuracy and applicability of DLRs hydrogen combustion simulations, with a focus on exploring the nuances of fuel and load flexibility in combustion systems. This endeavour aims not only to validate CFD models through rigorous grid studies, but also to extend our understanding of operational flexibility across a range of conditions. These include investigations into Fuel and Load Flexibility (FF, LF) and the assessment of Non-Premixed (NP), Technically Premixed (TP), and Fully Premixed (FP) configurations.
3. A critical aspect of this work involves the meticulous comparison and validation of simulation results against experimental data. Emphasis will be placed on the precise prediction of flame characteristics, NO_x emissions, and the formation of recirculation zones. Through these comparative analyses, the thesis seeks to ascertain the combustion models' effectiveness and reliability.
4. Furthermore, this study is committed to the thorough documentation of methodologies, outcomes, and insights. To accomplish these objectives, the thesis will leverage the ThetaCOM code for CFD simulations, supplemented by ANSYS Workbench for pre-processing and grid generation, and Tecplot for post-processing.

This approach ensures a focused and feasible study, mindful of the balance between computational demands and the quest for simulation accuracy.

By navigating these complexities, the thesis endeavours to contribute meaningful advancements to the field of hydrogen combustion and offer valuable insights for the design and optimization of future combustion systems.

Limitations inherent to this thesis relate to the computational capabilities and accuracy of the numerical models employed. While Direct Numerical Simulation (DNS) offers unparalleled fidelity, it is computationally prohibitive for extensive parametric studies. Consequently, this work will utilize the Reynolds-Averaged Navier-Stokes (RANS) approach in conjunction with advanced combustion chemistry models, accepting the necessary trade-offs between computational efficiency and the resolution of physical phenomena to generate practically insightful results within these constraints.

1.3 Literature survey and previous studies

The pursuit of sustainable energy paradigms has prominently included the incorporation of hydrogen as an alternative fuel within gas turbine systems, significantly advanced by developments in FLOX[®] (**FL**ameless **OX**idation) combustion technology. This innovative combustion strategy, developed to substantially mitigate nitric oxides (NO_x) emissions while simultaneously enhancing the operational efficacy of these systems, is founded upon rigorous scientific inquiry and developmental efforts dedicated to the optimization of combustion dynamics.

Initially developed to reduce thermal NO_x formation, FLOX[®] distributes the combustion process across a larger volume, avoiding high-temperature zones characteristic of conventional flame combustion. This technique was further explored in the works of Wüning and Wüning [21].

An investigation by Petry et al. (2024) [20] into the fuel and load flexibility of an atmospheric single nozzle jet-stabilized FLOX[®] combustor using hydrogen/methane-air mixtures provides profound insights into the adaptability of MGTs to hydrogen fuels. Their study meticulously assessed the impact of varying hydrogen content in fuel blend from 0 to 100%, maintaining a constant equivalence ratio and thermal power. This approach unveiled that an increase in hydrogen content decreased the flame lift-off height across all configurations, emphasizing hydrogen significant effect on flame dynamics and emission profiles. Critically, the research noted a near fourfold rise in NO_x emissions with an increased hydrogen mix, underscoring the complexities of managing emissions in hydrogen-fuelled combustion systems. Their findings, demonstrating the crucial role of fuel-air mixedness in achieving efficient and low-emission combustion, will be used as reference for this thesis in order to validate the combustion simulations.

The application of hydrogen in gas turbines, has been identified as a promising path towards achieving lower emissions and higher efficiency. Research by Aigner et al. (2013) [22] has provided insights into the adaptation of flameless combustion for gas turbines, highlighting the potential of hydrogen as a key fuel in this context.

Single-nozzle FLOX[®] burners facilitate efficient and homogeneous mixing of hydrogen fuel with air, ensuring stable combustion and minimal emissions across a range of operational conditions. The challenges posed by hydrogen high reactivity, including the risk of flashback, are addressed through advanced burner designs and operational strategies, as detailed in the comprehensive study by Keller et al.(2009) [23].

Zanger, Monz, and Aigner (2013) [24] conducted a study to investigate the characteristics of confined jet flame, supporting the design of gas turbine combustors. Turbulent, lean, premixed methane/air and hydrogen/air flames with high jet velocities were stabilized in a rectangular combustion chamber, forming a strong lateral recirculation zone (LRZ) crucial for flame stabilization. Laser diagnostic techniques were employed to analyse flow fields, flame position, shape, and species concentrations. The study revealed distinct flame shapes for methane and hydrogen flames, with the hydrogen flame being nozzle-attached and the methane flame lifted. The LRZ induced stable, asymmetric flame shapes for methane flames by mixing fresh fuel/air with combustion products. Heat loss to the combustor walls significantly reduced temperatures in methane flames compared to adiabatic conditions. Turbulent shear layers induced by the LRZ contained hot combustion products without

methane, influencing flame characteristics. Intermediate mixing states, including partially reacted mixtures, were identified, suggesting a complex combustion process influenced by mixing and auto-ignition.

Another Experimental study [25], conducted under atmospheric conditions, analysed the influence of various operating conditions on the shape, location, and homogeneity of reaction zones using time-averaged OHCL images. The research discussed the dependencies of jet velocity and combustor front plate cooling on lean blow-off (LBO) limits, along with exhaust gas emissions. A modified nozzle air number was defined based on CO profiles of the cooled and uncooled designs to facilitate comparative analysis. Results indicated a distinct increase in the dispersion of OH*–signal with rising air-fuel numbers, leading to volumetric reaction regions at LBO-near conditions. Moreover, the cooling air was found to shift emission and flame profiles to lower nozzle air numbers. However, it was noted that only a portion of the cooling air interacts with the reaction region, while the rest bypasses the combustion chamber. The study demonstrated that the cooled combustor design allows for higher overall air numbers at low thermal powers, offering advantages for maximizing combustion air quantity.

Izadi et al.(2021) [26] conducted experiments to investigate the combustion behaviour of single-nozzle liquid-FLOX[®]-based burners on an atmospheric test rig. Three burner configurations were tested, focusing on variations in the burner discharge orifice diameter. The burners were operated stably within a range of air equivalence ratios and thermal powers, using JetA-1 as the liquid fuel at atmospheric pressure conditions. The exhaust gas analysis revealed low NO_x concentrations and decent CO concentrations, indicating good atomization quality and rapid evaporation rates of the liquid fuel within the reaction zone. OHCL images showed larger reaction zones at high flame temperatures and low jet velocities for all burner configurations.

Despite these advancements, the journey towards the widespread adoption of hydrogen-fuelled FLOX[®] technology in gas turbines involves navigating challenges such as scalability, material compatibility, and the economic aspects of implementing such advanced systems. Future research directions are aimed at enhancing the technology's efficiency, reliability, and adaptability to varying operational demands, ensuring its viability for broader industrial applications.

1.4 Structure of the Thesis

This thesis is structured to systematically address the challenges and objectives outlined in the exploration of hydrogen combustion simulations and the nuanced investigation of fuel and load flexibility. The thesis is divided into the following chapters:

Chapter 2: Fundamentals of Combustion Modeling

This chapter lays the groundwork for understanding reactive flows, beginning with the fundamental equations governing these processes. It then delves into the intricacies of turbulence, combustion modelling, and the discretization techniques employed in CFD simulations, setting the stage for the subsequent application-focused discussions.

Chapter 3: Single-nozzle FLOX[®] burner

Focusing on the Single nozzle FLOX[®] burner, Chapter 3 describes its construction, application and the critical aspects of flame stabilization. It discusses the key phenomena influencing combustion chamber design, such as adiabatic flame temperature, flashback, and auto-ignition. The chapter concludes with an analysis of the equations governing pollutant formation, with a special emphasis on NO_x emissions, aligning with the thesis objectives of enhancing simulation accuracy and environmental compliance.

Chapter 4: Numerical model description

Delving into the simulation process, Chapter 4 outlines the steps taken to establish a suitable computational domain, including the conduct of a grid independence study to ensure model plausibility. It also touches upon post-processing methods, indicative of the meticulous approach taken to validate and refine the combustion models used.

Chapter 5: Results and Discussion

Addresses the validation of the created numerical setup. This chapter extensively discusses the results obtained from RANS simulations and conducts a comprehensive comparative analysis of the NP, FP, and TP configurations. It evaluates the impact of fuel and load flexibility on key parameters including flame lift-off height, flame shape, NO_x emissions, flow field, and temperature.

Chapter 6: Summary and outlook

The final chapter concludes the thesis with a comprehensive summary of the findings and the conclusions drawn from the research. It encapsulates the contributions made to DLRs hydrogen combustion simulation capabilities and the broader field of combustion research, offering insights for future studies and design optimizations in the realm of sustainable energy technologies.

Chapter 2

Fundamentals of Combustion modelling

In the modern gas turbine combustors, swirling flames undergoes strong interaction between highly turbulent flow and intensive chemistry. A detailed understanding of turbulence accompanied by swirling flows and its correlation with combustion chemistry is of great importance. This chapter intends to introduce simulation theory and governing equations for the modelling of reacting flows. After that, the turbulence models and combustion models are described. Along with the flame stabilisation mechanism, the dominant flow/flame dynamics are further discussed.

2.1 Governing Equations for Compressible Reactive Flows

A system of coupled, partial differential equations can be set up to describe compressible reactive flows. These are known as Navier-Stokes equations. These are conservation equations for the mass, the momentum and the energy of the fluid in enthalpy form. In addition, transport equations for the respective species mass fractions Y_α need to be solved. The number of transport equations for a fluid is determined by the number of species in the fluid. From a total of N_s species in a fluid, $N_s - 1$ transport equations result. The conservation equations in conservative form are expressed as:

$$\frac{\partial \rho}{\partial t} + \nabla \cdot (\rho \mathbf{u}) = 0, \quad (2.1)$$

$$\frac{\partial(\rho \mathbf{u})}{\partial t} + \nabla \cdot [(\rho \mathbf{u}) \otimes \mathbf{u}] + \nabla p = \nabla \cdot \underline{\underline{\boldsymbol{\tau}}} + \rho \mathbf{f}, \quad (2.2)$$

$$\frac{\partial(\rho h)}{\partial t} + \nabla \cdot (\rho \mathbf{u} h) - \frac{\partial p}{\partial t} - \mathbf{u} \cdot \nabla p = \nabla \cdot (\lambda \nabla T) + \underline{\underline{\boldsymbol{\tau}}} : \nabla \mathbf{u} + \rho \mathbf{u} \cdot \mathbf{f}, \quad (2.3)$$

$$\frac{\partial(\rho \mathbf{Y}_\alpha)}{\partial t} + \nabla \cdot [(\rho \mathbf{u}) \otimes \mathbf{Y}_\alpha] = -\nabla \cdot \underline{\underline{\mathbf{j}}} + \mathbf{S}_\alpha. \quad (2.4)$$

The variable $\underline{\underline{\boldsymbol{\tau}}}$ characterises the stress tensor, which is defined by the following formula [27]:

$$\underline{\underline{\boldsymbol{\tau}}} \equiv 2\mu \left[\underline{\underline{\mathbf{S}}} - \frac{1}{3}(\nabla \cdot \mathbf{u})\underline{\underline{\mathbf{I}}} \right] \quad \text{with} \quad \underline{\underline{\mathbf{S}}} \equiv \frac{1}{2} [\nabla \mathbf{u} + (\nabla \mathbf{u})^T]. \quad (2.5)$$

where $\underline{\underline{S}}$ denotes the strain rate tensor. The variable μ describes the dynamic viscosity and is obtained using a weighted mean of the pure species viscosity values [28].

Also, λ represents the thermal conductivity, T is the temperature, and the term $\underline{\underline{\tau}} : \nabla \mathbf{u}$ describes the volumetric work per unit time. This is the Frobenius scalar product of the matrices $\underline{\underline{\tau}}$ and $\nabla \mathbf{u}$, resulting in a scalar term [29]. Applying the divergence operator $\nabla \cdot (\dots)$ to a dyadic product of two vectors (a matrix), represented by the operator \otimes , yields a column vector. Thus, for the two convective terms $\nabla \cdot [(\rho \mathbf{u}) \otimes \mathbf{u}]$ and $\nabla \cdot [(\rho \mathbf{u}) \otimes \mathbf{Y}_\alpha]$, and the stress tensor $\nabla \cdot \underline{\underline{\tau}}$, a column vector is obtained for each.

The diffusion mass flux can be described according to Fick's law against the concentration gradient by the approach

$$\underline{\underline{j}} = -\underline{\underline{D}} \cdot \nabla \mathbf{Y}_\alpha \quad (2.6)$$

where $\underline{\underline{D}}$ stands for the diffusion coefficients [30].

Since all equations are applied to a 3-dimensional computational domain, the balance Equation (2.2) has the dimension $\dim = 3$. The dimension of the transport equation for the species mass fractions (2.4) results from the number of species N_s . The vector \mathbf{Y} includes for $\alpha = 1, 2, \dots, N_s - 1$ species the occurrence of the mass fractions Y_α [31–33]. In addition, the following relationship applies to the sum of mass fractions:

$$\sum_{\alpha=1}^{N_s} Y_\alpha = 1 \quad (2.7)$$

The above equations include the flow quantities pressure p , density ρ , enthalpy h , and velocity \mathbf{u} . The consumption or production of a respective species α , through a chemical reaction, is described in Equation (2.4) by the chemical source term \mathbf{S}_α [34]. If the fluid used is a chemically-reactive ideal gas, the pressure p and density ρ are related to each other via the thermal equation of state. Based on the ideal gas law, the density can be calculated depending on the pressure, temperature, and the specific gas constant of the mixture R as

$$\rho = \frac{p_{\text{abs}}}{RT}. \quad (2.8)$$

where p_{abs} is the absolute pressure, which is composed of the ambient pressure p and the reference pressure p_{ref} . The specific gas constant can be expressed via the universal gas constant R_m , the mass fractions of the species Y_α , and their molar masses M_α . Thus, for the density, we have

$$\rho = \frac{p_{\text{ref}} + p}{RT} \quad \text{with} \quad R \equiv R_m \sum_{i=1}^{N_s} \frac{Y_\alpha}{M_\alpha}. \quad (2.9)$$

If the fluid is incompressible, the density is independent of hydrodynamic or acoustic pressure changes in the flow field and is merely a function of the mean thermodynamic pressure [27, 34–36]. From this, it follows that the dissipation term $\underline{\underline{\tau}} : \nabla \mathbf{u}$ and the pressure fluctuation term $Dp/Dt = \partial p/\partial t + \mathbf{u} \cdot \nabla p$ in Equation (2.3) can be neglected [31]. Assuming an ideal gas, the enthalpy h balanced in Equation (2.3) consists of thermal enthalpy and formation enthalpy, given by

$$h = \int_{T_0}^T c_p dT + \sum_{\alpha=1}^{N_s} \Delta h_{f,\alpha}^0 Y_\alpha. \quad (2.10)$$

and is thus based on the contributions of individual gas components [34,37]. The vector \mathbf{f} on the right side of the momentum and energy equations accounts for body forces such as gravitational force. Since only minor height differences are considered in gas turbines and the influence of the gravitational force is negligible compared to pressure gradients or convection, body forces can be neglected [30].

2.2 Turbulence modelling

Fluid flow can be roughly divided into laminar and turbulent flows based on the Reynolds number. The Reynolds number Re describes the ratio of inertial to viscous forces, or the ratio of specific momentum convection to momentum diffusion. It is defined as:

$$Re = \frac{u \cdot L}{\nu} \quad (2.11)$$

where u is the characteristic velocity, L is the characteristic length, and ν is the kinematic viscosity.

The transition point from laminar to turbulent flow is determined by the critical Reynolds number, which is about $Re_{\text{crit}} \approx 2300$ for flow in straight pipes [38]. Figure 2.1a showcases a laminar current, while Figure 2.1b shows a turbulent flow [39].

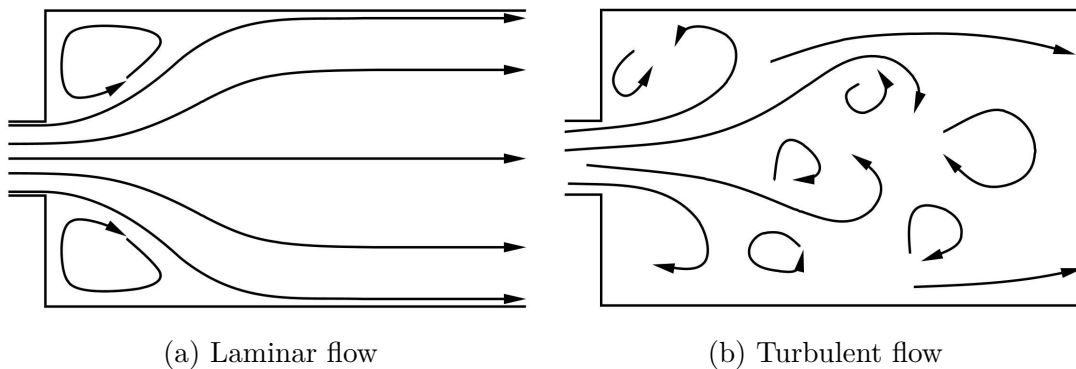


Figure 2.1: Laminar and turbulent flows in a pipe with cross-sectional expansion [39]

A turbulent flow is characterized by random, chaotically distributed velocity fluctuations, which follow the main flow of the pipe. The cause of the velocity fluctuations is the formation of vortices of different length and time scales. The occurrence of high velocity gradients ensures the formation of large, turbulent eddies, which interact with and extract kinetic energy from the main flow, breaking down into smaller and smaller vortices. Starting from the large vortices, the kinetic energy is transported across the entire vortex spectrum in so-called energy cascades. Due to the rapid drop in energy in a cascade process, the smallest vortices have the lowest kinetic energy until it is dissipated by the movement and converted into internal thermal energy (to overcome the viscous stress of the fluid). This dissipation leads to an increased energy loss, which is associated with turbulent flow [40].

Direct Numerical Simulation (DNS) is the most accurate method to solve the transport equations (2.1) - (2.3) without statistical averaging and thereby calculate turbulent flow. However, it makes the highest demands on the numerical method and computational

power, as the smallest turbulent scales must be resolved both spatially and temporally [41]. However, the CPU requirements necessary for this exceed the computational capacity available in recent years. For this reason, averaging methods are applied to the governing NS equations in order to filter out and model parts of the turbulent spectrum.

The most widely used is the Reynolds Averaged Navier-Stokes (RANS) method, whereby the conservation equations from Section 2.1 are subjected to statistical averaging. This results in the vortex structures from turbulence no longer being resolved in time and space, leading to a significant reduction in computation time and memory requirements. It allows for the numerical simulation of technically relevant flow cases with high Reynolds numbers. The turbulence model estimates the velocity and length scales of the large, energy-carrying turbulence elements, which are represented by dashed lines in Figure 2.2 [39].

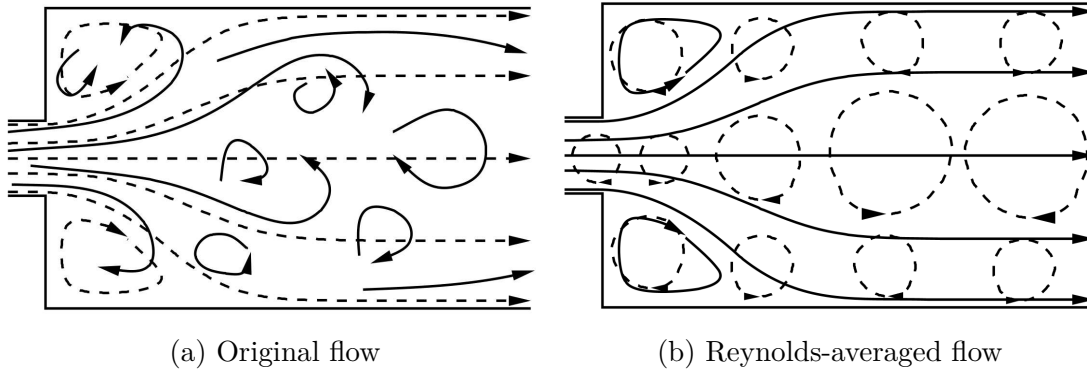


Figure 2.2: Comparison of the original and Reynolds-averaged flow in a pipe with cross-sectional expansion [39]

The basis of the RANS method is the Reynolds decomposition [42], where a flow quantity is divided into a mean value and a fluctuation [43]. This leads to the derived RANS equations, in which the fluctuation is no longer explicitly described:

$$\frac{\partial \bar{\rho}}{\partial t} + \nabla \cdot (\bar{\rho} \tilde{\mathbf{u}}) = 0, \quad (2.12)$$

$$\frac{\partial (\bar{\rho} \tilde{\mathbf{u}})}{\partial t} + \nabla \cdot [\bar{\rho} (\tilde{\mathbf{u}} \otimes \tilde{\mathbf{u}})] + \nabla \bar{p} = \nabla \cdot [\underline{\underline{\tau}} - \bar{\rho} (\mathbf{u}'' \otimes \mathbf{u}'')], \quad (2.13)$$

$$\frac{\partial (\bar{\rho} \tilde{h})}{\partial t} + \nabla \cdot (\bar{\rho} \tilde{\mathbf{u}} \tilde{h}) - \frac{Dp}{Dt} = \nabla \cdot \left[\frac{\lambda}{c_p} \nabla \tilde{h} + \bar{\rho} \mathbf{u}'' \tilde{h}'' \right] + \underline{\underline{\tau}} : \nabla \mathbf{u}, \quad (2.14)$$

$$\frac{\partial (\bar{\rho} \tilde{Y}_\alpha)}{\partial t} + \nabla \cdot [\bar{\rho} (\tilde{\mathbf{u}} \otimes \tilde{Y}_\alpha)] = \nabla \cdot [\underline{\underline{D}} \cdot \nabla \tilde{Y}_\alpha + \bar{\rho} (\mathbf{u}'' \otimes Y_\alpha'')] + \bar{S}_\alpha. \quad (2.15)$$

In Equation (2.14), the heat flux is transformed according to Fourier's law to:

$$\lambda \nabla T = \frac{\lambda}{c_p} h. \quad (2.16)$$

The averaging of the flow quantities in equations (2.12) to (2.15) are divided into Reynolds-averaged quantities (denoted by $\overline{(\dots)}$) and Favre-averaged quantities (denoted by $\widetilde{(\dots)}$). The respective fluctuation quantities are represented by $(\dots)''$ [44].

Due to the averaging process, unclosed terms occur, which must be modelled by suitable turbulence models. In addition, averaging is always associated with a loss of information.

The unclosed terms are the chemical source term $\overline{S_\alpha}$, the component fluxes $\mathbf{u}'' \otimes \widetilde{Y_\alpha''}$, the enthalpy fluxes $\overline{\rho \mathbf{u}'' \widetilde{h''}}$ and the Reynolds stresses $\mathbf{u}'' \otimes \widetilde{\mathbf{u}''}$. Using the gradient diffusion approach, both the Reynolds energy flux and the component flux can be transformed as follows [45, 46]:

$$\overline{\rho \mathbf{u}'' \widetilde{h''}} \approx -\frac{\mu_t}{Pr_t} \nabla \widetilde{h} \quad \text{and} \quad \overline{\rho (\mathbf{u}'' \otimes \widetilde{Y_\alpha''})} \approx -\frac{\mu_t}{Sc_t} \nabla \widetilde{Y_\alpha}. \quad (2.17)$$

Here, μ_t describes the turbulent viscosity, $Pr_t = (\mu_t c_p) / \lambda_t$ the turbulent Prandtl number, and $Sc_t = \mu_t / (\overline{\rho} D_t)$ the turbulent Schmidt number. λ_t represents the turbulent thermal conductivity, and D_t is the turbulence-induced diffusion coefficient [44]. The Reynolds stresses are closed in RANS models using the linear eddy viscosity hypothesis of Boussinesq [47]. The basis of the approach is the assumption that a turbulent flow is present and that the Reynolds stresses are proportional to the velocity gradients of the mean main flow. This results in the following expression for the Reynolds stresses:

$$-\overline{\rho (\mathbf{u}'' \otimes \widetilde{\mathbf{u}''})} \approx \mu_t \left[\nabla \tilde{\mathbf{u}} + (\nabla \tilde{\mathbf{u}})^T - \frac{2}{3} (\nabla \cdot \tilde{\mathbf{u}}) \mathbf{I} \right] - \frac{2}{3} \overline{\rho} k \quad (2.18)$$

where $k = \frac{1}{2} \cdot (\mathbf{u}'' \cdot \widetilde{\mathbf{u}''})$ represents the turbulent kinetic energy and \mathbf{I} is the identity matrix [30]. The modelling of Reynolds stresses in RANS models is thus reduced to the calculation of the turbulent viscosity. Unlike molecular viscosity μ , turbulent viscosity is not a material property but a function of the turbulence. A variety of models for determining turbulent viscosity are proposed in the literature [37]. The approaches used in this work for turbulence description are explained in the following sections 2.2.1 and 2.2.2.

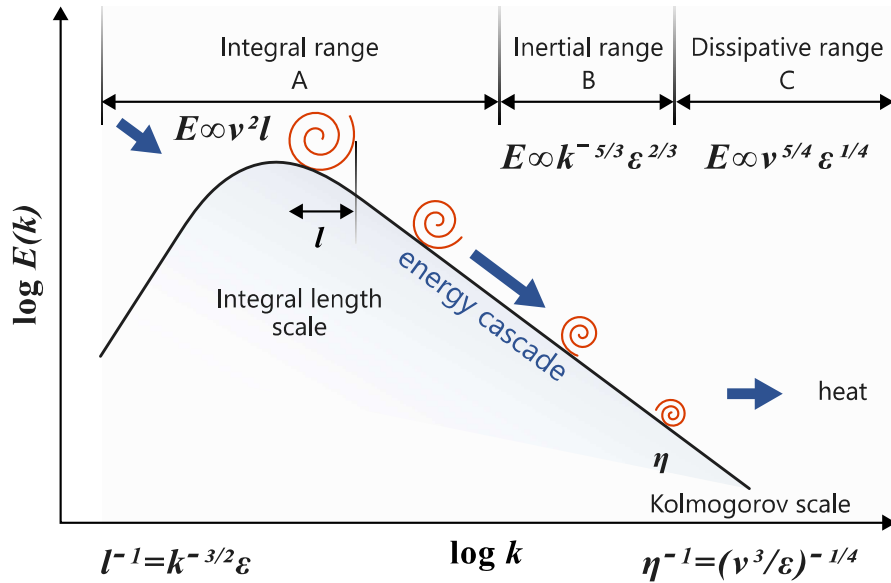


Figure 2.3: Schematic Representation of Turbulence Energy Spectrum adapted from [48, 49].

To calculate unsteady flows, Unsteady Reynolds Averaged Navier-Stokes (URANS) simulations are often used. The turbulence models derived for steady-state RANS conditions are applied to the averaged, unsteady conservation quantities. However, this approach can only resolve flow fluctuations within the range of integral length and time scales [50].

In the approach known as Large Eddy Simulation (LES), only the large and energy-carrying vortices are directly resolved. The influence of smaller, anisotropic scales (fine vortex

structures), whose spatial extent is smaller than the spatial resolution of the computational grid, is modelled. This requires a decomposition of the turbulent flow field into fine and coarse structures. The LES thus lists all turbulence elements that are larger than a selected spatial filter width. Due to the finer temporal and spatial discretization as well as the fact that only the effect of the filtered out, smaller turbulence elements on the resolved flow are approximated, the computational effort of LES increases significantly compared to RANS simulations [39, 51]. Figure 2.3 provides an overview of the resolution degree of turbulent structures.

In the ThetaCOM [2], the following RANS turbulence models are available:

- One-equation eddy-viscosity models:
 - Spalart-Allmaras (SA-Standard)
- Two-equations eddy-viscosity models:
 - Standard k - ε
 - Wilcox k - ω (Wilcox-1988 model)
 - Menter SST (SST-1994 and SST-2003 models)

2.2.1 The k - ε Turbulence Model

All k - ε models are two-equation models, which are frequently used in industrial flow simulations. These models solve two transport equations and model the Reynolds stresses through the linear eddy viscosity approach of Boussinesq, as mentioned in Section 2.2 [52]. The robustness, economy and reasonable accuracy explain the frequent use of these models in industrial flow and heat transport simulations. The disadvantages of some k - ε models are their insensitivity to negative pressure gradients and boundary layer dissipation. They usually calculate a delayed and reduced dissipation compared to visual experiments [40].

The Standard k - ε Model

For turbulent flows with high Reynolds numbers, the k - ε model established by Launder and Spalding [53] remains one of the most used turbulence models in CFD simulations, often referred to as the Standard k - ε Model. The theoretical descriptions of the following k - ε models are based on the works of Schwarze [39] and Kunz [52], with detailed descriptions available in the references by Launder et al. [53, 54]. The turbulent stresses are attributed to gradients in the main flow. The production P_k and diffusion D_k of turbulent kinetic energy, due to velocity gradients in the flow, are approximated in the transport equations for turbulent kinetic energy k as follows:

$$P_k = \mu_t \nabla \mathbf{u} \cdot [\nabla \mathbf{u} + (\nabla \mathbf{u})^T] \quad (2.19)$$

$$D_k = \nabla \cdot \left(\mu \nabla k + \frac{\mu_t}{\sigma_k} \nabla k \right) = \nabla \cdot \left[\left(\mu + \frac{\mu_t}{\sigma_k} \right) \nabla k \right] \quad (2.20)$$

Using the turbulent kinetic energy k and dissipation rate ϵ , the velocity scale U_t and timescale L_t (characteristic scales of turbulence) can be estimated as

$$U_t = \sqrt{k} \quad \text{and} \quad L_t = \frac{k^{1.5}}{\epsilon} \quad (2.21)$$

The transport equations for the turbulent kinetic energy k and the turbulent dissipation rate ϵ are as follows:

$$\frac{\partial(\bar{\rho}k)}{\partial t} + \nabla(\bar{\rho}\mathbf{u}k) - \nabla \cdot \left[\left(\mu + \frac{\mu_t}{\sigma_k} \right) \nabla k \right] = \tilde{P}_k - \bar{\rho}\epsilon \quad (2.22)$$

$$\frac{\partial(\bar{\rho}\epsilon)}{\partial t} + \nabla(\bar{\rho}\mathbf{u}\epsilon) - \nabla \cdot \left[\left(\mu + \frac{\mu_t}{\sigma_\epsilon} \right) \nabla \epsilon \right] = C_1 \tilde{P}_k \frac{\epsilon}{k} - C_2 \bar{\rho} \frac{\epsilon^2}{k} \quad (2.23)$$

The modelling in Equation (2.23) is based on the assumption that the production and decay of ϵ are proportional to their respective terms in Equation 2.22. The proportional factors in Equation 2.23 are the terms $C_1 \tilde{P}_k \epsilon/k$ and $C_2 \bar{\rho} \epsilon^2/k$. In this case, the turbulent viscosity is calculated as $\mu_t = C_\mu \bar{\rho} k^2/\epsilon$, where it is simplistically treated as a scalar. The transport equations contain model constants, which for the Standard k - ϵ model are usually proposed as shown in Table 2.1 [55, 56]. These values have been adapted for a wide range of flow conditions and are based on the analysis of canonical flows using the Standard k - ϵ Model. Canonical flows refer to simplified flow configurations such as boundary layer or free jet flows. In combination, these can represent key properties of complex flows [39]. The

Table 2.1: Model constants of the Standard k - ϵ Model.

C_μ	σ_k	σ_ϵ	C_1	C_2
0.09	1.0	1.3	1.44	1.92

model is well-suited for the calculation of flows, such as fully turbulent pipe flow, and is often used to analyse flow processes where the global flow structures are to be determined. In the case of complex flows or near-wall regions, where turbulence can typically not be assumed fully developed, the model sometimes provides poor quantitative and qualitative results [39]. To compensate for this disadvantage, special models, such as Low-Reynolds or wall functions, are used.

2.2.2 The k - ω Turbulence Model

In addition to the various k - ϵ models, turbulence models are increasingly being used, which determine the characteristic turbulent frequency ω of the energy-carrying vortices. The turbulent frequency is defined as

$$\omega = \frac{\epsilon}{k} \left(= \frac{U_t}{L_t} \right) \quad (2.24)$$

The Standard k - ω Model by Wilcox [57] is a two-equation turbulence model that also relies on the eddy viscosity principle. The foundation of these eddy viscosity models is the assumption that turbulence results in an increase in viscosity. The laminar and turbulent viscosity are added together, thereby affecting the flow.

The k - ω model is defined by a transport equation for the turbulent kinetic energy k and for the turbulent frequency ω [30]:

$$\frac{\partial(\bar{\rho}k)}{\partial t} + \nabla(\bar{\rho}\mathbf{u}k) - \nabla \cdot \left[\left(\mu + \sigma^* \frac{k}{\omega} \right) \nabla k \right] = \tilde{P}_k - \beta^* \bar{\rho} \omega, \quad (2.25)$$

$$\frac{\partial(\bar{\rho}\omega)}{\partial t} + \nabla(\bar{\rho}\mathbf{u}\omega) - \nabla \cdot \left[\left(\mu + \sigma \frac{k}{\omega} \right) \nabla \omega \right] = \tilde{P}_k \frac{\alpha}{\nu_t} - \beta \bar{\rho} \omega^2. \quad (2.26)$$

The turbulent kinematic viscosity is calculated as $\nu_t = k/\omega$. For the excitation term \tilde{P}_k on the right side of equations (2.25) and (2.26), we have:

$$\tilde{P}_k = \min \left(\mu_t \nabla \mathbf{u} \cdot [\nabla \mathbf{u} + (\nabla \mathbf{u})^T], 10 \cdot \beta^* \bar{\rho} k \omega \right) \quad (2.27)$$

\tilde{P}_k is a limiter to restrict the production of turbulence in stagnation areas [58]. The remaining model constants are listed in Table 2.2. In the area close to the wall, this

Table 2.2: Model constants of the Standard k - ω Model [57].

α	β	β^*	σ	σ^*
5/9	3/40	0.09	0.5	0.5

model provides a much better description of the mean turbulence and thus the entire mean flow field than the standard k - ε Model. However, in free external flows and shear layers, turbulence and flow modelling performs significantly worse [39, 59].

The k - ω SST Turbulence Model

The Shear-Stress-Transport (SST) Model, developed by Menter [60], is based on the k - ω Model by Wilcox and combines the advantages of both the k - ε and k - ω models [61]. The k - ω SST Model employs a hybrid approach with two different model equations for ω . Near the wall, the k - ω Model is used to calculate the mean turbulence and flow quantities. In the free field, blending functions transition to the k - ε Model. The theoretical description of the k - ω SST Model is based on the works of Reichling [31] and Grimm [44]. The transport equations for k and ω in this model are as follows:

$$\frac{\partial(\bar{\rho}k)}{\partial t} + \nabla(\bar{\rho}\mathbf{u}k) - \nabla \cdot [(\mu + \sigma_k \mu_t) \nabla k] = \tilde{P}_k - \beta^* \bar{\rho} \omega, \quad (2.28)$$

$$\frac{\partial(\bar{\rho}\omega)}{\partial t} + \nabla(\bar{\rho}\mathbf{u}\omega) - \nabla \cdot [(\mu + \sigma_\omega \mu_t) \nabla \omega] = \tilde{P}_k \frac{\alpha}{\nu_t} - \beta \bar{\rho} \omega^2 + 2(1 - F_1) \frac{\bar{\rho} \sigma_\omega^2}{\omega} (\nabla k \nabla \omega). \quad (2.29)$$

F_1 is a blending function which is expressed using the following formula:

$$F_1 = \tanh \left\{ \left\{ \min \left[\max \left(\frac{k}{\beta^* \omega y}, \frac{500\nu}{y^2 \omega} \right), \frac{4\bar{\rho} \sigma_\omega^2 k}{CD_{k\omega} y^2} \right] \right\}^4 \right\}. \quad (2.30)$$

Here y corresponds to the wall distance, ν to the kinematic viscosity and $CD_{k\omega}$ to the cross-diffusion term, which is described by the following expression:

$$CD_{k\omega} = \max \left(2\bar{\rho} \sigma_\omega^2 \frac{1}{\omega} (\nabla k \nabla \omega), 10^{-10} \right) \quad (2.31)$$

In the far-field, the blending function F_1 from Equation (2.30) approaches zero and takes the value of one within the boundary layer. The turbulent kinematic viscosity in this model is calculated as:

$$\nu_t = \frac{a_1 k}{\max(a_1 \omega, F_2 \sqrt{2S_{ij}} \cdot S_{ij})} \quad (2.32)$$

The excitation term \tilde{P}_k was already introduced and defined in Section 2.2.2, and the shear rate S_{ij} earlier in Section 2.2.1. F_2 in Equation (2.32) is another blending function, defined as:

$$F_2 = \tanh \left\{ \left[\max \left(\frac{2\sqrt{k}}{\beta^*\omega y}, \frac{500\nu}{y^2\omega} \right) \right]^2 \right\}. \quad (2.33)$$

If we assume ν as a vector comprising the entries α , β , and σ , the model constants without subscript can be expressed through the blending functions as:

$$\nu = F_1\nu_1 - (1 - F_1)\nu_2 \quad \text{with} \quad \nu = [\alpha \ \beta \ \sigma]^T \quad (2.34)$$

The model constants for the k - ω SST Model are presented in Table 2.3.

Table 2.3: Model Constants for k - ω SST Model [31]

α_1	α_1	α_2	β_1	β_2	β^*	σ_{k1}	σ_{k2}	$\sigma_{\omega 1}$	$\sigma_{\omega 2}$
0.31	0.5	0.44	0.075	0.828	0.09	0.85	1	0.5	0.856

Within the flow field, ω generally takes small values, which, however, increase drastically in the very near-wall area. This implies that the k - ω SST Model requires a correspondingly fine wall resolution in the boundary layer, becoming especially relevant in specific applications where flow separation occurs. By combining the k - ω and k - ε models, the k - ω SST Model leverages the advantages of both models and can even compensate for the respective disadvantages of each model [39].

Consequently, the use of the k - ω -SST turbulence model requires a proper resolution of the boundary layer. In order to achieve an adequate boundary layer resolution, conditions concerning the meshing of the computational domain need to be applied to the near-wall region. A resolution of the boundary layer region of $y^+ \approx 1$ is therefore recommended when the k - ω -SST turbulence model is used. According to [62], the dimensionless wall distance y^+ is defined by the following relation:

$$y^+ \equiv \frac{u_\tau}{\nu} \cdot y \quad \text{with} \quad u_\tau = \sqrt{\frac{\tau_w}{\rho}} \quad \text{and} \quad \tau_w = \rho\nu \frac{\partial u_{\parallel}}{\partial x_n} \quad (2.35)$$

In the above equation, u_τ is the shear velocity, whereas τ_w and ν denote the wall shear stress and the kinematic viscosity, respectively. u_k and x_n stand for the velocity component parallel and the coordinate normal to the wall, respectively. y describes the wall distance. As a consequence, the first point should be at a distance of $y^+ \approx 1$. The boundary layer of the flow in the near-wall area should be resolved using at least eight to ten grid points.

A dimensionless wall distance higher than unity can lead to a boundary layer which will not be correctly calculated within the numerical simulation carried out later on. In this case, the overall solution might be erroneous, and convergence problems may occur [61]. However, for the numerical computation of complex industrial flows the requested grid resolution near the walls is in general too high, since this would lead to a large amount of computational time. The strict application of wall functions enables the use of coarser grid regions, but has the inconvenience of limiting the model accuracy. As a remedy to this issue, the automatic near-wall treatment [50] is applied. The key idea of the automatic

near-wall treatment is that it shifts gradually between a viscous sublayer formulation and the use of wall functions based on the grid density within the near-wall region [31]. This automatic near-wall treatment is well-suited for the ω -equation, as the ω -equation provides analytical solutions for both the sublayer and the logarithmic zone. The automatic near-wall treatment is incorporated in the ThetaCOM CFD code and is used for the test case in this section.

2.3 Combustion modelling

Combustion is rapid, self-sustaining oxidation of fuels (typically hydrocarbons) with the release of heat, light, and volatile substances, and is referred to as an exothermic reaction. The area in which most of the chemical conversion takes place is called the flame. The narrow reaction zone between reaction educts and products is called the flame front. In principle, a distinction is also made between the mixing state of fuel and oxidizer when entering the combustion chamber. A distinction is made between a homogeneous premixed or separated state when entering the combustion chamber or whether the mixing only takes place immediately before the chemical reaction [63]. If the combustion completely converts both fuel and oxidiser into reaction products, the mixture is considered stoichiometric. To accurately describe the combustion process, the air-fuel ratio λ and the equivalence ratio ϕ are introduced. For an air/fuel mixture, the equivalence ratio is defined as [63]

$$\phi = \frac{1}{\lambda} = \frac{(\dot{m}_{\text{Air}}/\dot{m}_{\text{Fuel}})_{\text{stoich}}}{(\dot{m}_{\text{Air}}/\dot{m}_{\text{Fuel}})} \quad (2.36)$$

where \dot{m}_{Air} and \dot{m}_{Fuel} are the air and fuel mass flow rates, respectively. The air-fuel ratio λ represents the relationship of a fuel-air mixture to its stoichiometric mixture. This classification determines whether combustion is rich, stoichiometric, or lean. For $\lambda < 1$, a rich mixture is present, indicating an excess of fuel that is not completely burned. A lean mixture, characterised by $\lambda > 1$, indicates an excess of oxidiser. A stoichiometric mixture is achieved for $\lambda = 1$.

2.3.1 Modes of Combustion

Non-premixed Flames

Traditionally, non-premixed combustion has been the prevailing mode, wherein fuel and oxidizer are introduced independently into the combustion process [64]. Non-premixed combustion is distinguished by its high stability and elevated local firing temperatures [65]. The governing factor for non-premixed flames is the rate at which fuel and oxidizer can reach the flame front. In laminar flames, diffusion dominates the supply rate, leading to the characterization of non-premixed flames as diffusion flames. Once fuel and air are thoroughly mixed, combustion typically occurs near stoichiometric conditions, where all fuel and oxidizer are consumed. In turbulent non-premixed flames, diffusion and turbulent mixing govern the supply rate to the flame front, with the mixing rate dependent on turbulence intensity. A drawback of non-premixed combustion is the significant production of nitrogen oxides (NO_x), linked to high firing temperatures [66]. Given the recognized harm of NO_x emissions to human health, global efforts to minimize them are imperative [19, 67]. One strategy to mitigate NO_x emissions involves reducing local firing temperatures, achievable through non-premixed flame cooling using inert species or water. However, this approach necessitates additional resources of water and/or inert species alongside the fuel and oxidizer.

Premixed and Partially Premixed Flames

Premixed flames involve the blending of fuel and oxidizer before entering the flame zone. A key distinction lies in the fact that premixed flames exhibit flame propagation. In non-premixed flames, there exists a zone with combustion products and another with unburned fuel or oxidizer [68]. In premixed flames, the combustion products coexist with a flammable mixture of fuel and oxidizer, allowing the flame to propagate into fresh mixtures. While diffusion rate remains crucial in premixed flames, the reaction rate equally influences flame stabilization. Ideally, achieving a perfectly premixed flame requires homogeneous mixing of fuel and oxidizer, a condition rarely met in real applications [65]. Fuel is often continuously injected into the oxidizer stream, introducing gradients in the fuel and oxidizer mixture upstream of the flame front, resulting in partially premixed flames. The degree of mixedness, or rather unmixedness, significantly impacts flame behaviour and must be considered when dealing with partially premixed flames.

Lean Premixed

An alternative approach to reduce firing temperatures involves lean premixed combustion, where fuel and air are premixed with an excess of oxidizer. In this scenario, all fuel reacts, but not all oxidizer is consumed [65]. The surplus oxidizer serves to cool the flame, reducing the firing temperature to varying degrees depending on the amount of excess oxidizer.

2.3.2 Turbulent Premixed Combustion

Turbulence is vital in combustion, enhancing reactivity, mixing, and efficiency. When a flame interacts with turbulent flow, the laminar flame structure is replaced by turbulent regimes. Numerous chemical reactions taking place within the flow exhibit a diverse range of temporal scales, ranging from nanoseconds to seconds, alongside the temporal and

spatial scales of turbulence [69].

Borghis and Peters have categorized turbulent flame regimes using dimensionless numbers obtained from scaling analysis [70, 71]. Identifying an appropriate regime is crucial for modelling the reaction process, leading to the construction of diagrams under certain assumptions. These assumptions include isotropic turbulence, adiabatic conditions, and unit Lewis and Schmidt numbers ($Sc = \frac{\nu}{D_{i,\text{mix}}}$). The concept relies on the size of eddies and the flame thickness (δ_f). Eddies larger than δ_f cannot penetrate the flame but stretch and wrinkle it, known as the flamelet concept. This model represents the turbulent flame as a collection of stretched laminar flamelets with a local flame speed S_L^0 . Conversely, eddies smaller than the flame thickness penetrate the reaction zone, distorting both the flame and the timescale, identified as the non-flamelet region. The boundary between these regions is determined by the criterion proposed by Klimov and Williams [72].

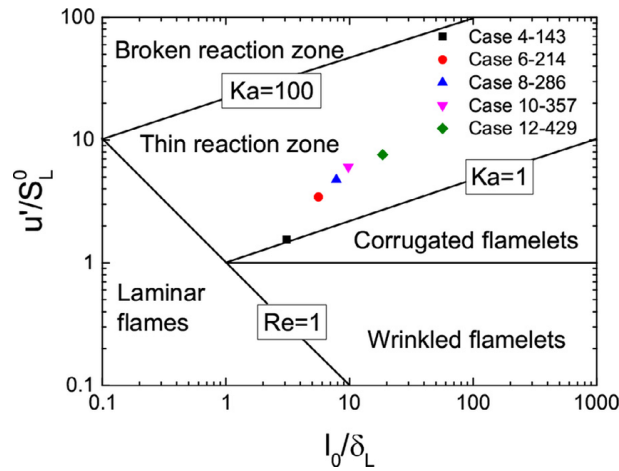


Figure 2.4: Borghis and Peters combustion regime diagram, adapted from [65, 70, 73].

The interaction between the flame front and turbulence is represented by Damköhler number (Da) and Karlovitz number (Ka). Da number is defined as the ratio of turbulent integral timescale to chemical timescale [73]. Peters proposed that even if eddies are smaller than the flame thickness (δ_f), they will still enter the preheat zone and expand it [71]. This hypothesis led to the identification of a different regime, termed the thin reaction zone, where a broad preheat zone exists. The boundary between a well-stirred reactor and the thin reaction zone is defined by Peters' criterion $Ka_{\delta_r} = 1$. Combustion regimes of turbulent premixed combustion are summarised as follows [73]:

- **For $Ka < 1$ (Flamelets):**
 - Flame thickness is smaller than turbulent eddies, and they penetrate into the flame. This flamelet region is further divided into Wrinkled flamelets ($u' \approx S_L^0$) and Corrugated flamelets ($u' > S_L^0$)
- **For $Ka > 1$ (Thin reaction zones):**
 - Small-scale turbulent eddies penetrate into the preheat zone and enlarge the flame thickness.
- **For $Ka > 100$ (Broken reaction zones):**
 - Reaction is the rate-limiting step, since turbulence is much faster than reaction. Turbulence mixes like a well-stirred reactor.

2.3.3 Pollutant Formation

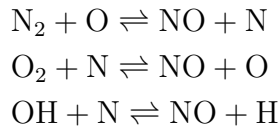
The regulations aiming at limiting pollutant emissions from gas turbines have become increasingly stringent over the past few decades [74]. The main pollutants emitted by combustors are in the form of nitrogen oxides (NO_x), unburned hydrocarbons (UHC), and carbon monoxide (CO).

Nitrogen Oxides

NO_x is a general term for nitrogen oxides, namely nitrogen monoxide (NO) and nitrogen dioxide (NO_2), that are most relevant for air pollution in terms of photochemical smog and acid rain [75]. The formation of NO_x is mainly observed via three mechanisms:

- Thermal NO_x is a major source produced in applied gas turbine combustors using nitrogen-free fuels. It is usually generated in the post-flame region at high temperatures, typically above 1800 K. The set of reactions for thermal NO is referred to as the extended Zeldovich mechanism (see Table 2.4).

Table 2.4: Zeldovich Mechanism [8]



- Prompt NO_x is generated in the reaction zone as an attribute of hydrocarbon flames, where hydrocarbon radicals react with nitrogen [68]. This mechanism shows less dependence on temperature and becomes more important when other NO_x formation mechanisms are suppressed.
- Fuel NO_x is produced from the nitrogen-containing functional group. Most of the chemically bound nitrogen in amino groups is converted to HCN and NH_3 to sequentially react with other free radicals in the combustion process to form NO. In ammonia flames, the fuel NO_x emission remains a major challenge towards its application in practical gas turbines.

Carbon Monoxide

Carbon monoxide (CO) is a toxic gas that negatively affects cardiovascular function. A high concentration of CO suppresses the capacity of the blood to absorb oxygen and causes asphyxiation [76]. It is usually generated in a combustion process operated at fuel-rich conditions due to a lack of sufficient oxygen to complete the reaction to CO_2 . The formation of CO is also influenced by temperature and pressure. Dissociation of CO_2 into CO occurs when the flame temperature peaks beyond 1800 K under stoichiometric conditions [76].

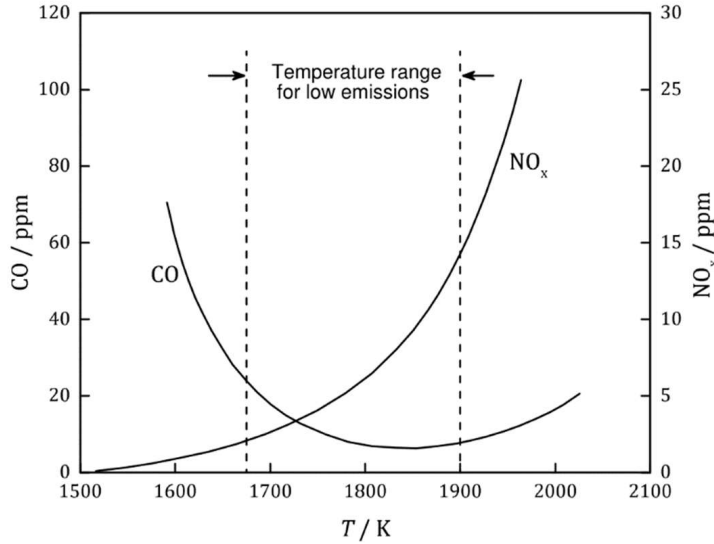


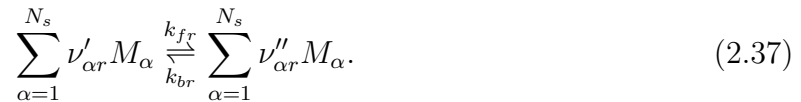
Figure 2.5: Dependence of emissions on Adiabatic Flame Temperature. Adapted from [76]

Unburned Hydrocarbons (UHC)

UHC are hydrocarbons emitted from the combustion process, particularly when using liquid fuels. Their presence typically indicates insufficient atomization and evaporation of the liquid fuel, leading to fuel inefficiencies and waste [76]. In general, the formation and emission of UHC are affected by the same factors as CO, while the reaction kinetics of UHC is more complicated.

2.3.4 Chemical reaction kinetics

Combustion processes are essentially chemical redox reactions, which can be represented by reaction equations. The main objective of this work is to investigate the influence of mixedness on the fuel and load flexibility of methane-hydrogen-air flames stabilized inside a single-nozzle FLOX[®] combustor. To describe such mechanisms, the interaction of several hundred to thousands of elementary reactions must be considered [69]. These reactions collectively form a detailed reaction mechanism and define the combustion process. Consequently, a large number of additional transport equations need to be solved, resulting in a significantly higher demand for resources [77]. Generally, a reaction mechanism consisting of $r \in \{1, 2, \dots, N_r\}$ elementary reactions and $\alpha \in \{1, 2, \dots, N_s\}$ species can be described by the relation [30]



In Equation (2.37), arrows indicate the direction in which a corresponding reaction occurs. M_{α} represents the molecular weight of a species α involved in the reaction. The factors $\nu'_{\alpha r}$ and $\nu''_{\alpha r}$ represent the stoichiometric coefficients of the respective reactants and products. k_{fr} and k_{br} are the rate constants for the forward and reverse reactions, interpreted as the probability of molecular collisions. These rate constants describe the speed at which reaction r occurs [65]. At least one of these values can typically be calculated using the

extended Arrhenius approach:

$$k_{i,r} = A_r T^{\beta_r} \exp\left(-\frac{E_{a,r}}{R_m T}\right), \quad \text{for } i \in [f, b], \quad (2.38)$$

where the constants A_r and β_r describe the collision frequency of the molecules. $E_{a,r}$ stands for the activation energy of the reaction and R_m is the universal gas constant [34, 78].

2.3.5 Modelling of the Chemical Source Term

Reactive flows are controlled by the fundamental equations (2.1) to (2.4). To simulate reactive, turbulent flows, it is necessary to use the averaged Navier-Stokes (NS) equations (2.12) to (2.15). Various methods for modelling these equations have been introduced in earlier chapters. However, we still need an approach to model the averaged chemical source term \bar{S}_α from Equation (2.15) in order to fully address the closure problem of the averaged NS equations. Therefore, the key to combustion modelling lies in describing the chemical source term and approximating the interactions between turbulent fluctuations and chemical kinetics.

As mentioned earlier in Section 2.3.4, chemical transformations in combustion processes are described using chemical reaction mechanisms. For instance, a detailed description of hydrogen combustion involves dozens of reaction steps [30, 37], which significantly increases the number of component transport equations and computational power required. In addition, complex reaction schemes have large differences in chemical time scales, leading to a stiff numerical system that requires sophisticated solution method [79]. To maintain reasonable computation times, simplified treatments of chemical reactions are used to calculate the averaged source term. Combustion models are generally categorised into component transport models and models based on tabulated chemistry [30, 44]. The following chapters will focus exclusively on the component transport models utilised in this study.

The Eddy Dissipation Model

The **Eddy Dissipation Model** (EDM) is a robust, mixing-controlled model suitable for both premixed and non-premixed combustion modelling. Originally introduced by Magnussen [80, 81] as an extension of the Eddy Break-Up model by Spalding [82], EDM is a vortex decay model, where the determining timescale corresponds to the turbulent mixing time. It assumes very fast chemical reactions compared to the turbulent mixing of fuel and oxidiser, as well as chemical equilibrium. Thus, the model presumes infinitely fast chemistry, reducing the problem of solving the chemical source term to a problem of turbulent mixing [63]. The mixing timescale in CFD-RANS is also described as the integral timescale of turbulence:

$$\tau_t = \frac{k}{\epsilon} = \frac{1}{\beta^* \omega} \quad (2.39)$$

where β^* is a model constant of the k - ω SST Model introduced in Section 2.2.2. The reaction rate RR of a species α in the EDM approach is calculated as:

$$\overline{RR}_r^{\text{EDM}} = A \frac{\rho}{\tau_t} \left[\min \left(\min_{e, \nu'_{e,r} \neq 0} \frac{Y_e}{\nu'_{e,r} M_e}, B \frac{\sum_p Y_p}{\sum_p \nu''_{p,r} M_p} \right) \right]. \quad (2.40)$$

The empirical constants $A = 4$ and $B = 0.5$ were determined experimentally. The indices e and p denote reactant and product properties, respectively. Thus, Equation (2.40) determines the reaction rates of a global reaction r for the EDM [44]. The chemical source term is then derived from the sum over all reactions, as:

$$\overline{S}_\alpha^{\text{EDM}} = M_\alpha \sum_{r=1}^{N_r} (\nu''_{\alpha r} - \nu'_{\alpha r}) \overline{RR}_r^{\text{EDM}} \quad (2.41)$$

In the near-wall region of turbulent no-slip boundary walls, ω may increase significantly. In this case, the reaction rate increases to very high values. This causes the EDM combustion model to produce unphysical behaviour in the near-wall region, such as ignition at boundaries or flame movement along the wall. In order to prevent such results, the inverse of the turbulent mixing time $\frac{1}{\tau_t} = \omega$ is limited by an upper boundary L_{mix} , see equation(2.40). L_{mix} is referred to as the mixing rate limit of the EDM combustion model. For methane/air mixtures, $L_{\text{mix}} = 2,500 \text{ s}^{-1}$ constitutes a reasonable value. The EDM combustion model does however not account for non-equilibrium effects [31], which may produce erroneous results in case chemical kinetics limit the reaction rate. By coupling EDM with a chemistry-dominated model, these weaknesses can be partially improved. EDM is often used in combination with the Finite Rate Chemistry (FRC) Model, allowing for correction of overpredicted reaction rates [37, 63]

The Finite Rate Chemistry Model

The **Finite Rate Chemistry (FRC) Model**, in contrast to the EDM, considers chemical reactions occurring at a finite rate. In this model, reaction rates are determined based on velocity coefficients, calculated under the assumption of laminar chemistry. The FRC Model also accounts for the possibility of reverse reactions [63]. In a mixture consisting of N_r elementary reactions, the reaction rate RR for a reaction r can be calculated as follows [34]:

$$\overline{RR}_r^{\text{FRC}} = k_{f,r} \prod_{\alpha=1}^{N_s} [\alpha]^{\nu'_{\alpha r}} - k_{b,r} \prod_{\alpha=1}^{N_s} [\alpha]^{\nu''_{\alpha r}} \quad (2.42)$$

In Equation (2.42), the concentration of species α is given by $[\alpha] = \frac{\rho Y_\alpha}{M_\alpha}$. The velocity coefficients $k_{f,r}$ for the forward and $k_{b,r}$ for the backward reaction can be calculated using the Arrhenius approach (2.38), as described in Section 2.3.4. Equations (2.38) and (2.42) show that the reaction rate $\overline{RR}_r^{\text{FRC}}$ is a highly nonlinear function, dependent only on temperature and species concentration. The source term for the component equations, similar to EDM, is given by [44]:

$$\overline{S}_\alpha^{\text{FRC}} = M_\alpha \sum_{r=1}^{N_r} (\nu''_{\alpha r} - \nu'_{\alpha r}) \overline{RR}_r^{\text{FRC}} \quad (2.43)$$

The FRC model is advantageous for laminar flows for slow chemical time scales, as the chemical timescale here is greater than the mixing duration. In mixing processes, there are areas with laminar structures as well as areas with intensive mixing and strong turbulence. The reaction rates of the EDM and FRC methods are computed a priori independently of each other. The combined EDM/FRC combustion model then takes the minimum value of both reaction rates in order to determine the reaction rate source term of the species conservation equations [63].

The Eddy Dissipation Concept

The **Eddy Dissipation Concept (EDC)** Model, developed by Magnussen [81], is an extension of the EDM, allowing for the inclusion of detailed reaction mechanisms in the modelling of turbulent flows [83]. The EDC Model is analogous to the concept of energy cascades and vortex decay in turbulent flow. It is based on the transport of turbulent energy from large turbulence structures to dissipation in the smallest structures. The EDC Model divides the entire flow domain into a reaction zone and the surrounding fluid, assuming that reactions occur only in the smallest turbulent structures, the so-called fine-scales. These fine-structures are treated as homogeneously mixed reactors, based on the assumption that the mixing speed within the fine-structures is significantly higher than the transfer rate between the fine-structures and the surrounding fluid. This transfer rate M_{tr}^* is calculated from the dissipation rate ϵ and the kinematic viscosity ν as [84, 85]:

$$M_{\text{tr}}^* = \frac{1}{C_\tau} \sqrt{\frac{\epsilon}{\nu}} \quad (2.44)$$

where $C_\tau = 0.4082$ is a constant of the characteristic residence time, which can be directly calculated from the transfer rate as:

$$\tau^* = \frac{1}{M_{\text{tr}}^*} = C_\tau \sqrt{\frac{\nu}{\epsilon}} \quad (2.45)$$

To quantify the proportion of the fine-structures in the total mass, it is assumed that the fine-structures concentrate in regions of constant energy. The proportion ζ^* of the fine-structures is modelled by the expression:

$$\zeta^* = C_\zeta \cdot \sqrt[4]{\frac{\nu\epsilon}{k^2}} \quad (2.46)$$

where $C_\zeta = 2.1377$ is another model constant, and the mass fraction is derived from Equation 2.46 as $(\zeta^*)^3$.

The mass transfer rate \dot{R}_α of a species α between the surrounding fluid and the fine-structures is calculated as:

$$\dot{R}_\alpha = \frac{\rho(\zeta^*)^2}{\tau^* [1 - (\zeta^*)^3]} (Y_\alpha^* - Y_\alpha) \quad (2.47)$$

Here, Y_α^* and Y_α denote the species mass concentrations within the fine-structures and in the surrounding fluid, respectively [85]. The chemical source term resulting from the EDC Model corresponds to the mass transfer rate determined in Equation 2.47 and is thus given by $\bar{S}_\alpha^{\text{EDC}} = \dot{R}_\alpha$.

The EDC Model enables the inclusion of detailed reaction mechanisms in the modelling of turbulent flows. While the use of the EDC Model allows for the incorporation of detailed reaction mechanisms, the resulting numerical system becomes very stiff, requiring high computational power. Therefore, the model should only be used when the assumption of fast chemistry is invalid.

2.4 Spatial and Temporal Discretization

For solving the continuous system of governing equations, numerical approximation with the help of spatial and temporal discretization schemes is required. The general idea

behind discretization is dividing the domain into a grid and then replacing derivatives in the governing equation with difference quotients. Different types of grids have their own advantages and disadvantages in terms of both complexity and accuracy of the mesh generation process. There are three main discretization schemes namely finite-difference, finite-volume, and finite-element method.

FVM evaluates elliptic, parabolic, or hyperbolic partial differential equations and is the most popular and widely used approach in CFD [86]. The FVM discretization can be implemented by adopting a vertex-centred approach, where vertices of the control volume are centroids of the mesh elements, or a cell-centred approach where control volumes coincide with elements, as depicted in Figure 2.6 for the two-dimensional case. After domain decomposition, an integral formulation of the governing equations and an approximation by numerical integration is needed for each control volume.

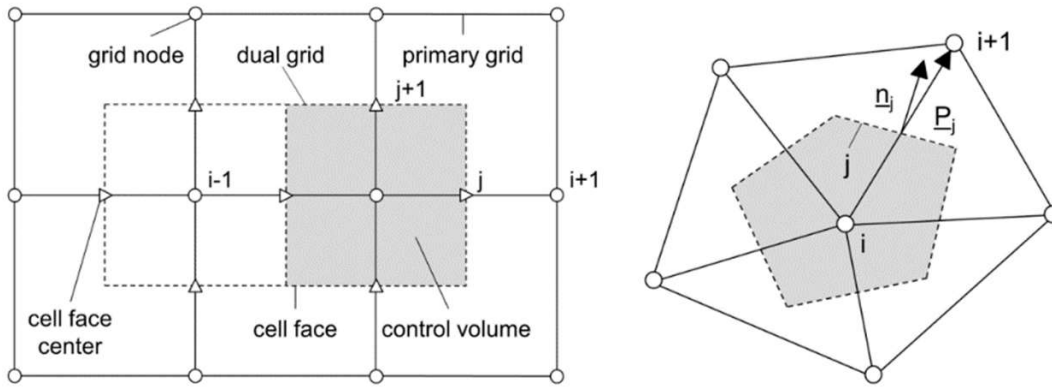


Figure 2.6: Two-dimensional geometrical overview of the dual grid (details available in [2]) used by ThetaCOM

ThetaCOM uses a cell-centred FVM formulation, variables are stored only at the grid cell centres, meaning the values at the cell faces must be approximated from the nodal values. This approximation is carried out by assuming a constant pressure correction gradient along the cell faces.

Since the governing equations are nonlinear and coupled to each other, the solution process involves iterations wherein the entire set of governing equations is solved repeatedly until the solution converges. Depending on the desired accuracy and computational resources available, spatial discretization schemes like first-order upwind, second-order upwind, central differencing, and third-order MUSCL (Monotone Upstream Central Schemes for Conservation Laws) can be implemented. Desired quantities at cell faces are computed using a multidimensional linear reconstruction approach, where higher-order accuracy is achieved at cell faces through a Taylor series expansion of the cell-centred solution about the cell centroid, using a second-order upwind scheme [86]. For transient simulations, the governing equations must be discretized in both space and time. The spatial discretization for the time-dependent equations is identical to the steady-state case. Temporal discretization involves the integration of every term in the differential equations over a time step Δt .

A generic expression for the time evolution of a variable ϕ is given by:

$$\frac{\partial \phi}{\partial t} = F(\phi) \quad (2.48)$$

where the function $F(\phi)$ incorporates any spatial discretization. If the time derivative is discretized using backward differences, the first-order accurate temporal discretization is given by:

$$\frac{\phi^{n+1} - \phi^n}{\Delta t} = F(\phi) \quad (2.49)$$

Once the time derivative has been discretized, a choice of numerical integration scheme must be made for evaluating $F(\phi)$.

Implicit Time Integration

One method is to evaluate $F(\phi)$ at the next time instance:

$$\phi^{n+1} = \phi^n + \Delta t \cdot F(\phi^{n+1}) \quad (2.50)$$

This implicit equation is computed iteratively at each time instance before moving to the next time step. The advantage of the fully implicit scheme is that it is unconditionally stable with respect to time step size.

Explicit Time Integration

$F(\phi)$ is evaluated explicitly (based on the existing solution of the dependent variable) and ϕ^{n+1} can be expressed explicitly in terms of the existing solution as follows:

$$\phi^{n+1} = \phi^n + \Delta t \cdot F(\phi^n) \quad (2.51)$$

A time step is limited by the Courant-Friedrichs-Lewy condition. For high accuracy and solution stability, all cells in the domain must use the same time step, which must be the minimum of all the local time steps in the domain [40]. It is implemented predominantly to capture the transient behaviour of discontinuity, such as shocks, due to its computational economy compared to implicit scheme in such cases. The coupled set of governing equations are discretized in time for both steady and transient cases. However, in the steady case, it is assumed that time marching proceeds until a steady-state solution is reached [2].

2.5 Numerical flow and combustion code - ThetaCOM

The DLR proprietary combustion CFD code, ThetaCOM (Turbulent Heat Release Extension of the TAU code for COMbustion), serves as the foundational tool for all simulations conducted in this study. ThetaCOM adopts a 3D FVM discretization method and includes a dual grid approach, enabling the calculation of flows on structured, unstructured, and hybrid grids [31]. Operating on a collocated grid, ThetaCOM simultaneously computes velocity, pressure, and scalar variables at the same spatial locations. A dual grid is generated from the primary grid nodes, establishing control volumes around the vertices of the primary grid. Variables are stored in the cell centres (nodes of the primary grid) using a cell-centred arrangement, as illustrated in Figure 2.6. The code incorporates an automatic grid adaptation module and supports parallel computations through a domain decomposition approach.

Originally designed for incompressible reactive steady and unsteady flows, ThetaCOM features a pressure-based core solver [2]. It employs the SIMPLE (Semi-Implicit Method for Pressure-Linked Equations) approach for steady incompressible flows with variable density and implements the incompressible projection method for unsteady and incompressible fluid and combustion dynamics [31]. The system of partial differential equations is transformed into algebraic systems using the FVM, solved by matrix-free linear solvers like PBCGS (Preconditioned Bi-Conjugate Gradient Stabilized), GMRES (Generalized Minimal RESidual), Multigrid method [87], and the Jacobi solution algorithm.

The algebraic system of equations yields discrete values that are stored at the nodes. Additionally, fluxes at control volume cell faces, such as mass flux, are determined. These surface flux values, assumed to be constant along control volume interfaces, are computed using an arithmetic average of adjoining nodal values. ThetaCOM offers four different spatial discretization schemes for computing the convective terms of the momentum and scalar equations [2]:

- The first-order accurate Upwind Difference Scheme (UDS)
- The Central Difference Scheme (CDS)
- The Linear Upwind Difference Scheme (LUDS)
- The Quadratic Upwind Difference Scheme (QUDS)

Although the QUDS scheme is formally of third-order accuracy, the midpoint rule is used to determine the mass flux at the control volume interfaces, which is of second-order accuracy. Thus, the spatial accuracy of the discretized convective terms when using the QUDS scheme is apparently reduced to an order of $O(2) < O < O(3)$. The diffusive terms are discretized by means of the second-order CDS scheme.

Temporal discretization schemes in ThetaCOM include the first-order explicit and implicit Euler schemes, as well as the second order three points backward (TBP) and Crank-Nicolson schemes. The code also incorporates stiff chemistry solver schemes [2] with various combustion models, allowing for the calculation of both global and detailed chemistry. ThetaCOM capabilities extend beyond the basics, encompassing convective heat and species transport, diffusion of multispecies flows, turbulence-chemistry interaction (TCI), pollutant formation, multiphase flows, ignition behaviour, gas volume, and solid surface heat radiation. Furthermore, it accommodates various RANS, hybrid RANS-LES, and pure LES turbulence models [31].

Chapter 3

Single-nozzle FLOX[®] burner

This chapter elaborates on the single-nozzle FLOX[®] burner, crucial to our study, by detailing its structural design and operational principles, supported by insights from various investigative studies. Additionally, it explores the role of hydrogen as a gas turbine fuel, examining its impact on combustor performance and emissions, alongside challenges such as flame flashback and dynamic instabilities.

3.1 Combustor Design

The single nozzle set-up, as depicted in figure 3.1, comprises three identical segments, each extending $20D$ in height and characterized by a rectangular cross-section with dimensions of $5D \times 4D$ [20,88]. Central to the combustor's design is a straight stainless steel air nozzle, possessing an inner diameter of $1D$. The nozzle's tip is chamfered, projecting $2D$ above the baseplate, and is notably positioned off-centre. In this work, the fuel nozzle was installed concentrically inside the air nozzle and was arranged in three different configurations to vary the level of mixedness. In the first, non-premixed case, the fuel and air nozzles were flush at the nozzle exit. In the second, technically premixed case, the fuel nozzle terminated $L_{\text{mix}} = 5D$ below the air nozzle exit. A third, fully premixed case was also achieved by injecting fuel into the air delivery line via an inline-mixer upstream of the nozzle exit. This strategic placement aims to emulate the flow dynamics around a single nozzle, thereby facilitating a large recirculation zone on one side of the jet, a phenomenon corroborated by Lammel et al.(2012) [89].

3.1.1 Operational Principles

The burner's operational principle is characterized by the emission of high momentum jets through orifices arranged in a circular fashion, leading to strong recirculation within the combustion chamber [89]. This design ensures intense mixing of the burnt gas with the incoming fuel/air mixture, enhancing flashback resistance by avoiding low velocity zones, thus favouring the burner's application across a wide range of fuels, especially those with medium to high hydrogen content [90].

This approach is recognized as a competitive alternative to swirl-stabilized flames due to

its robust resistance against thermo-acoustic instability and flame flashback [91], while also achieving significant fuel versatility and reduced NO_x emissions [92]. "FLOX[®] combustors" specifically refers to combustion systems designed around a principal idea: flames are stabilized through the intensive mixing of fuel and oxidizer, achieved by strong flow recirculations induced by high-momentum jets injected into the combustion chamber. Experimental investigations have tested a variety of combustor designs with different nozzle configurations, operating under both normal and elevated pressures. These designs have included setups using (partially) premixed air and gaseous fuels, such as methane and hydrogen, featuring single, linearly aligned, or circularly arranged multiple nozzles, some with [93] and some without a pilot flame [91, 92, 94]. Studies have also covered combustors that use liquid fuels, employing both single and multiple nozzle systems [95]. Specifically, the research into a single-nozzle FLOX[®] combustor aimed at understanding the fundamental dynamics of flame stabilization under the FLOX[®] principle, highlighted significant insights into periodic jet oscillations, raising concerns over potential instability sources within FLOX[®] combustors that could restrict their operational range [96].

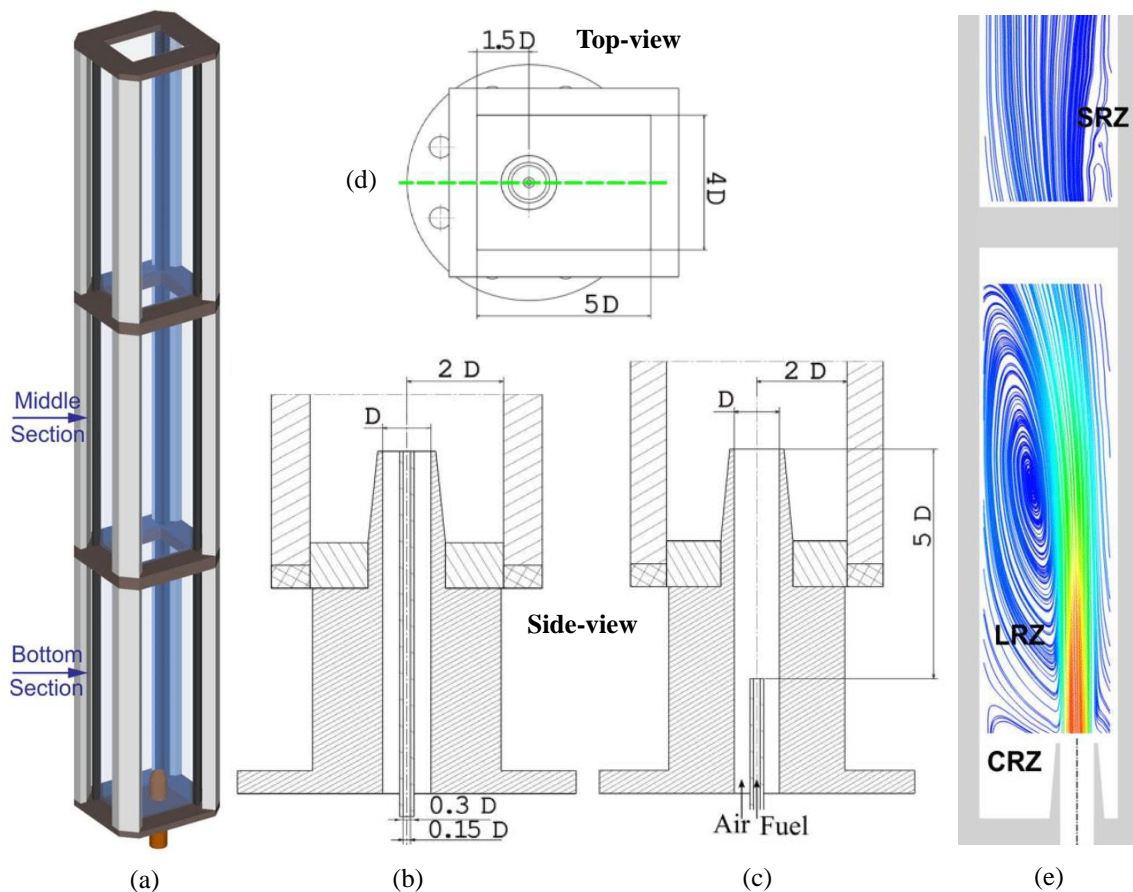


Figure 3.1: Schematics of the single-nozzle burner: (a) combustion chamber (b) Non-premixed config. (c) Technically Premixed config. (d) Top view (e) Recirculation zones in a Jet-stabilized burner, adapted from [20, 88]

The phenomenon of laminar and turbulent jets confined and exhibiting self-excited oscillations has been thoroughly documented. The consensus is that such oscillations are initiated by blocked shear layers, with a feedback loop between initial disturbances and their points of impact sustaining them. The behaviour and occurrence of jet oscillation

largely depend on the jet's velocity and the configuration of its confinement. Primary oscillation modes include jet flapping in planar jets under rectangular confinement [97] and jet precession in round jets within cylindrical chambers, leading to induced swirling flows. These oscillations significantly influence the flow field, notably enhancing jet spread and the large-scale entrainment of surrounding fluid, while reducing fine-scale mixing. In reacting flows, these dynamics offer several advantages, such as expanded flame volumes, decreased flame temperatures, and lower NO_x emissions, due to reduced overall flame strain [97]. Despite widespread interest, the implications of jet oscillation on combustion stability have yet to be fully explored.

3.1.2 Flame Stabilisation

To meet contemporary emissions standards, today's gas turbines for burning gaseous fuels are equipped with lean premixed combustion systems. This approach mixes the fuel with an excess amount of air, leading to lower flame temperatures and, consequently, reduced emissions of pollutants, especially nitrogen oxides (NO_x). However, this setup results in decreased flame speed. The pursuit of high power densities leads to elevated flow speeds in the combustion chamber, making flame stabilization through diffusion alone inadequate due to insufficient heat and radical transport to the yet-to-burn air-fuel mix [98]. Therefore, modifying the combustion chamber's flow to create recirculation zones is essential. These zones enhance the convective return of hot gases and radicals to the burner's exit, mixing with the unburned gas mixture to heighten reactivity and enable stable, low-emission burning even at high speeds. This method also permits a more compact design of the combustion chamber.

For consistent combustion over a broad operational spectrum, designing the chamber with multiple burner stages, typically incorporating a pilot and a main stage, is advisable. The pilot stage aids in ignition and stabilizes the main stage during lean operations. Enhanced flame stabilization is achievable through swirl or jet stabilization techniques, which are elaborated further.

Swirl-stabilised combustion

In systems with swirl-stabilized combustion chambers, the incoming air or air-fuel blend is given a rotational motion around the main flow direction, before it enters the chamber. This is achieved using a device known as a swirl generator for basic applications, while more advanced setups may employ multiple such devices. The induced swirl generates a pressure gradient within the chamber, creating a pronounced recirculation zone along the chamber's central axis. This zone, characterized by its highly turbulent shear layers, allows for the stabilization of the flame front even at elevated flow speeds. The swirl effect causes the reaction zone in these burners to adopt a V-shaped configuration. Swirl flames are preferred in various combustion applications due to their enhanced flame stability across a wide range of Reynolds numbers [98]. This stability is largely attributed to the vortex-induced recirculating flow, which brings hot combustion products back to the flame's base, as shown in figure 3.2. Here, they help maintain continuous ignition and stabilize the flame by mixing with incoming fresh fuel and air.

Swirl flames are characterized by high power density and a broad operating range [98]. Its

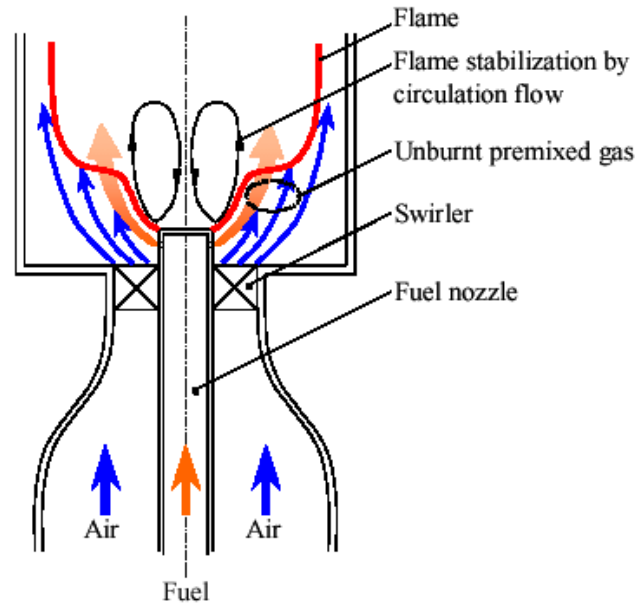


Figure 3.2: Swirl-stabilized combustor schematic [3]

unsteady behaviour may trigger resonance with the combustor acoustics modes and lead to thermo-acoustics instabilities.

Jet-stabilised combustion

To ensure stable combustion across a wide operating range, it is usually sensible to design the combustion chamber with several burner stages. Typically, a pilot stage is combined with a main stage. The pilot stage is used during ignition and to stabilize the main stage, especially in lean partial load operation.

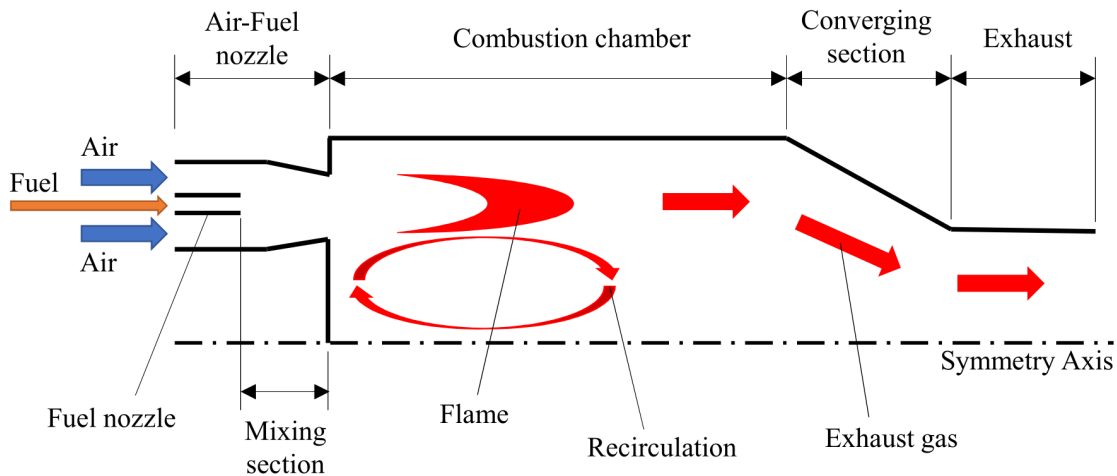


Figure 3.3: Schematic of the jet-stabilized FLOX[®] burner principle [4]

The core of jet-stabilized combustion systems lies in the injection of the air-fuel mixture into the combustion chamber through nozzles arranged in a circular pattern, imparting high axial momentum. This design fosters a significant recirculation zone along the combustor's

axis, evident in Figure 3.3, where unswirled, partially premixed gas jets, imparted with substantial axial momentum, create a recirculation area. This area brings hot exhaust gases from the reaction zone back to the burner exit, mixing with the unburned air-fuel mixture in the turbulent shear layers of the jet flow. Such mixing, coupled with high recirculation rates, effectively stabilizes the flame. However, it also dilutes fresh air, moderating reaction rates and expanding the reaction zone within the combustion chamber. Consequently, a more homogeneous temperature field emerges, slightly surpassing the adiabatic flame temperature of the global mixture, laying the groundwork for reduced NO_x emissions characteristic of this combustion type [99–101].

Exploring alternatives, concepts like flameless combustion, represented by MILD, FLOX, or HiTAC combustion, have gained attention for their potential to further reduce NO_x emissions and combat combustion instabilities. These approaches are distinguished by a homogenized flame zone and minimized temperature peaks, complying to recirculation induced by high momentum confined jets [100, 102–104]. In the absence of auxiliary stabilization methods like pilot flames or external ignition sources, flame propagation and autoignition emerge as the principal mechanisms for flame stabilization. While these mechanisms often work in tandem, their contributions vary across different flame regions. Despite the known importance of these processes, the intricate dynamics within turbulent flames and how autoignition and flame propagation interact remain under-explored. This gap underscores the necessity for robust numerical models, which in turn require empirical data from well-defined experimental setups [105].

To shed light on the dynamics of flameless combustion and its stabilization mechanisms, extensive research has previously been conducted under simplified conditions. Jet-in-hot-co flow (JHC) configurations have been a focal point, simulating the intense mixing characteristic of practical systems through a co-flow of vitiated air around a central fuel or fuel-air jet [104, 106]. While MILD combustion’s peak temperatures remain below $1600\text{ }^\circ\text{C}$, modern gas turbines target inlet temperatures above this threshold, presenting a distinct context for the present investigation. Notably, the flames examined here feature distinct flame fronts, diverging from the flameless paradigm yet incorporating its essential aspects like dilution with exhaust gas, extended flame zones, and lower NO_x emissions. The development of jet-stabilized burners for large gas turbines, leading to a large central recirculation zone crucial for flame stabilization, originates from these considerations. Though not strictly flameless, the resulting FLOX[®] combustor shares key attributes with flameless combustion, like dilution of fresh charge with exhaust gas, extended flame zone and reduced emissions, as evidenced in high-pressure tests across various configurations [107, 108].

3.2 Hydrogen as a gas turbine fuel

The combustion of H₂ yields potentially zero carbon emissions, making its widespread adoption in the energy sector highly desirable, particularly with the aim of modifying existing combustion systems originally designed for natural gas to function with up to 100 vol.% H₂ [15,75]. In the aviation industry, H₂ is considered a promising substitute for fuel cells and Sustainable Aviation Fuel (SAF) for aircraft up to the mid-range passenger jet category [109]. Given the significant opportunities and the undeniable challenges associated with transitioning to H₂ combustion, there is a need to enhance our comprehension of H₂ combustion dynamics within gas turbine combustors for both stationary energy generation and aviation applications. This section delves into the thermal, transport and chemistry characteristics of hydrogen-rich fuel mixtures.

3.2.1 Thermophysical properties

The transport characteristics of fuels play a critical role in defining the dynamics of combustion and the attributes of flames. Specifically, thermal and mass diffusivity, with their non-dimensional ratio and the Lewis number, are important in this context. Hydrogen is notably distinguished by its transport characteristics among various fuels. Its heat and momentum diffusivity are approximately an order of magnitude higher than those of CH₄, CO, and even air. Moreover, hydrogen’s diffusion rate in air is about four times greater than that of CH₄ and CO [16]. While CH₄ and CO exhibit comparable transport properties, their densities differ significantly. This disparity in density is minimized in the context of premixed fuels, especially under lean conditions where the fuel’s mole fraction is generally lower than that of the oxidizer (dilute fuels).

Hydrogen, as a single-component fuel, exhibits unique chemical characteristics. In combustion processes, its chemical reactivity far exceeds that of natural gas, leading to higher flame speeds and temperatures (refer to Table 3.1). A more detailed exploration of these combustion-related properties is provided.

Table 3.1: Fuel properties of hydrogen, natural gas, and methane [9–11]

Fuel/combustion property	Unit	Hydrogen	Natural gas	Methane
Density at 300 K, 1.1013 bar	kg/m ³	0.082	0.7–0.9	0.651
Flammability limits in air	vol.%	4–75	4.5–13.5	5–15
Flammability limits (Φ)	-	0.1–7.1	0.55–1.6	0.4–1.6
Specific lower heating value (LHV)	MJ/kg	120	38.9–47.1	50
Molar lower heating value (LHV)	MJ/m ³	10.8	31–41	35.9
Maximum laminar flame speed	m/s	3.25	0.4–1.5	0.45
Adiabatic flame temp. ($\Phi = 1$)	K	2370	1950–2000	2226
Thermal diffusivity	10 ⁻⁶ .m ² /s	159.4	20–25	24.56
Mass diffusivity (in air)	10 ⁻⁶ .m ² /s	77.92	16–19	22.39

Flammability range

Hydrogen possesses a notably broader volumetric flammability range than natural gas, with lean extinction occurring at reduced equivalence ratios, a consequence of its enhanced chemical reactivity and diffusivity. Additionally, hydrogen's upper flammability limit is significantly greater in fuel-rich conditions.

Heating value

Regarding energy content, the mass-specific lower heating value (LHV) of hydrogen can be up to three times that of natural gas. Nevertheless, hydrogen's lower molar density results in a considerably reduced molar LHV, impacting overall engine performance.

Ignition delay

The ignition delay period is defined as the available time for mixing fuel with air before ignition starts. This duration is influenced by the fuel composition, the ambient temperature, and the pressure. Extending the ignition delay allows the flame to move lower and supports enhanced premixing. Notably, the presence of hydrogen in the fuel mix substantially reduces ignition delay times across all temperature ranges [51]. An increase in pressure tends to shorten the ignition delay in both high temperature ($T > 1350$ K) and low temperature conditions ($T < 1000$ K) [5]. Auto-ignition describes the process by which a fuel-air combination shifts from being non-reactive or slowly reactive to undergoing self-sustained combustion [110].

3.2.2 Fundamental flame characteristics

During the development phase of a combustion chamber, it is necessary to focus on specific combustion phenomena. This encompasses early assessments of adiabatic flame temperatures and the potential for flame flashback and auto-ignition, particularly within the context of premixed combustion designs. Such preliminary evaluations facilitate the early comparison and selection of different conceptual approaches.

Flame speed

The laminar flame speed, a key characteristic of flame behaviour, denotes the rate of flame propagation in a mixture of premixed reactants. The peak laminar flame speeds are achieved at different equivalence ratios (Φ) for different fuels or fuel blends. Specifically, hydrogen's maximum laminar flame speed is observed at $\Phi = 1.80$, whereas for methane, this peak speed occurs at $\Phi = 1.08$. The influence of the equivalence ratio on laminar flame speed is notably more pronounced for hydrogen and its mixtures [6]. Figure 3.4 shows typical unstretched laminar flame speeds for common fuels as a function of the equivalence ratio.

Hydrogen's flame speed can be an order of magnitude greater than that of other fuels. This enhanced speed results from the superior molecular diffusivity of H_2 and H radicals within hydrogen flames compared to those in other fuel flames, as detailed in Table 3.1. Additionally, the heightened chemical reactivity, owing to the increased pool of critical radicals such as H, O, and OH contributes to this phenomenon [16]. Figure 3.4 also demonstrates how burning velocity escalates with rising hydrogen content. The addition of hydrogen not only alters the unstretched laminar burning velocity, as discussed previously, but also significantly impacts how the flame responds to stretch rates. The stretch rate of

a flame is affected by a combination of hydrodynamic strain and the curvature of the flame front. For a detailed comparison, readers are recommended to refer Ramanan et al. [111].

While the laminar flame speed is an intrinsic property of a fuel that is determined by the mixture's chemical and transport characteristics. In contrast, the turbulent flame speed is influenced by flow properties such as turbulence intensity, resulting in an accelerated magnitude that exhibits a sublinear relationship, a phenomenon referred to as the bending effect [112,113]. The dynamic interplay between chemical kinetics and turbulence is termed turbulence-chemistry interaction.

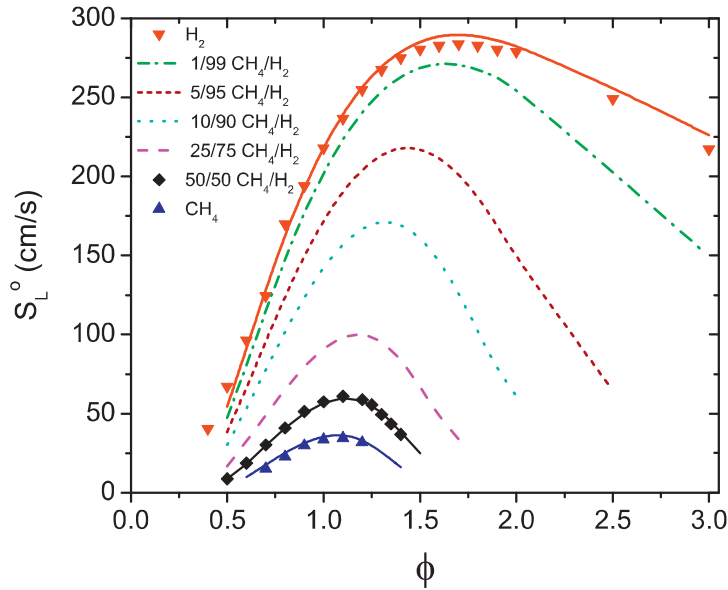


Figure 3.4: Laminar flame speed comparison of pure and blended CH_4 and H_2 at various equivalence ratios at 300 K and 1 atm in air. Points are experimental data, and lines are from the kinetics model, adapted from [5, 6]

Adiabatic flame temperature

The peak temperature within a combustor holds significant practical relevance, as it directly impacts the gas turbine's performance, specifically its efficiency (as reflected by the ideal Carnot efficiency via the turbine inlet temperature), and the generation of NO_x emissions. Moreover, this temperature is crucial in determining suitable materials for constructing and coating both the combustion chamber and turbine blades.

A key measure of this temperature is the adiabatic flame temperature, defined as the equilibrium temperature attained by combustion products when reactants combust at constant pressure and no heat exchange with the environment. This calculation typically assumes complete reactions and a limited number of stable reaction products [69], excluding the explicit consideration of dissociation in reaction products and pollutants. Adiabatic flame temperatures for specific fuel-oxidizer combinations are often computed across a range of equivalence ratios, as illustrated in Figure 3.5.

Upon examining the adiabatic flame temperatures for CH_4 , CO , and H_2 as depicted in Figure 3.5, it is evident that among these pure fuels, H_2 exhibits a comparatively high flame temperature under stoichiometric conditions, while CH_4 records the lowest. This observation can be linked to methane's higher oxidizer demand on a molar basis, resulting in a mixture more diluted with N_2 . Despite CO and H_2 requiring identical oxidizer amounts

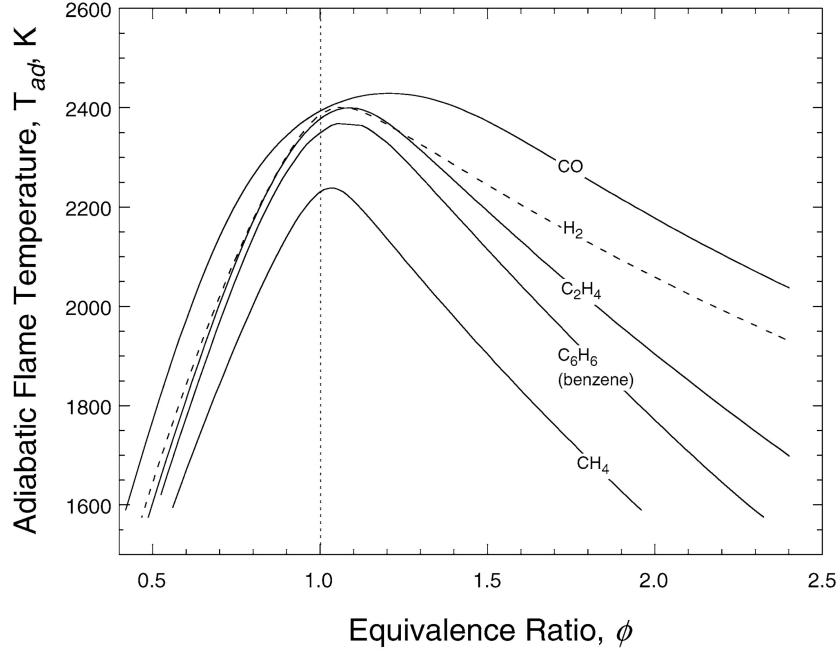


Figure 3.5: Adiabatic flame temperature of different fuels in air at 1 atm, adapted from [7]

for a given Φ , CO's flame temperature marginally exceeds that of H_2 at elevated Φ values due to CO's superior molar heating value. These adiabatic flame temperature calculations are crucial for gauging the thermal stress on components within the combustion chamber.

3.2.3 Standardization of NO_x emissions

The standardization and normalization of NO_x emissions form a critical preliminary step prior to in-depth discussions on emission characteristics. These procedures ensure that comparisons across varied combustion systems are consistent and in adherence to regulatory benchmarks. Specifically, standardization converts emissions to a dry basis, negating the variable water vapour content, while normalization adjusts for ambient oxygen levels, thereby facilitating an equitable assessment of emissions. The conversion methodology is based on the exclusion of water content from the sample, providing an accurate representation of the NO_x emissions generated [66].

The conversion of NO_x emissions from a wet to a dry basis is described by:

$$NO_{x_{dry}} = NO_{x_{measured}} \times \left(\frac{100}{100 - (H_2O)\%} \right) \quad (3.1)$$

where $NO_{x_{dry}}$ is the dry basis NO_x concentration, $NO_{x_{measured}}$ is the measured NO_x concentration on a wet basis, and $(H_2O)\%$ is the percentage of water vapour in the exhaust gases.

For stationary gas turbines, NO_x measurements are corrected to 15% O_2 [66]. The normalization of NO_x emissions to 15% O_2 utilizes the formula:

$$\text{NO}_{x_{\text{normalized}}} = \text{NO}_{x_{\text{dry}}} \times \left(\frac{21 - \text{O}_{2_{\text{measured}}}}{21 - \text{O}_{2_{\text{reference}}}} \right) \quad (3.2)$$

Here, $\text{NO}_{x_{\text{normalized}}}$ denotes the NO_x concentration normalized to 15% O_2 , $\text{O}_{2_{\text{reference}}}$ is the reference oxygen concentration, and $\text{O}_{2_{\text{measured}}}$ is the actual oxygen concentration measured in the exhaust gas.

The calculated NO_x emissions must comply with the European Union regulations concerning produced NO_x pollution. The current legislation for gas turbines using gaseous fuels other than natural gas specifies a limit of 200 mg/Nm³ [74]. However, in new gas turbines, this limit is 75 mg/Nm³ [74]. To ensure legislative compliance, NO_x measurements are typically converted to ppm (parts per million) on a volume basis as follows [114]:

$$\text{ppm} = \frac{\text{Concentration in mg/Nm}^3 \times 22.414}{\text{Molecular weight of NO}_x \text{ (g/mol)}} \quad (3.3)$$

In this equation, 22.414 represents the molar volume of an ideal gas at standard conditions (i.e., 298.15 K and 1 atm), and the molecular weight of NO_x is considered based on the specific nitrogen oxide being measured, typically NO or NO_2 . For instance, the molecular weight of nitrogen dioxide (NO_2) is 46 kg/kmol. Using this molecular weight, results in a concentration of 97.45 ppm NO_x for existing gas turbines and 36.54 ppm for new gas turbines.

3.3 Effects on combustion stability

Ensuring combustion stability is essential for the optimal and secure operation of gas turbines. This segment delves into the dynamic interactions between the fuel combustion and the physical environment within the combustion chamber, a key factor in sustaining stable combustion. It highlights the difficulties arising from issues such as thermo-acoustic oscillations, flashback, and LBO, all of which can significantly impact the system's reliability and performance.

3.3.1 Lean blow-off

Contemporary premixed gas turbine combustors are mainly operated in lean conditions to lower combustion temperatures and NO_x emissions [19, 67]. Nonetheless, operating near the LBO limit poses risks, including flashback and combustion instabilities characterized by local flame extinction and variability in heat release. These factors adversely affect the combustor's performance and operability. In particular, fluctuations in heat release, if synchronized with the acoustics of the system, may lead to significant fluctuations in pressure and velocity, increasing the risk of flashback, especially with fuels that have a high flame speed, such as hydrogen.

Instabilities at the flame front play a pivotal role in the blow-off process, with flame pulsations and flickering often observed prior to blow-off [115]. However, fully understanding LBO presents challenges and necessitates further investigations [116]. This

complexity is more pronounced with mixed fuels like syngas, which typically comprises hydrogen, carbon monoxide, methane, and other gases. Both fluid dynamics and chemical kinetics are recognized as influencing factors in LBO. Extensive experimental studies consistently demonstrate that increasing the hydrogen mole fraction in a fuel blend lowers the equivalence ratio at which LBO occurs, indicating a leaner mixture at the point of flame extinction [16].

Understanding flame stability requires considering the flame's interaction with vortices, wrinkling, and its ability to hold, as well as how these behaviours relate to the flow field and turbulence levels. Zhang et al. [117] observed that the average flow field structure remains unchanged under various conditions for both methane and hydrogen-enriched flames, implying that chemical kinetics do not significantly influence the flow field structure.

Hydrogen, with its broad flammability range, low ignition energy requirement, and high flame speed, enables stable ultra-lean combustion at temperatures conducive to minimizing NO_x production, without negatively impacting CO and unburned hydrocarbon emissions. Although adding hydrogen could potentially raise NO_x emissions due to increased flame temperatures at constant equivalence ratios, this effect might be mitigated by the capacity to combust leaner mixtures [20, 118].

3.3.2 Flame Flashback

Challenges arise when burning these so-called H_2 -rich fuel gases (with the hydrogen content typically over 70 vol. %) instead of natural gas in the lean-premixed gas turbine combustor, and one of the operability issues is the higher propensity for flashback [113].

Flashback arises when the flame propagates from the combustion zone back into the premixing zone of the combustor. This phenomenon significantly elevates the temperature within the premixer, a component not engineered to withstand such conditions. Moreover, should the flame stabilize in the wake of structural elements within the premixer's passageways, it poses a severe risk of damage to the gas turbine. At least four distinct mechanisms can lead to flashback in gas turbine premixers [112, 119–121]:

1. **Core flow flashback**

Flashback within the core flow is triggered when the turbulent flame's propagation speed surpasses the local flow velocity. The turbulent burning velocity magnitude plays the main role in triggering the core flow flashback and is a function of turbulent flame interaction as well as chemical kinetics [99, 113]. Thus, the fuel's composition and the turbulence pattern are critical in defining the limits for core flow flashback occurrence. Although combustors are designed to prevent core flashback by increasing axial velocity, conventional flame stabilization techniques in use might inadvertently facilitate it. Specifically, the application of swirl reduces the axial velocity, and vortex-flame interactions that lead to flame stretching can increase the turbulent burning velocity [119].

2. **Combustion instability induced flashback**

Flashback triggered by combustion instability is a consequence of significant fluctuations in the flow field's amplitude [113]. Such instabilities arise from interactions

among acoustic modes, variations in heat release, and highly turbulent flow. Oscillations in pressure and velocity, linked to these instabilities, can mobilize the flame and create substantial vortices, thereby causing flow reversal [112], a precursor to flashback.

3. Combustion induced vortex breakdown

CIVB flashback stands as a common occurrence in swirl-stabilized gas turbine combustors. This phenomenon is distinguished by vortex breakdown, a key characteristic of swirling flows, which is contingent upon the swirl number that quantifies the degree of swirl intensity. Exceeding a critical swirl number prompts the onset of vortex breakdown [120, 122]; lacking this, reverse flow fails to manifest. The rise in azimuthal velocity in comparison to axial velocity triggers vortex breakdown, ensuing from the emergence of a reverse flow zone. Such breakdown signifies a dramatic alteration in the vortex configuration, culminating in a stagnation point and a subsequent recirculation area downstream.

4. Boundary layer flashback

Boundary layer flashback emerges as a predominant flashback mechanism in jet/Bunsen flame configurations. Typically, the free stream velocity within a gas turbine pre-mixer during standard operation surpasses the speed of turbulent flame propagation, preventing the flame from moving upstream within the core flow. However, adjacent to the wall, the flow velocity diminishes due to the no-slip condition, potentially paving the way for flashback initiation. Furthermore, the combustion speed diminishes near the so-called "quenching distance," a region where the flame cannot be sustained because of heat dissipation or stretching effects [123]. Therefore, flashback is triggered at spots where the local combustion velocity sufficiently exceeds the local flow velocity. The phenomenon of boundary layer flashback is analytically represented by the "critical velocity gradient" concept, delineating the propensity for flashback under specific conditions based on the bulk flow velocity at the point of flashback [124, 125]. Studies of boundary layer flashback have explored various conditions, like equivalence ratio, preheat temperature, pressure levels, burner materials, and burner geometrical configurations under both laminar and turbulent conditions.

3.3.3 Dynamic instabilities

Beyond blow-off and flashback, combustion systems, particularly those operating under premixed conditions, are vulnerable to dynamic instabilities. These instabilities often stem from fluctuations in the heat release rate, triggered by variations in the equivalence ratio or inherent unsteadiness within the flow field, such as vortex shedding from separation zones or vortex roll-up along shear layers, compounded by turbulence. Such oscillations in heat release may synchronize with acoustic pressure variations, creating a positive feedback loop that significantly amplifies pressure amplitudes. This phenomenon, known as thermoacoustic instability, poses a challenge to lean premixed combustion strategies [76]. Termed an "innovation trap," this issue has sparked extensive research, which continues to this day [126]. When heat release oscillations align with pressure fluctuations, they can act as an acoustic energy source, potentially causing substantial impacts on the system's hardware due to high sound pressure levels (SPL). The significance of dynamic instabilities has fuelled decades of thorough investigation, yet gaps in understanding persist, particularly

regarding conventional fuels like methane, with relatively less emphasis on hydrogen-rich fuels or syngas.

Changes in fuel composition can notably influence combustion instabilities by altering the flame's shape, local dynamics, or position, thereby affecting the synchronization between heat release and pressure fluctuations for a given flame configuration [68].

Chapter 4

Numerical model description

The computational flow domain model is developed through a structured approach, beginning with the idealization of the CAD model for different nozzle configurations, categorized by their mixing levels at the fuel nozzle exit. This is followed by a mesh generation procedure, along with the specification of boundary conditions, aligned with operating conditions from prior experiments [20]. To ensure the model's accuracy and robustness, sensitivity analyses are conducted, with a focus on establishing mesh independence as detailed in subsection 4.5.

4.1 Computational domain

The investigation of the flow domain within the physical setup, as depicted in Figure 3.1, is essential for understanding the flow field and flame dynamics. The computational domain is defined as a segment extending $40D$ in height with a rectangular cross-section of $5D \times 4D$.

At the core of the combustor design is a jet nozzle with an inner diameter of $1D$, positioned off-centre (with respect to the longer side of the combustion chamber) and demonstrated in Figure 4.1. This specific design, with a chamfered tip and specifications of the fuel nozzle's outer diameter at $OD = 0.3D$ and inner diameters at $ID = 0.15D$, aims to replicate the multi-nozzle FLOX[®] combustor. Such an arrangement is pivotal for inducing a significant recirculation zone on one side of the jet, thereby enhancing the mixing and auto-ignition of unburned fuel (detailed in section 3.1.1). This design strategy ensures a detailed replication of the dynamic flow conditions, facilitating the analysis of their emission characteristics under various operational conditions.

Owing to the intricacies involved, a three-dimensional (3D) modelling approach is adopted in ThetaCOM [31]. Within the scope of this thesis, the combustion chamber is subjected to examination under three distinct configurations, distinguished by their respective levels of mixedness at the nozzle exit:

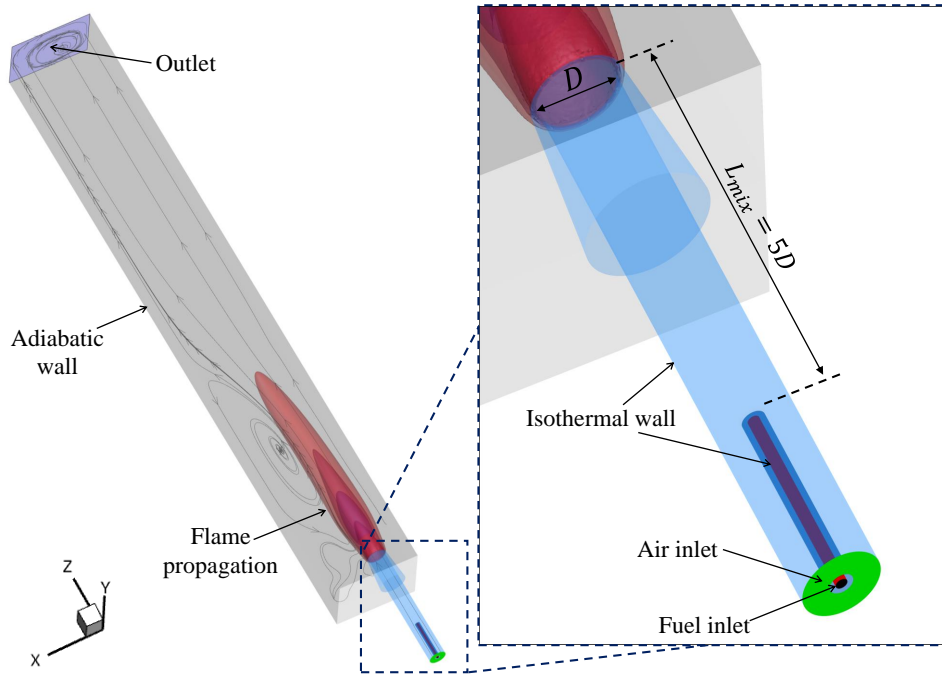


Figure 4.1: Computational domain in 3D for the single-nozzle FLOX[®] burner (Technically Premixed configuration), illustrating the applied boundary conditions

1. Non-premixed (NP): The configuration where fuel and air nozzles are aligned flush at the nozzle exit, with $L_{\text{mix}} = 0$.
2. Technically premixed (TP): In this setup, the fuel nozzle extends to terminate $5D$ below the air nozzle exit, denoted as $L_{\text{mix}} = 5D$.
3. Fully premixed (FP): Achieved through the introduction of fuel into the air delivery line via an inline-mixer positioned upstream of the nozzle exit.

4.2 Operating conditions

As a prerequisite for the RANS analysis, boundary conditions have to be precisely applied to the computational domain (illustrated in Figure 4.1) during the CAD stage by annotating the model's surfaces with specific names (named selections in ANSYS Space claim software). These annotations serve as boundary markers within the boundary mapping file, enabling ThetaCOM to accurately identify and process each surface according to its designated numerical treatment, laying the groundwork for well-posed models.

Walls of the combustion chamber are designated as adiabatic to preclude heat transfer (due to unavailability of precise heat flux values), whereas the walls of the air and fuel nozzles are assigned an isothermal boundary condition, maintaining a constant air preheat temperature of $T_{pre} = 573\text{K}$. To accommodate the nature of viscous flows, a no-slip condition is applied at all wall interfaces, facilitated through the inclusion of the 'turbulent' keyword within the boundary mapping file.

Table 4.1: Operating conditions for the investigation on FF and LF at atmospheric pressure. Specification of \dot{m}_{FP} is the mass flow rate for the FP configuration and \dot{m}_{fuel} , \dot{m}_{air} is valid for both NP and TP

Fuel (vol. %)		Φ	\dot{m}_{fuel} (g/s)	\dot{m}_{air} (g/s)	\dot{m}_{FP} (g/s)	Objective of Investigation
H_2	CH_4					
0	100	0.74	0.21	4.85	5.06	Fuel Flexibility
30	70	0.74	0.195	4.73	4.96	
60	40	0.74	0.17	4.59	4.76	
80	20	0.74	0.14	4.44	4.58	
90	10	0.74	0.12	4.27	4.39	
100	0	0.74	0.09	4.01	4.1	
100	0	0.49	0.06	4.23	4.29	Load Flexibility
100	0	0.3	0.04	4.38	4.41	
100	0	0.21	0.03	4.46	4.48	

For the investigation on FF, each case was examined with a global equivalence ratio of $\Phi=0.74$ with the velocity at the air nozzle exit regulated to $v_{\text{air}} = 105 - 110$ m/s at standard atmospheric pressure. To highlight the influence on combustion chemistry, the single-nozzle FLOX[®] burner has been operated with 100 vol.% CH_4 and 100 vol.% H_2 . At the inflow boundary marker, mass fractions of species were explicitly specified to recreate the desired proportions within the fuel mixture. The specific FF parameters integral in this thesis is also demonstrated in the Table 4.1. LF aspect of this study was exclusively analysed using hydrogen as the fuel, probing the operational adaptability of the burner under varied Φ .

As evident from the Table 4.1, the investigation on FF and LF are conducted across the three distinct nozzle configurations outlined in Section 4.1. This is necessary for understanding the influence of premixing on the lift-off height and NO_x emissions. Such comparative analysis provides valuable insights into the adaptability and performance of the burner and serves as a medium for experimental validation.

4.3 Mesh generation

Creating an optimal mesh is imperative for effectively validating experimental results. The quality and refinement of the mesh substantially affect the fidelity of simulations, impacting factors like accuracy, convergence rates, and computational resource utilization. This study employs ANSYS Meshing's capabilities to identify the ideal mesh refinement level within the reaction zone, focusing on flame lift-off height and emission prediction.

4.3.1 Unstructured meshing for reactive flows

A computational mesh can be broadly classified into two categories, structured and unstructured. Structured grids consist of quadrilaterals (2D) and hexahedrons (3D), which are then lined up in an orderly fashion to fill the flow domain. The position of each cell can be described by an index (usually i, j, k) in space due to the exact neighbourhood relations. The main disadvantage of such meshes is seen in more complex shapes, where the cells often degenerate to fill the flow area, which can then lead to problems with the stability of the chosen numerical method and iterative convergence of the simulation [40]. Unstructured meshes consist of triangular (2D) and tetrahedral, pyramids, prisms (3D) cells.

For combustion simulations, the intricate geometries of burners, fuel injectors, and combustion chambers necessitate a mesh that can conform to curved boundaries and fine features, making unstructured meshes particularly suitable. While unstructured meshes offer significant benefits, they also present challenges. Highly skewed tetrahedra and pyramids near walls and corners, can compromise the accuracy and convergence of solutions. To mitigate these issues, ANSYS Meshing offers tools for quality diagnostics and mesh improvement. Secondly, the compatibility of the solver with the mesh topology must be considered. ThetaCOM supports unstructured grids, ensuring that solver-specific requirements are met. Lastly, the computational cost associated with highly refined unstructured meshes, may result in a significant increase in element counts and computational demands.

4.3.2 Meshing procedure

Following the import of the CAD model into ANSYS Meshing, the GUI presents various components within the structure tree. The meshing procedure incorporates the use of named selections for identifying specific surfaces, such as the combustor walls, air and fuel nozzles, inlets, outlet, and bodies of influence (BOI) for areas like the reaction zone. Utilizing named selections facilitates the targeted application of mesh controls, including face sizing, body sizing, and boundary layer inflation (BLI).

The computational mesh, as illustrated in Figure 4.2, undergoes local refinement through the implementation of curvature size control. This approach adjusts the mesh density to conform to the small nozzle diameter and prevent the formation of highly skewed elements that could degrade simulation accuracy. The mesh is specifically refined in the reaction zone and fuel injection areas, by employing BOI. Given the prevalence of chemical reactions in these zones, marked by significant heat release and the formation of combustion products, these areas exhibit steep gradients in temperature, species concentration, and

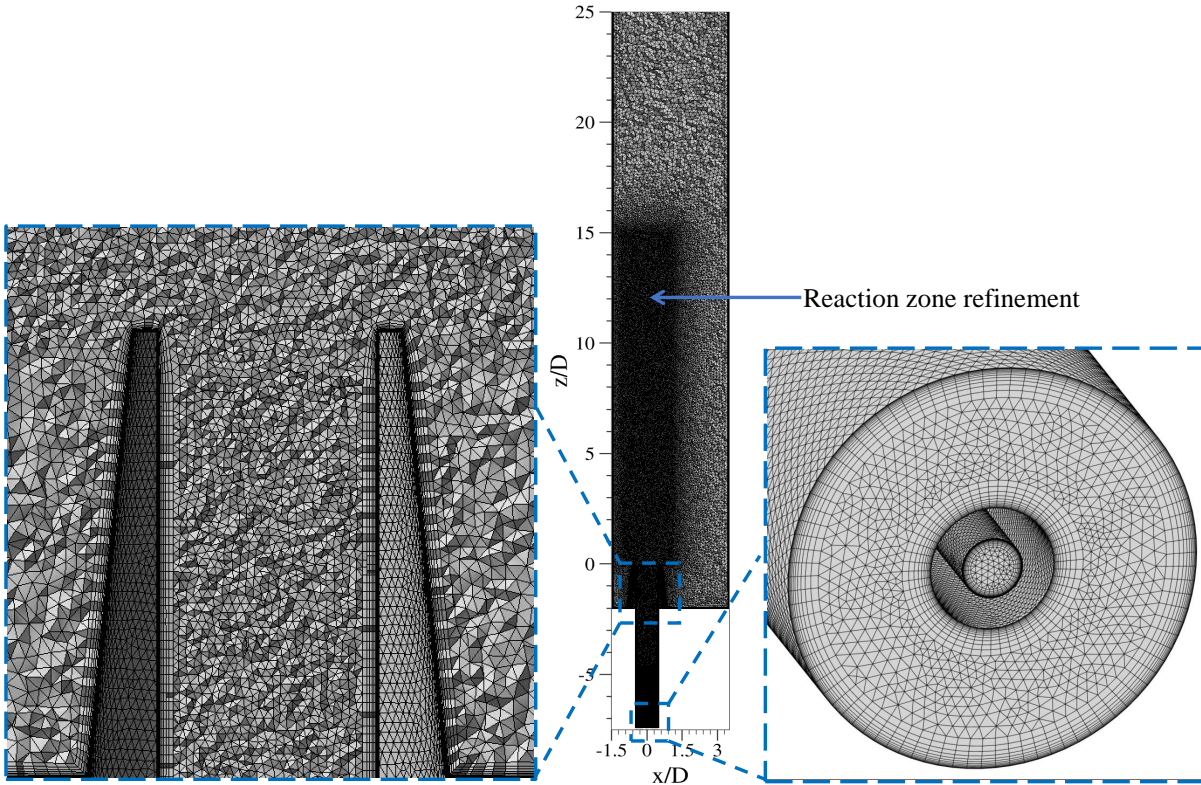


Figure 4.2: Computational mesh for the flow domain (Technically Premixed configuration). The visualization is done on a sectional mid-plane, and the zoom box on the right signifies mesh generated on the inlet.

velocity, alongside rapid shifts in thermodynamic and chemical properties. Accurately capturing these gradients is fundamental for reliable predictions of flame location and emissions. The intricate details of the air and fuel nozzle inlets is highlighted in Figure 4.2 through a zoomed-in section, showcasing the mesh adaptation to capture the nozzle's curvature.

Another fundamental requirement in a CFD mesh is the inflation layer, essential for modelling the no-slip boundary condition and turbulence near the wall. BLI implemented in this study provides a smooth transition from the near-wall mesh to the coarser bulk flow mesh. The application of 15 prism layers with a growth rate of 1.2 ensures the dimensionless wall distance (y^+) is around 1 or below, optimizing the mesh for capturing velocity and gradients near walls.

4.3.3 Quality criteria

In the following subsection, the most important indicators according to which the mesh quality can be assessed are briefly explained. All indicators refer to the used ANSYS meshing programme [127].

1. **Aspect Ratio:** serves as an indicator of mesh cell elongation. Ideal mesh cells exhibit aspect ratios close to unity, reflecting minimal elongation. While aspect ratios up to 100 might be acceptable in regions distant from walls, it is critical to limit the aspect ratio to less than 1500 near wall regions [127].

2. **Skewness:** is a metric that evaluates the deviation of mesh cells from their ideal geometric configuration (i.e., equilateral triangles in 2D and tetrahedrons in 3D). Skewness values approaching 0 are desirable as they indicate cells with optimal geometry, whereas values nearing 1 suggest a high degree of distortion, potentially undermining simulation stability and accuracy.
3. **Orthogonality:** The measure of mesh orthogonality is integral for ensuring precision in the computation of gradients. A mesh with perfect orthogonality exhibits a value of 1, denoting perpendicular grid lines to the cell faces. Suboptimal orthogonality, indicated by values lower than 0.6, can introduce numerical diffusion [127].
4. **Jacobian Ratio:** This criterion evaluates cell shape quality through the determinant of the Jacobian transformation matrix. A positive Jacobian ratio signifies a properly configured cell, whereas negative values indicate inverted cells, which are not permissible. Ensuring a universally positive Jacobian ratio is essential for the integrity of the mesh.
5. **Minimum Face Angle:** The elements undergo a check to identify any distortion characterized by small internal angles, as such distortion can significantly reduce the accuracy of the simulation. To ensure reliable results, the internal angles should always be greater than 20° , thereby preventing the occurrence of deformed cells.

By ensuring these quality metrics, one can ascertain a dependable unstructured mesh. Nonetheless, achieving an optimal balance between computational resource utilization and solution reliability in RANS simulations, is necessary. Thus, a comprehensive mesh convergence study is undertaken within this research to assess the impact of mesh refinement on simulation outcomes, ensuring that accuracy is not compromised by mesh dependencies. Further details are presented in Section 4.5.

4.4 Simulation workflow

The foundation of every combustion simulation is a generalized framework into which various models like turbulence, species transport and combustion are introduced in a step-wise manner to achieve higher numerical stability and avoid divergence due to abrupt changes in the flow dynamics. The configuration of this framework relies on multiple parameter files in ThetaCOM, acting as intermediaries between the solver and the user for defining essential pre-processing and solver settings.

Initially, general inputs such as boundary conditions, reaction mechanisms, fuel and air mass flow rates, reference values, and the turbulence model are defined. Following this, the solver settings are established, encompassing relaxation factors, discretization methods, and pressure-velocity coupling strategies. Despite the availability of numerous equations for velocity and pressure determination, the interdependence of variables across all equations categorizes the system as coupled. To navigate this complexity, this study employs the Semi Implicit Method for Pressure-Linked Equations (SIMPLE) algorithm [128], an iterative technique characterized by pressure-velocity coupling. After solving the momentum equations, three additional steps, pressure correction, velocity correction, and mass flow correction, are performed [129].



Figure 4.3: ThetaCOM simulation workflow with three stages concerning the reactivity of the flow: cold flow, EDM and FRC, with each stage consisting of two phases, implemented by the use of six subsequent parameter files

The simulation initiates with a cold flow setup (with combustion models deactivated) and uses UDS for the initial 10,000 iterations. The next stage transitions to 2nd order Quadratic Upwind Differencing Scheme (QUDS) for a further 10,000 iterations, establishing a numerically stable foundation. Upon achieving stability, combustion models are activated in subsequent phases. The third and fourth phases incorporate the Eddy Dissipation Model (EDM), applying 1st order UDS for discretization with the Nicol DLR H₂ mechanism [130] over 5,000 iterations. Phase five introduces chemical reactions via the Finite Rate Chemistry (FRC) method, employing the detailed DC1S30N18 mechanism [131] and applying QUDS for all equations except species, which continue with UDS. The final phase fully implements QUDS across all equations, including species, with the analysis proceeding until NO_x emissions (in ppm) at the outlet stabilize.

4.5 Mesh dependence study

The mesh resolution can considerably influence the accuracy and reliability of CFD simulations. Inadequate mesh refinement can lead to erroneous results, while overly refined meshes can result in excessive consumption of computational time and resources. Therefore, determining the appropriate mesh resolution is crucial for obtaining reliable results. Mesh dependence study involves testing the sensitivity of the simulation results to different mesh resolutions to find the optimal mesh. Since the simulation run by computer codes has an inherent uncertainty, the estimation of uncertainty has to be conducted as verification to analyse the solution accuracy. As the grid becomes finer, it typically results in a more accurate solution. However, the computational effort rises when increasing the mesh size. If a mesh still can give a solution that meets the accuracy requirements after decreasing its size, employing this coarse mesh can save both time and computing resources, especially for the projects that require multiple operating conditions to be investigated.

4.5.1 Grid Convergence Index

The procedure for a mesh dependence study follows the steps recommend by I. B. Celik [132] which involves 5 different grids, that are identical in topology and have significantly different cell count. After the simulations of 5 grids, the values of key variables important to the objective of the simulation study are to be determined.

In order to describe the size of grids, a representative cell size h should be defined:

$$h = \left[\frac{1}{N} \sum_{i=1}^N (\Delta V_i) \right]^{1/3} \quad (4.1)$$

where ΔV_i is the volume of the i -th cell, and N represents the total number of cells. For three-dimensional grids, this relation holds as a cubic cell size and is derived from [132]. However, in this study, the meshing process uses tetrahedral cells, which necessitates the introduction of an additional cell size variable, a , representing the typical edge length of tetrahedral cells. The relationship between h and a is derived from the fact that a cube with edge length h has the same volume as a regular tetrahedron with edge length a . This geometric relationship is expressed as:

$$h = \left(\frac{\sqrt{2}}{12} \right)^{1/3} \times a \approx 0.49028 \times a \quad (4.2)$$

In this context, the variable a is more meaningful because the meshing process is controlled by setting a "Cell Size" in the meshing tool (ANSYS), which defines the representative edge length of the tetrahedral cells in the meshing region. It should be noted that the refinement factor between two grids $r = h_{\text{coarse}}/h_{\text{fine}}$ is recommended to be larger than 1.3, which ensures enough difference is set between the grids.

Table 4.2: The refinement factor and corresponding mesh resolutions with cell count. Where $h = 0.49028 \times a$

Refinement factor	h (mm)	a (mm)	Cell count (in million)
–	0.147	0.3	28.51
$r_{21} = 1.50$	0.221	0.45	12.95
$r_{32} = 1.56$	0.343	0.70	7.67
$r_{43} = 1.43$	0.490	1.00	5.10
$r_{54} = 1.30$	0.637	1.30	3.76

The indices 1 through 5 correspond to a hierarchical classification of mesh refinement, with 1 representing the finest mesh and 5 the coarsest. The creation of fine and coarse meshes can be conducted through a global adjustment of the cell numbers throughout the domain, or through a localized refinement strategy that targets specific regions. This study adopts the latter approach, applying refinement factors specifically to the reaction zone BOI (see Figure 4.2). Table 4.2 details the cell counts for each grid size used in the study, alongside the associated refinement factors. The variable ' a ' denotes the tetrahedral cell size within the flame zone, while ' h ' is the representative cell size determined using Equation 4.1. In subsequent figures that pertain to the grid study, the cell size ' a ' will serve as the metric for indicating the degree of mesh refinement.

Apparent Order p and quantities $q(p)$ and s are defined according to [132] as:

$$p = \frac{1}{\ln(r_{21})} \ln \left[\frac{\varepsilon_{32}/\varepsilon_{21} + q(p)}{r_{21} - s} \right] \quad (4.3)$$

$$q(p) = \ln \left[\frac{r_{21}^p - s}{r_{32}^p - s} \right] \quad (4.4)$$

$$s = 1 - \text{sgn}(\varepsilon_{32}/\varepsilon_{21}) \quad (4.5)$$

$\varepsilon_{32}, \varepsilon_{21}$ represent the difference of the solutions of the different meshes with respect to the flow quantity Φ and are derived from [132] as:

$$\varepsilon_{21} = \Phi_2 - \Phi_1 \quad (4.6)$$

$$\varepsilon_{32} = \Phi_3 - \Phi_2 \quad (4.7)$$

When looking at equation 4.3 it becomes evident that the Apparent Order p can only be determined by iteration. For the first iteration step, $q(p) = 0$ can be assumed. The final result for p is reached when, $q(p)$ and p do not change significantly between two iterations. In the next step, the so-called approximate relative errors must be determined for each refinement step. These are defined according to [132] as:

$$e_a^{21} = \left| \frac{\Phi_1 - \Phi_2}{\Phi_1} \right| \quad (4.8)$$

Ultimately, the Grid Convergence Index (GCI) is determined from the previously determined variables by:

$$GCI_{fine}^{21} = \frac{1.25 \cdot e_a^{21}}{r_{21}^p - 1} \quad (4.9)$$

If the GCI value of the index is less than 3%, the three meshes can be considered comparable. For more detailed insight into the meaning of the formulas and variables used, please refer to [132, 133].

In this study, averaged NO_x emissions and temperature at the outlet surface were chosen as key variables to assess the mesh dependence. These parameters are critical indicators for examining the combustion chamber's capabilities regarding FF and LF. The mesh sensitivity analysis spanned a broad operational spectrum, ensuring the plausibility of results under varying boundary conditions. Specifically for FF, the five meshes listed in Table 4.2 were evaluated across a hydrogen content range of 0%, 60%, 80%, and 100% at an equivalence ratio $\Phi = 0.74$, as well as $\Phi = 0.30$ to account for LF scenarios, refer to Table 4.1 for details about the test cases.

The results of GCI method reported in Tables 4.4 and 4.3 offer significant insights into the convergence behaviour of various mesh sizes, contributing to a profound understanding of the simulation's accuracy and consistency over a broad operational spectrum. The minimal values of relative error and GCI reinforce the mathematical precision of the results for the investigated parameters, suggesting the achievement of grid independence [132] within the framework of this study.

4.5. MESH DEPENDENCE STUDY

Table 4.3: Relative Error and Grid Convergence Index (GCI) for FF and LF. The variable under consideration is Temperature (in K) probed at the outlet surface

Mesh convergence parameters	0% H ₂	60% H ₂	80% H ₂	100% H ₂	100% H ₂
	$\Phi = 0.74$	$\Phi = 0.74$	$\Phi = 0.74$	$\Phi = 0.74$	$\Phi = 0.30$
0.30 mm	2110.3	2127.5	2168.3	2241.8	569.9
0.45 mm	2109.4	2129.6	2170.7	2247.6	569.1
0.70 mm	2087.1	2140.2	2172.8	2246.6	1404.9
1.00 mm	2090.5	2134.9	2172.5	2247.1	1403.2
1.30 mm	2083.7	2135.4	2173.2	2247.3	1410.5
e_{21}^a	0.04%	0.1%	0.11%	0.26%	0.14%
e_{32}^a	1.06%	0.5%	0.1%	0.04%	147%
e_{43}^a	0.16%	0.25%	0.015%	0.02%	0.13%
e_{54}^a	0.33%	0.025%	0.03%	0.01%	0.5%
GCI ₂₁	0.06%	0.4%	0.97%	0.07%	0.18%
GCI ₃₂	1.4%	0.75%	0.77%	0.001%	74%
GCI ₄₃	0.21%	0.41%	0.14%	0.007%	0.15%
GCI ₅₄	0.47%	0.05%	0.45%	0.005%	0.65%

Nonetheless, an anomaly is evident, as indicated by the data in Table 4.3 and Table 4.4. Specifically, when examining LF at an operating condition of 100% H₂, $\Phi = 0.30$, there is a marginal error between the fine (0.3 mm, 0.45 mm) and coarser meshes (0.70 mm, 1.00 mm, 1.30 mm). The coarser meshes unexpectedly yields plausible outcomes. This observation suggests caution against employing excessively fine meshes for cases with leaner mixtures, where $\Phi < 0.74$. A potential explanation for this behaviour could be attributed to the refined face sizing implemented at the outlet for the finer meshes. A smaller element size at the outlet, compared to the upstream elements, can create difficulties in achieving convergence, particularly in grids with highly inhomogeneous resolution. Very fine cells near the outlet may complicate the convergence of the solution by restricting the propagation of combustion information throughout the domain, especially in lean cases, which could potentially result in LBO (for theory refer to subsection 3.3.1).

Table 4.4: Relative Error and Grid Convergence Index (GCI) for 5 different mesh resolutions under FF and LF investigations. The variable under consideration is NO_x (in ppm) probed at the outlet surface (refer subsection A.3.1).

Mesh convergence parameters	0% H₂ $\Phi = 0.74$	60% H₂ $\Phi = 0.74$	80% H₂ $\Phi = 0.74$	100% H₂ $\Phi = 0.74$	100% H₂ $\Phi = 0.30$
0.30 mm	8.9	8.8	11.1	24	0.01
0.45 mm	8.8	9.7	11.6	25.4	0.0101
0.70 mm	8.6	10.2	12.0	26.3	0.58
1.00 mm	9.1	9.6	12.2	26.4	0.61
1.30 mm	9.4	10.5	12.6	27.2	0.68
e_{21}^a	1.12%	10.22%	4.5%	5.83%	0.99%
e_{32}^a	2.23%	5.15%	3.45%	3.54%	56.5%
e_{43}^a	5.81%	5.88%	1.67%	0.38%	5.17%
e_{54}^a	3.3%	9.38%	3.28%	3.03%	11.48%
GCI_{21}	2.83%	12.14%	14.5%	21.55%	1.24%
GCI_{32}	5.49%	28.45%	6.77%	15.03%	123%
GCI_{43}	15.01%	11.84%	11.5%	9.42%	6.15%
GCI_{54}	11.04%	0.05%	23.15%	25.55%	12.92%

Table 4.4 shows elevated GCI values and relative errors for the NO_x emission's parameter, as determined using the Tecplot [134] macro described in Appendix Subsection A.3.1. This study adopts a larger margin of error for NO_x emissions compared to other variables, due to their expression in parts per million (ppm), which corresponds to $1e - 6$ time the value derived from the RANS solution. This representation in ppm also facilitates direct comparisons with experimental measurement results.

Given the anomalies observed in the LF scenario with 100% H_2 and $\Phi = 0.30$, making a definitive decision regarding the best mesh is challenging. The fine meshes fail to accurately capture physical phenomena, suggesting they should be excluded from LF studies. Alternatively, adjusting the face-sizing refinement at the outlet to match the upstream element consistency could be explored to address this issue.

4.5.2 Graphical illustration and flow visualization

While residual monitoring offers a measure of convergence, it cannot necessarily confirm the physical accuracy of the flow results or the achievement of a steady state [40]. In scenarios where simulation residuals display oscillatory convergence, stability of the key CFD variables should be assessed at specific probes to ensure reliable outcomes. It is crucial, therefore, to monitor the convergence trends of variables throughout the simulation. Keeping in mind, the aim of this study, the convergence behaviour of NO_x emissions under the operating conditions detailed in Tables 4.3 and 4.4 has been graphically illustrated across a range of mesh configurations in Figure 4.4.

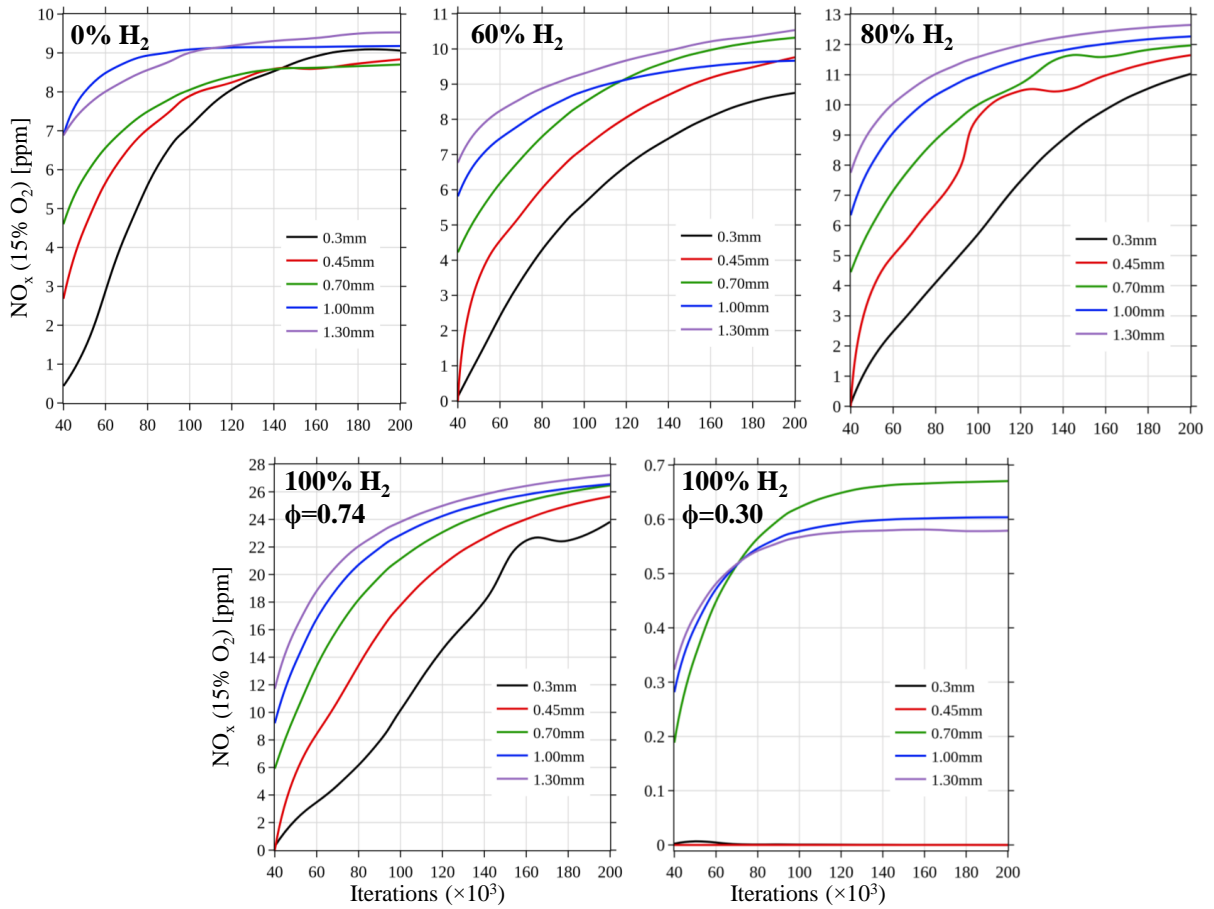


Figure 4.4: Convergence behaviour of NO_x emission at the outlet for a range of meshes and operating conditions. Y-axis is the NO_x values and X axis represents the iterations.

The observed convergence behaviour is key for identifying the optimal mesh refinement that ensures faster convergence with minimal resource utilization for both LF and FF investigations. According to Figure 4.4, achieving reliable NO_x emission results and stability requires at least 100,000 iterations for all the operating conditions. This necessity arises from the requirement to report NO_x emissions in parts per million (ppm), highlighting the precision level attainable through RANS simulations, which is equivalent to maintaining accuracy in CFD variables such as velocity, temperature, and mass flow rate up to 6-7 decimal places. Figure 4.4 also illustrates that, for the FF case with 0% H_2 , meshes with cell sizes of 1.00 mm and 1.30 mm achieve convergence with fewer iterations compared to finer meshes. Across all FF cases, the performance of each mesh was found to be remarkably consistent, yielding results within an acceptable range of relative error.

A notable finding, corroborated by the GCI method, emerged in the LF scenario with 100% H_2 at $\Phi = 0.30$: finer meshes were ineffective in resolving NO_x emissions due to the occurrence of LBO phenomena. Consequently, the 0.70 mm, 1.00 mm, and 1.30 mm meshes exhibited both consistent and dependable performance in the prediction of NO_x emissions for both FF and LF cases, meriting their selection for future simulations. However, the final selection also hinges on the mesh's ability to precisely predict and validate the experimentally measured flame lift-off height, a critical parameter for this thesis.

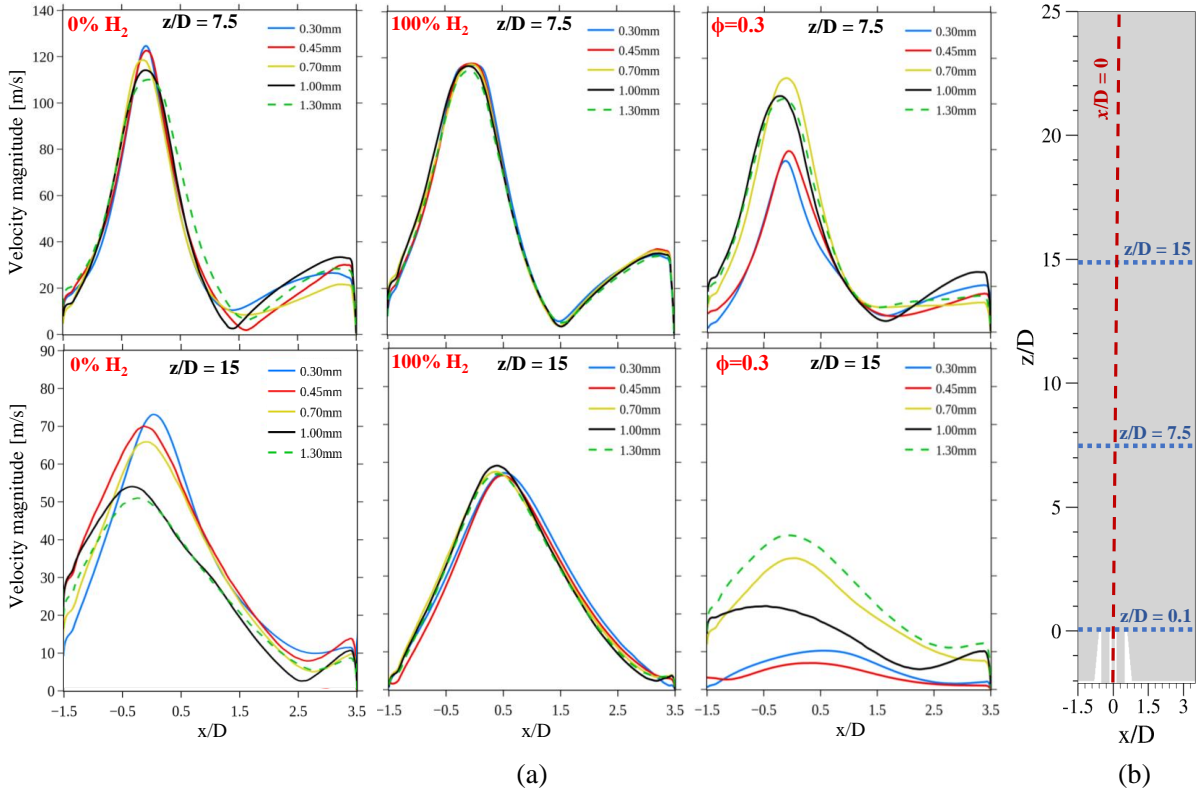


Figure 4.5: Velocity magnitude comparison at 1D probes along combustor width for FF and LF investigations across different mesh resolutions. The figure (b) alongside illustrates the 1D probes selected for extracting and monitoring CFD data.

To enhance the comparative analyses of different meshes, this thesis also adopts a traditional approach, evaluating key variables of interest such as velocity magnitude, temperature, and the mass fraction of the hydroxyl radical along 1D probes/lines. This method offers a more comprehensive basis for selection of appropriate mesh size. Figure 4.5 showcases the comparison of velocity magnitude along 1D line probes along the combustor width for both FF and LF investigations. Generally, the results across meshes are consistent, indicating mesh-independent outcomes. Yet, a notable deviation is observed in the lean condition at $\Phi = 0.30$, highlighting the importance of this visualization method. These findings further reinforce the selection of a mesh resolution between 0.45 mm and 0.70 mm, as it also aligns closely with the velocity profiles of finer meshes, particularly at a downstream location of $z/D = 15$, in the FF case of 0% H_2 .

The figure 4.6 illustrates the temperature profiles along the combustor length ($x/D = 0$) for both FF and LF scenarios using different mesh resolutions. This comparison aids in identifying flame positions through noticeable temperature peaks at specific z/D values.

4.5. MESH DEPENDENCE STUDY

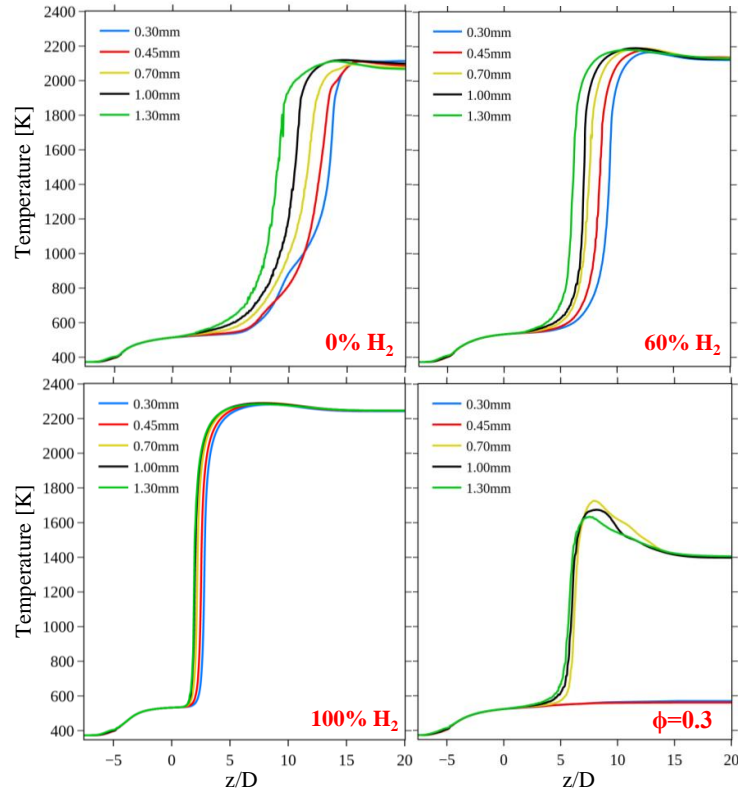


Figure 4.6: Temperature distribution along the combustor length for FF and LF investigations at different mesh resolutions.

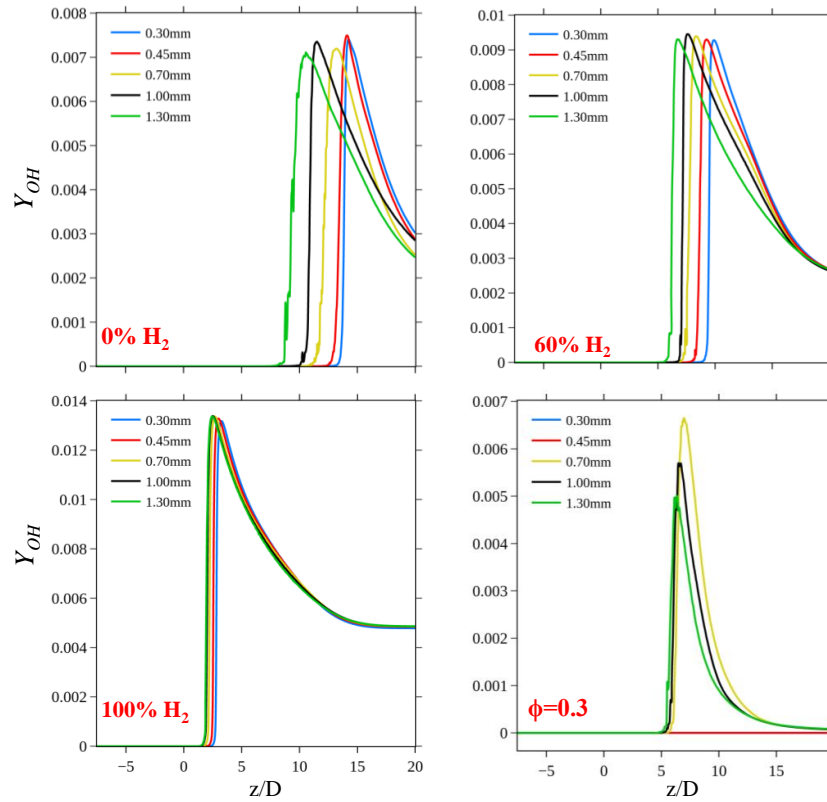


Figure 4.7: Mass fraction of OH along the combustor length for FF and LF investigations, showcasing mesh convergence.

Concurrently, figure 4.7 exhibits the distribution of OH mass fraction, where higher values serve as indicators of the flame location. This aligns with the temperature trends, providing a unified approach for identifying flame zones. Both figures demonstrate that, at 100% H₂ and $\Phi = 0.74$, all examined meshes consistently predict the z/D location of peak Temperature and Y_{OH} . However, at lower H₂ vol.%, discrepancies arise between the coarse and fine meshes. The anomaly observed in LF case persists in figures 4.6 and 4.7, highlighting the impact of mesh selection on the fidelity of simulations.

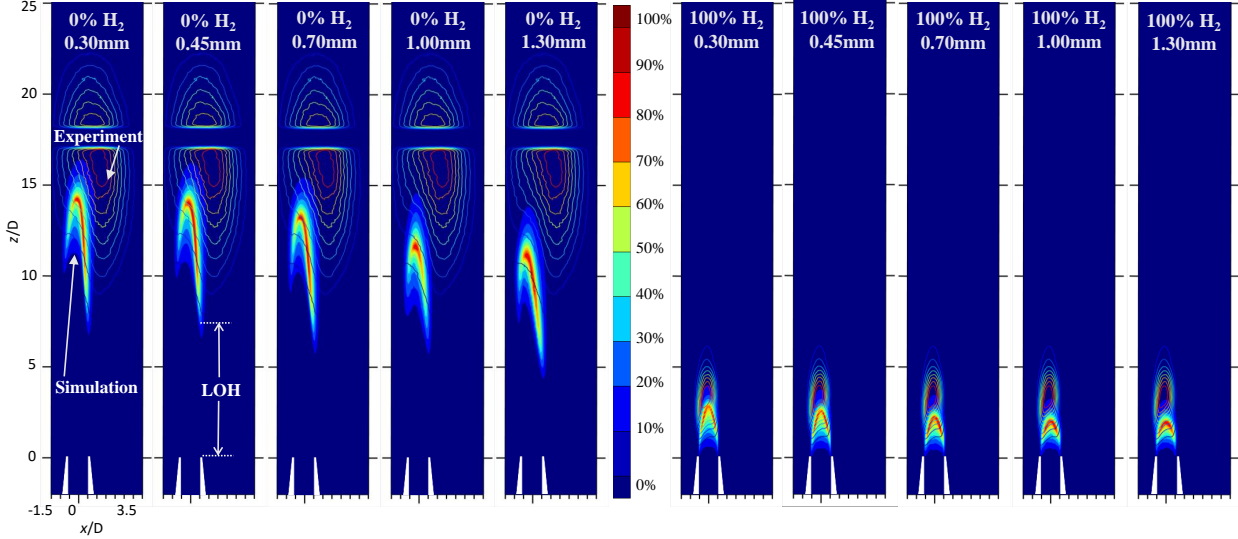


Figure 4.8: OH*-CL visualisation for TP configuration (0 and 100 vol.% H₂) across different mesh resolutions. LOH of the experimental results are compared with simulations.

To thoroughly assess flow dynamics and LOH, it is essential to examine contour plots for a visually detailed representation of the results, thereby enabling validation against experimental data [20]. Generally, OH*-chemiluminescence imaging is utilized in experimental setups to ascertain the flame position and morphology [135]. Due to the observational perspective relative to the nozzle configuration in OH*-CL imaging, two superimposed flame images are typically captured. Thus, the OH* radicals within a designated volume are collectively analysed, as illustrated in Figure 4.8. To process these images accurately, it necessitates computing the designated measurement area. This computation involves generating an auxiliary zone, mirroring the measurement volume's shape and location, using the post-processing tool Tecplot 360 [134], and interpolating the simulation data onto it (see Appendix A.3.2 for more details). A line of sight (LOS) integration across individual slices of the auxiliary zone, parallel to the camera's viewing direction, then yields the visualization of OH*-CL over the entire measurement volume, allowing direct comparison with experimental findings. Figure 4.8 shows the integrated OH*-CL for the reference case. The coordinate system of the diagram is adapted to the combustion chamber's coordinate system. The flame LOH was determined by measuring the difference between the base of the flame (a threshold value of 20% of the maximum value of Y_{OH} was used for all cases) and the exit of the air inlet nozzle.

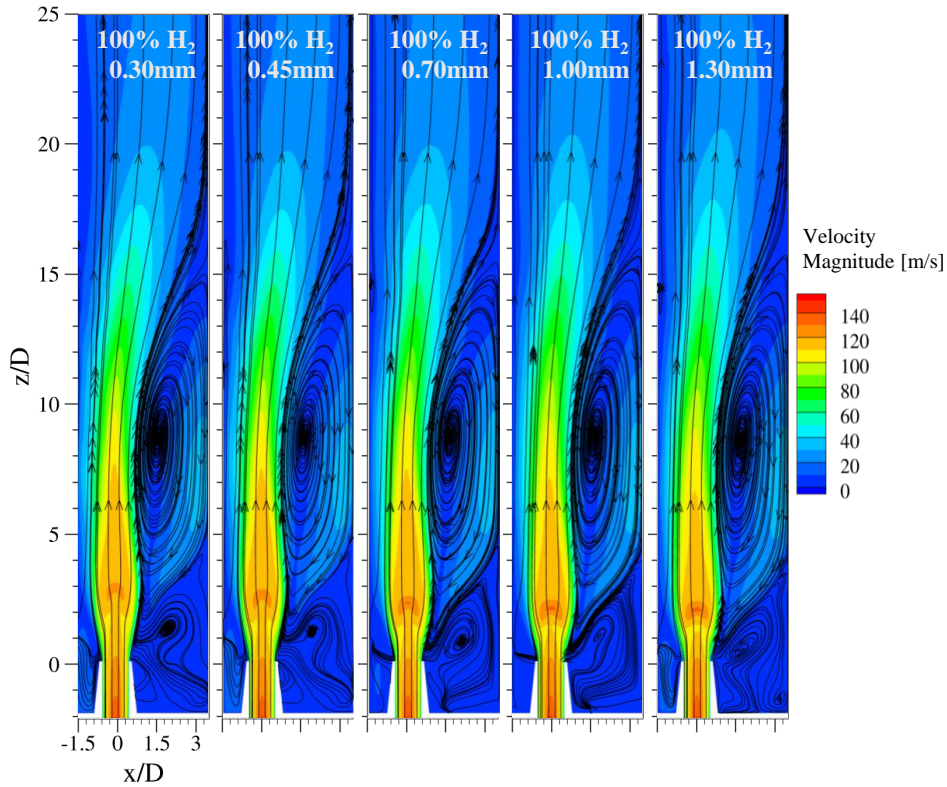


Figure 4.9: Flow field characteristics in TP configuration, showcasing different mesh resolutions for 100 vol.% H_2 and $\Phi = 0.74$.

Visualisation of OH^* -CL and flow velocities highlights the distinctive lifted and asymmetric nature of the flame within the combustion chamber for the 0 vol.% H_2 case, demonstrating stable combustion. As shown in Figure 4.8, for the 100 vol.% H_2 scenario, the LOH is consistent across various mesh refinements due to the flame attachment to the nozzle. However, for the 0% H_2 case, the LOH and flame morphology vary marginally with mesh resolution. Notably, the 0.30 mm mesh aligns more closely with experimental observations [20] and a reduced LOH trend is observed with coarser counterparts. This suggests that a 0.45 mm mesh represents an optimal balance between computational efficiency and accuracy.

The measured flow field and streamlines depicted in Figure 4.9, classify the flow into three zones: a high momentum jet exceeding $z/D = 16$, a pronounced lateral recirculation zone (LRZ) facilitating the mixing of hot exhaust with fresh gas, and a smaller recirculation zone (SRZ) adjacent to the nozzle. Each mesh accurately models these zones, with minor discrepancies observed in the re-attachment location and flow dynamics within the SRZ.

In summary, the mesh convergence study reveals that all meshes yield closely aligned solutions, corroborated by the low GCI values in Table 4.3. This investigation identifies a 0.45 mm mesh as suitable FF and a 0.70 mm mesh for LF investigations, accepting the necessary trade-offs between computational demand and the resolution of physical phenomena to generate practically insightful results within these constraints.

Chapter 5

Results and Discussion

This chapter delves into the outcomes of RANS simulations and engages in a detailed comparative analysis across the NP, FP, and TP configurations of the single nozzle FLOX[®] burner. Central to study is the examination of how fuel and load flexibility influence critical parameters such as flame lift-off height, flame shape, NO_x emissions, flow field, and temperature. It commences with a qualitative and quantitative evaluation of OH*-CL visualization, seeking to validate computational findings with experimental data [20]. Subsequently, flow re-circulation zones and velocity fields to understand the distinct flow dynamics inherent to each burner configuration. Next, the implications of FF, LF and the mixedness level on NO_x emissions are thoroughly examined, with a particular focus on their relationship to the adiabatic flame temperature. The last section is dedicated to analysing how outlet temperatures are affected by varying equivalence ratios.

5.1 Flame Shape and Lift-off Height

The investigation into FF and LF within an atmospheric single nozzle jet-stabilized FLOX[®] combustor reveals significant insights into the behaviour of hydrogen/methane-air mixtures under varied conditions. Central to these insights are the flame shape and lift-off height (LOH), whose variations underscore the combustor's adaptability and the intricate interplay between fuel composition, mixedness, and combustion dynamics. The subsection is divided into two analyses: qualitative and quantitative. The qualitative analysis utilizes contour plots of OH*-CL, which are generated with the LOS integration method detailed in Appendix A.3.2. The quantitative analysis, on the other hand, employs graphical data from line and point probes to precisely measure the LOH, thus quantifying the visual observations of the flame.

5.1.1 Qualitative evaluation

The analysis of contour plots offers a detailed perspective on flame dynamics, in response to changes in the combustor environment. Interpreting the average OH*-CL distributions uncovers how equivalence ratios and H₂ volume fractions influence flame characteristics.

The FF investigation in figure 5.1 showcases the flame's shape transition as the H₂ volume

percentage is varied in a non-premixed, jet-stabilized combustion setting, highlighting the flame's distinctively lifted and asymmetric nature towards 0% H₂ (corresponding to 100% CH₄, see also Table 4.1). As the H₂ content decreases, there is a noticeable elongation and distribution of the flame, moving away from the nozzle rim and expanding downstream. At 100% H₂, the flame is compact, with a higher concentration of reaction zones near the nozzle exit, suggesting a flame that is more anchored to the nozzle. This is typical of H₂ flames, which are characterized by higher reactivity and shorter ignition delays [136]. As the percentage of H₂ decreases, the LOH increases and its structure spreads further downstream, signifying a shift in the combustion dynamics. The flame stabilizes further into the flow, and the reduction in reactivity due to the lower H₂ content becomes apparent. The flame at 0% H₂ is widely spread out, suggesting that the flame stabilization mechanism has transitioned from being dominantly influenced by the hydrogen's reactivity to being more dependent on the jet flow dynamics and possibly the methane-air mixture combustion characteristics.

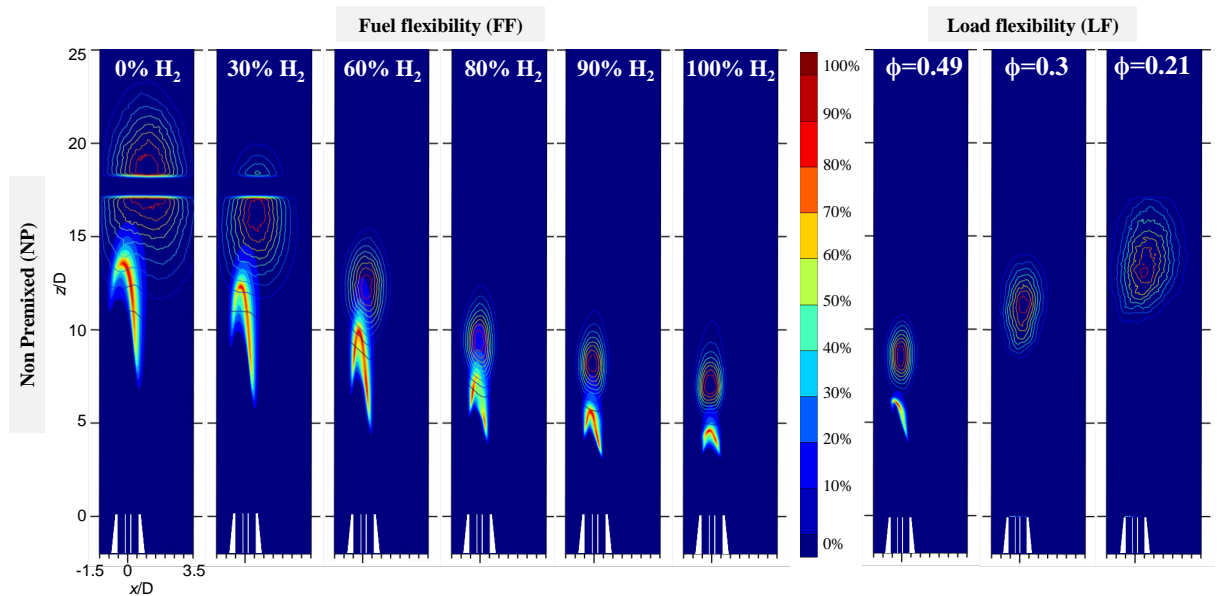


Figure 5.1: OH*-CL comparison of simulation and experiment dataset showcasing NP configuration. Left: FF, variation in H₂ vol.%. Right: LF, variation in $\Phi = 0.49\text{--}0.21$.

The concept of LF in combustion refers to the capacity of a combustor to perform efficiently in partial load operation, particularly at different thermal loads, which are typically adjusted by changing the equivalence ratio Φ . In the context of hydrogen-methane flames, as Φ decreases, representing a leaner mixture with less fuel relative to the oxidizer, the flame behaviour undergoes notable changes. When $\Phi = 0.74$, there is sufficient fuel to support a robust flame close to the nozzle, with a shorter LOH. As Φ decreases, the flame starts to lift off further away from the nozzle exit. This is because the flame requires a higher temperature to sustain the combustion reactions, and it must find this temperature in regions with recirculated hot gases further away from the nozzle, where the fresh mixture is cooler. At significantly lower equivalence ratios, approaching the LBO limit, the flame becomes increasingly unstable. Anchoring mechanism, thermal feedback from hot products and the flame's ability to auto-ignite the incoming fresh mixture become less effective, due to the reduced heat release in leaner mixtures. As a result, the flame can no longer sustain continuous combustion and eventually extinguishes if the mixture becomes too lean. This is marked by an increase in the LOH, a decrease in temperature and reactive

species concentration like OH^* , and eventually, the flame might detach entirely from the flow field or flicker out as evident in figure 5.1.

In the context of validating simulation results, a difference is observed when comparing the OH^* -CL signals from experiments to CFD simulation outcomes, as depicted in figure 5.1. The experimental OH^* -CL signal exhibits a broader spatial distribution, suggesting a wider flame presence, while the simulated flame appears more constrained and slender. This discrepancy highlights a potential limitation of the RANS approach in capturing the flame spread, particularly under lean combustion conditions. Despite this, the LOH predictions from the simulations are within a tolerable range of error, congruent with the experimental LOH trend discussed in subsection 5.1.2.

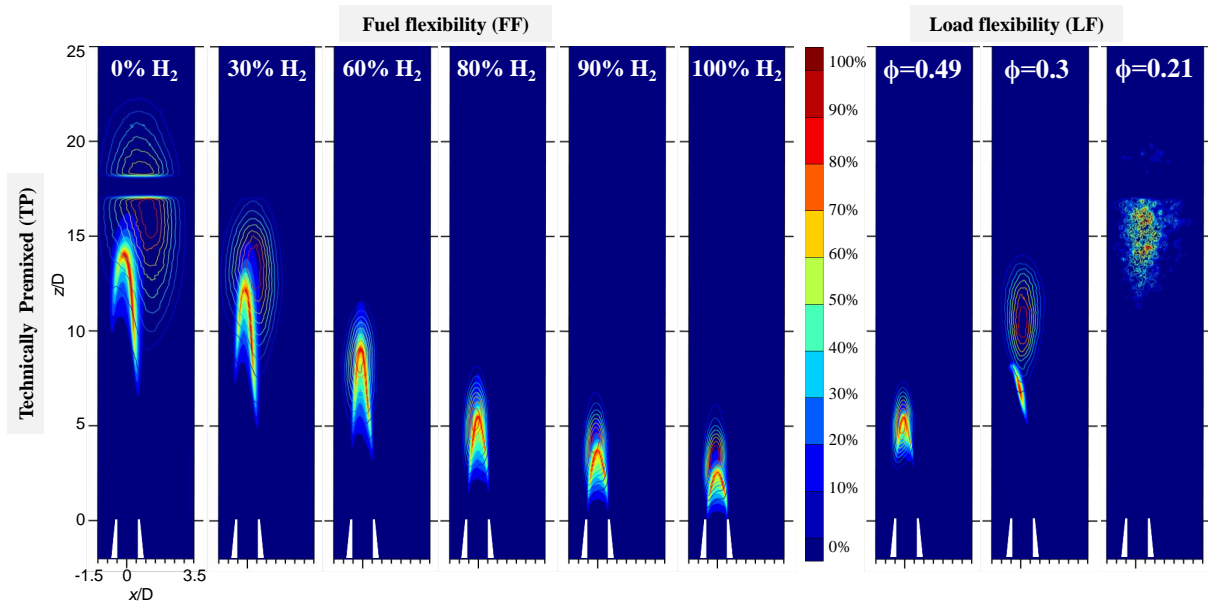


Figure 5.2: OH^* -CL comparison of simulation and experiment dataset showcasing for TP configuration. Left: FF, variation in H_2 vol.%. Right: LF, variation in $\Phi = 0.49\text{--}0.21$.

Similarly, the TP configuration has been illustrated in figure 5.2. For the FF sequence, we observe a pronounced transformation in flame shape as the H_2 content in the fuel blend increases. At 0% H_2 , the flame exhibits an extensive LOH and a broader shape, indicative of a diffused flame stabilized by the velocity shear layer and inner recirculation zone. This is consistent with methane-air combustion, where the flame speed is relatively lower, leading to a more distributed flame. With the progressive addition of H_2 , a notable change in the flame's structure occurs. The higher reactivity of hydrogen narrows the flame and reduces the LOH, indicating a shift from a stabilization mechanism driven by flow dynamics to one that is influenced by the chemical reactivity of the hydrogen. At higher H_2 concentrations, the flame becomes more compact, indicating higher influence of the hydrogen's rapid reaction kinetics and its ability to anchor the flame closer to the burner nozzle.

The LF sequence illustrates that, as Φ diminishes from 0.49 to 0.21, we witness a consistent increase in the LOH, an outcome of the reduced thermal power and lower temperatures unable to sustain combustion closer to the nozzle exit. At the lowest equivalence ratio presented ($\Phi = 0.21$), the flame becomes highly dispersed (as observed in the experiments [20]) and the OH^* -CL signal markedly sparse, a precursor to LBO conditions where the flame's stabilization mechanisms are insufficient to sustain the reaction, leading to

extinguishment. The simulation results demonstrate a commendable correlation with experimental observations. The overlap between the simulated OH^* -CL contour and the experimentally measured signal across a range of FF cases indicates a successful validation of the computational model.

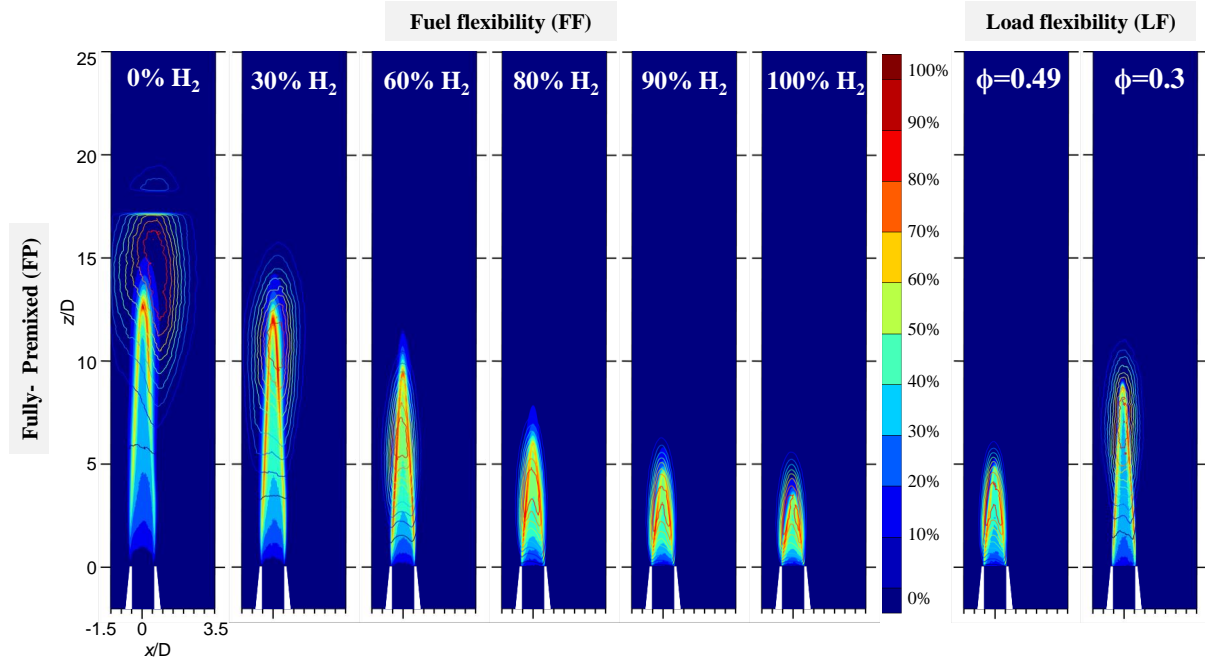


Figure 5.3: OH^* -CL comparison of simulation and experiment dataset showcasing for FP configuration. Left: FF, variation in H_2 vol.%. Right: LF, variation in $\Phi = 0.49\text{--}0.30$.

Flame stretch refers to the rate at which the surface area of the flame changes due to the flow field [111]. In premixed combustion, stretch affects both the flame propagation speed and the flame structure. In conditions of high hydrogen content (60% to 100% H_2), the inherent high laminar burning velocity of hydrogen-rich flames coupled with low stretch rates (due to the compact and symmetrical flame shape observed) suggests that the flame experiences minimal aerodynamic strain. The efficient mixing of fuel and oxidizer in FP promotes uniform combustion and helps maintain a stable flame front, even as the flow field changes, which aligns with the observed attached flame behaviour in the figure 5.3.

As H_2 content decreases, the flame stretch likely increases due to the lower burning velocity of methane-air mixtures compared to hydrogen-air mixtures. This increased stretch can lead to a higher LOH and a broader flame structure, as the flame front tries to stabilize itself against the flow dynamics that are trying to disrupt it. However, in the FP configuration, the flame retains a more symmetrical shape compared to NP, suggesting that the premixing effectively counters the destabilizing effects of increased stretch at lower H_2 percentages.

Across all configurations, the trend is clear: higher H_2 concentrations lead to a compact and anchored flame, while lower concentrations result in a diffused and elongated flame that is sensitive to aerodynamic effects. This indicates that the chemical reactivity of H_2 plays a significant role in flame stabilization.

In conclusion, the comparative analysis emphasizes the importance of the combustion configuration NP, FP, TP in determining the flame behaviour in response to FF and LF. It reveals that while TP offers an intermediate stance between NP and FP, the choice of configuration profoundly impacts the flame's stability, shape, and LOH under

varying operational conditions, necessitating careful consideration in the design and operation of combustion chambers, especially those intended to accommodate a wide range of fuel compositions and operating loads. The qualitative evaluation reveals that the RANS simulations are sufficiently robust for practical estimations of flame behaviour, but caution must be exercised when interpreting results, especially at LBO limit where the physical accuracy may be compromised due to the inherent simplifications of the RANS methodology.

5.1.2 Quantitative Evaluation

Delving into the quantitative aspects of LOH, unveils a consistent trend across the examined burner configurations. The inverse relationship between vol. %H₂ and LOH is evident, wherein an increased H₂ content correlates with a decreased LOH.

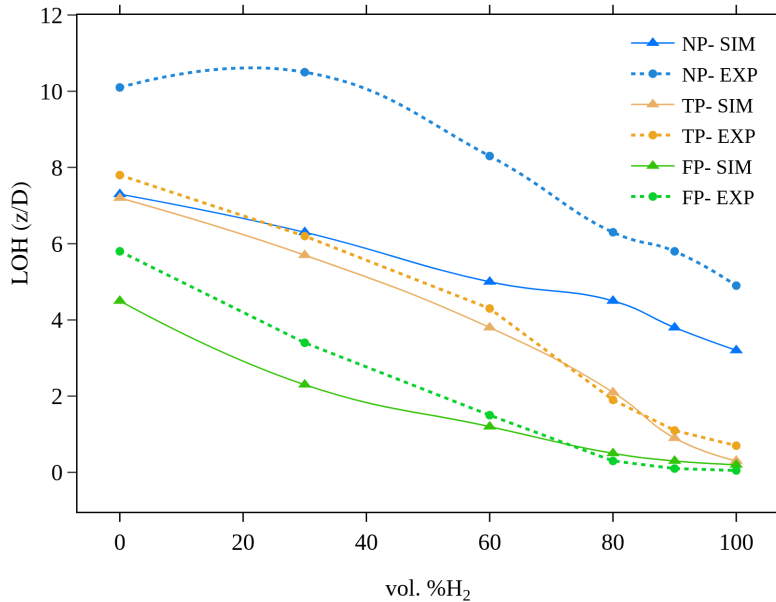


Figure 5.4: Quantitative representation of flame LOH for FF investigations.

The figure 5.4 under consideration contrasts the simulation (SIM) results with experimental (EXP) data [20] for each configuration, offering a multifaceted perspective on LOH. In NP configurations, the SIM results depict a distinct decrement in LOH with the increment in hydrogen content, mirroring the EXP observations. The largest deviations from experimental data are observed in the NP configuration.

The TP configuration demonstrates a steady decline in LOH across both SIM and EXP. The trends here indicate that technically pre-mixing the fuel and oxidizer does not completely homogenize the mixture, yet still significantly influences the LOH. This effect can be attributed to the intermediate stage between mixing and combustion, allowing hydrogen's properties to influence the flame stability sooner than in the NP scenario. The SIM curve's adherence to the EXP trend reinforces the validity of the computational model in capturing the flame dynamics under technically premixed conditions. For the FP scenario, the SIM and EXP trends are analogous and steeper compared to NP and TP configurations, showcasing the lowest LOH values. This steep decline corresponds to the theoretical understanding that a uniform mixture of fuel and air leads to an immediate

response of the flame to changes in fuel composition. In the presence of high vol. %H₂, the homogeneous mixture and high laminar flame speed significantly reduce the LOH, indicating an anchored and stable flame front. The smallest LOH values observed in the FP configuration for both SIM and EXP suggest that full premixing is most effective in reducing the distance between the flame and the nozzle.

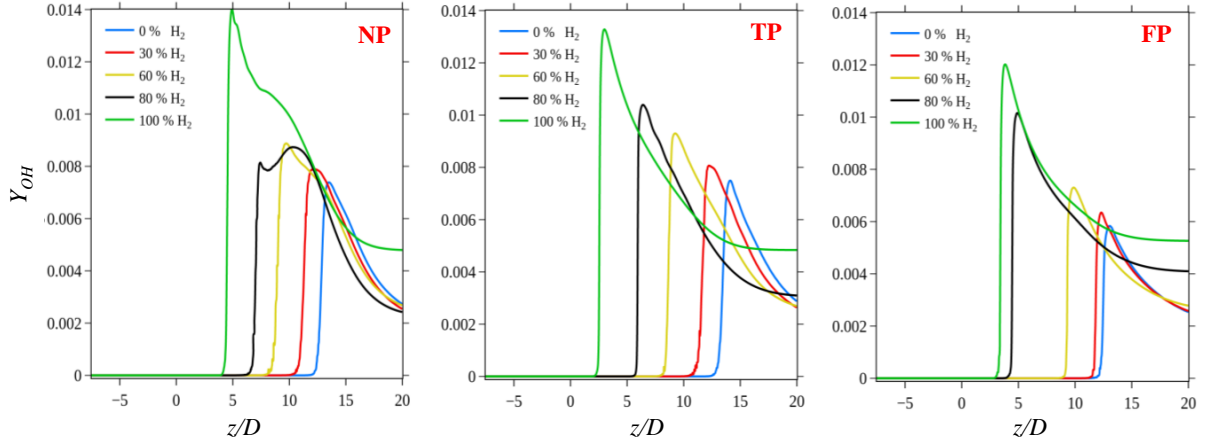


Figure 5.5: Mass fraction of OH along the combustor length for FF investigations, showing the trend in different configurations.

The examination of OH mass fraction profiles, presented in Figure 5.5, extends our understanding of the stabilization mechanisms within various burner configurations. The concentration of OH, indicative of high-temperature reaction zones, is integral to identifying the flame front. Within the NP configuration, the Y_{OH} profiles signify a shift from a broad to a more concentrated flame structure with increasing hydrogen content, correlating with the decrease in LOH. The sharpening and proximity of peak Y_{OH} concentrations to the nozzle at high H₂ substantiate a confined combustion zone and a diminished LOH, reflecting hydrogen's reactive dominance. The TP and FP configurations, through their Y_{OH} profiles, consistently demonstrate the effective utilization of hydrogen properties due to pre-mixing, resulting in prompt and robust flame stabilization. The FP configuration, in particular, maintains high Y_{OH} levels near the nozzle across all fuel flexibilities, denoting a stable flame front and minimal LOH. This congruence in Y_{OH} profiles with experimental data across configurations strengthens the confidence in simulation models to accurately replicate real combustion dynamics. It also establishes Y_{OH} as a pivotal marker for validating quantitative LOH in simulations.

In the case of LF, a quantitative analysis of the LOH during LBO limit, is challenging to illustrate due to the dynamic instability of the flame. The flame experiences rapid oscillations within the flow channel, leading to intermittent partial blowouts and subsequent relight events across the combustor segments. Such complex transient behaviours are beyond the scope of steady-state RANS simulations, which inherently cannot capture these rapid, time-dependent phenomena. As a result, the RANS approach does not accurately represent the flame's response to extreme lean conditions, as has been observed and documented in the experimental investigations referenced [20].

From a design standpoint, these findings emphasize the importance of optimizing combustors for different fuel compositions. The trend towards lower LOH with higher vol. %H₂ aligns with the goal of maintaining high temperatures away from the wall surface materials, vital for short and compact combustor design with minimal pollutant formation. The

detailed LOH values from comparison provides benchmarks for CFD model validation and are valuable in advancing combustor designs that can adapt to a range of fuel compositions and operating conditions.

5.2 Quantitative analysis of NO_x emissions

The integration of hydrogen as a primary fuel component represents a pivotal shift towards environmentally conscientious combustion practices. This transition, however, introduces new complexities in the emission profiles of nitrogen oxides (NO_x), pollutants that are the focus of stringent emission standards due to their adverse environmental and health effects. The provided graphical data on NO_x emissions delineates the dependency on both the volumetric percentage of hydrogen in the fuel mix and the equivalence ratio.

5.2.1 Variations in NO_x emissions relative to hydrogen volume fraction

The experimental analysis of exhaust gases offers a technical benchmark for evaluating the performance of varied nozzle configurations, primarily through NO_x measurements normalized to a uniform O_2 concentration on a dry basis. This normalization procedure (detailed in subsection 3.2.3), accounts for varying oxygen levels and presents the NO_x values corrected to a standard reference of 15 vol.% O_2 , enabling a consistent comparison across different operating conditions.

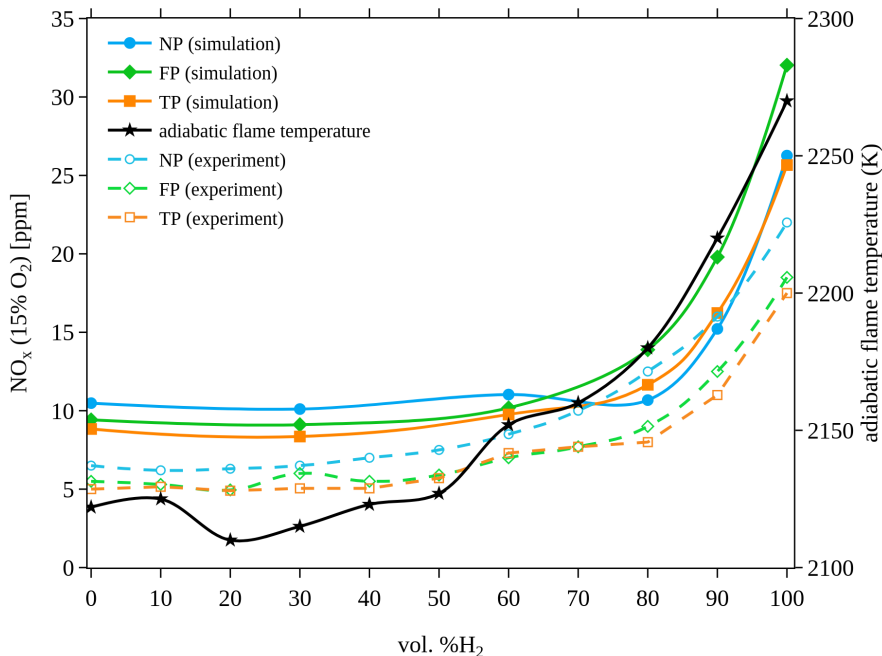


Figure 5.6: NO_x emissions in parts per million (ppm) as a function of hydrogen volume percentage for NP, FP, and TP configurations. The solid lines represent simulation data and dashed lines are the experimental data.

Analysing NO_x emissions in relation to the vol. % H_2 (illustrated in figure 5.6) reveals a nuanced interplay between fuel composition at a fixed global equivalence ratio of 0.74 and

emission levels. The corrected NO_x values on the left y-axis resonate with anticipated trends corresponding to each case under study, suggesting a direct correlation with mixedness level. In NP cases, NO_x levels are higher compared to TP and FP configurations. This can be attributed to localized areas of high temperature due to suboptimal fuel-air mixing, leading to increased thermal NO_x formation. Turning our attention to the adiabatic flame temperature, represented on the right y-axis and computed via the GRI 3.0 mechanism in Cantera 2.5, we discern a proportional relationship between temperature, vol. % H_2 and NO_x formation. Thermal NO_x generation [8], a temperature-dependent process, intensifies with rising adiabatic flame temperatures, due to hydrogen's low ignition energy and high diffusivity, which supports faster reaction rates.

The experimental data highlights the influence of homogenous mixing in curtailing NO_x emissions by preventing extreme thermal gradients within the combustion chamber. In the simulation dataset, a distinct trend concerning the mixedness level does not manifest as clearly as in experimental observations. Particularly at elevated vol. % H_2 , the FP configuration, exhibits the highest NO_x values. This deviation emphasizes the limitations inherent in RANS simulations while reporting NO_x emissions at the parts per million (ppm) level, reflecting the restrictions in capturing the precision required for accurate emissions' quantification.

5.2.2 Variations in NO_x emissions relative to Equivalence Ratio

The relationship between NO_x emissions and equivalence ratio demonstrates the influence of fuel richness on emissions. Lower equivalence ratios, indicating leaner fuel mixtures, generally result in diminished flame temperatures, thereby curtailing thermal NO_x production.

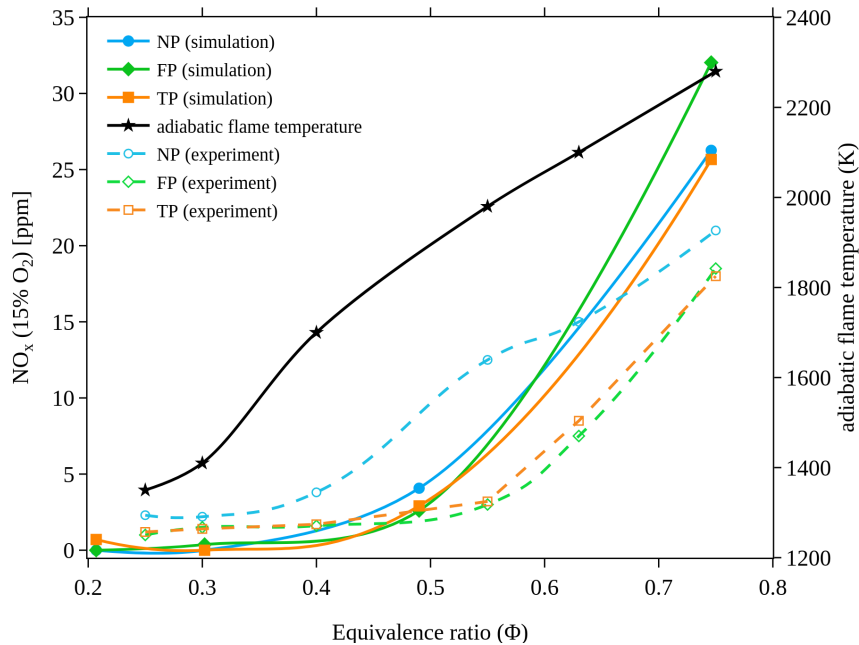


Figure 5.7: NO_x emissions in parts per million (ppm) as a function of equivalence ratio (Φ) for NP, FP, and TP configurations. The solid lines represent simulation data and dashed lines are the experimental data.

From figure 5.7 it is observed that as Φ increases, there is an exponential rise in NO_x emissions for all configurations. For hydrogen-enriched mixtures, the rapid kinetics due to hydrogen's high diffusivity and low activation energy for combustion reactions result in a steeper temperature gradient, escalating the rates of NO_x production. Consequently, the observed trend corroborates the fundamental understanding that NO_x emissions intensify with the increase in flame temperature.

The experimental data points for the NP configuration illustrate the most significant NO_x emissions across the range of Φ , likely reflecting local hot spots and heterogeneities in the fuel-air mixture, which lead to higher peak flame temperatures and consequently, increased NO_x formation. In comparison, the TP and FP configurations demonstrate a more moderate increase in NO_x emissions with rising Φ , suggesting a uniform fuel-air mix and controlled combustion process. Notably, the simulation results for the FP configuration diverge from the experimental data, particularly at $\Phi = 0.74$ where simulation predicts the highest emission levels. At lower equivalence Φ , nearing the LBO limit, all configurations exhibit flame instability and a noticeable deviation in emission trends. This variation highlights possible shortcomings in the RANS simulation's ability to accurately model the chemical kinetics of emission formation in highly reactive H_2 -enriched environments. Additionally, the simulation's prediction of higher emission levels can be partly attributed to the assumption of adiabatic combustor walls, which artificially maintain higher temperatures within the combustion chamber than what might be observed under actual operating conditions.

5.2.3 Relation between NO_x and CO emissions

The trends depicted in figure 5.8 are reflective of the complex interplay between combustion dynamics and chemical kinetics, as influenced by the level of hydrogen in the fuel mixture.

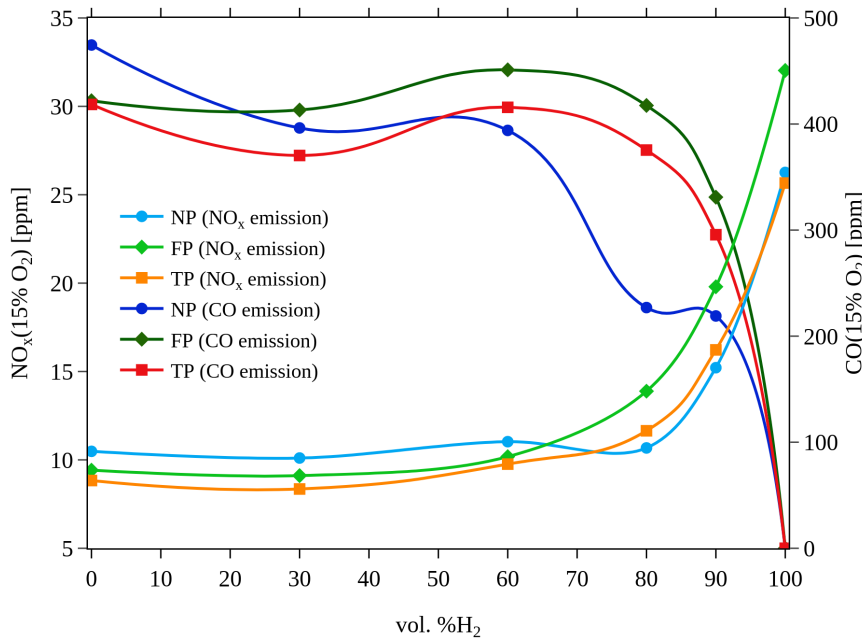


Figure 5.8: NO_x and CO emissions versus vol. %H₂ for NP, TP, and FP configurations.

For NO_x emissions, there is a gradual increase, followed by a steep rise from 80 vol.% H₂ onwards. This increase is attributable to higher flame temperatures associated with H₂ combustion. Conversely, CO emissions display an oscillatory trend. Methane, the sole fuel component at 0% H₂, has a higher propensity to produce CO, especially under less lean conditions or where combustion is quenched due to lower flame temperatures and insufficient oxygen availability. As the percentage of hydrogen, with its low activation energy and high flame speed, increases in the mixture, it enhances the overall reactivity of the fuel. This leads to a more complete combustion even at leaner conditions, thereby diminishing CO formation.

Upon reaching 100% hydrogen as fuel, the absence of carbon atoms in the fuel molecule negates the formation of CO. The combustion products are primarily water vapour and trace amounts of nitrogen oxides, contingent upon the temperature and pressure conditions. Thus, the CO emission profiles across different fuel compositions are dependent on the underlying combustion chemistry and thermodynamic properties prevalent in hydrogen-enriched methane flames. The figure 5.8 also showcases the challenge in optimizing fuel composition for reduced emissions. While increasing H₂ enhances flame speed and reduces CO, it also raises flame temperature, potentially increasing NO_x. Understanding these dynamics is crucial for designing combustion systems that leverage the benefits of hydrogen while mitigating emission-related drawbacks.

Notably, the simulation results are not only within the same order of magnitude as the experimental measurements, but they also exhibit a parallel trend across the entire spectrum of hydrogen volume fractions. This congruence is significant, given that emissions are reported in parts per million (ppm), a unit that demands a high level of precision in quantitative analysis. The fact that the simulated emissions mirror those observed experimentally, in both trend and scale, lends substantial credibility to the computational model employed.

5.3 Flow recirculation and velocity profiles

A direct comparison of the simulation results with experimental data is constrained at low hydrogen content; the experimental setup's field of view does not capture the flame's influence on the flow field [20]. Furthermore, in the FP configuration, the seeding challenges for accurate Particle Image Velocimetry (PIV) measurements result in a discrepancy in data quality, limiting the direct validation of computational simulations with experiments. These factors necessitate a careful interpretation of simulation data, acknowledging the inherent limitations and the complex nature of the flow fields around the combustion zone. This section seeks to present an overview of the simulated flow dynamics.

5.3.1 Streamlines and velocity field

This figure 5.9 presents a comprehensive study of flow field characteristics for a fully premixed flame across FF and LF investigations, highlighting the distinct behaviour of hydrogen-enriched flames within a single nozzle FLOX[®] burner. The burner operation involves high-momentum jets emanating from the nozzle, which induces vigorous recirculation within the combustion chamber. This mechanism promotes the thorough blending of

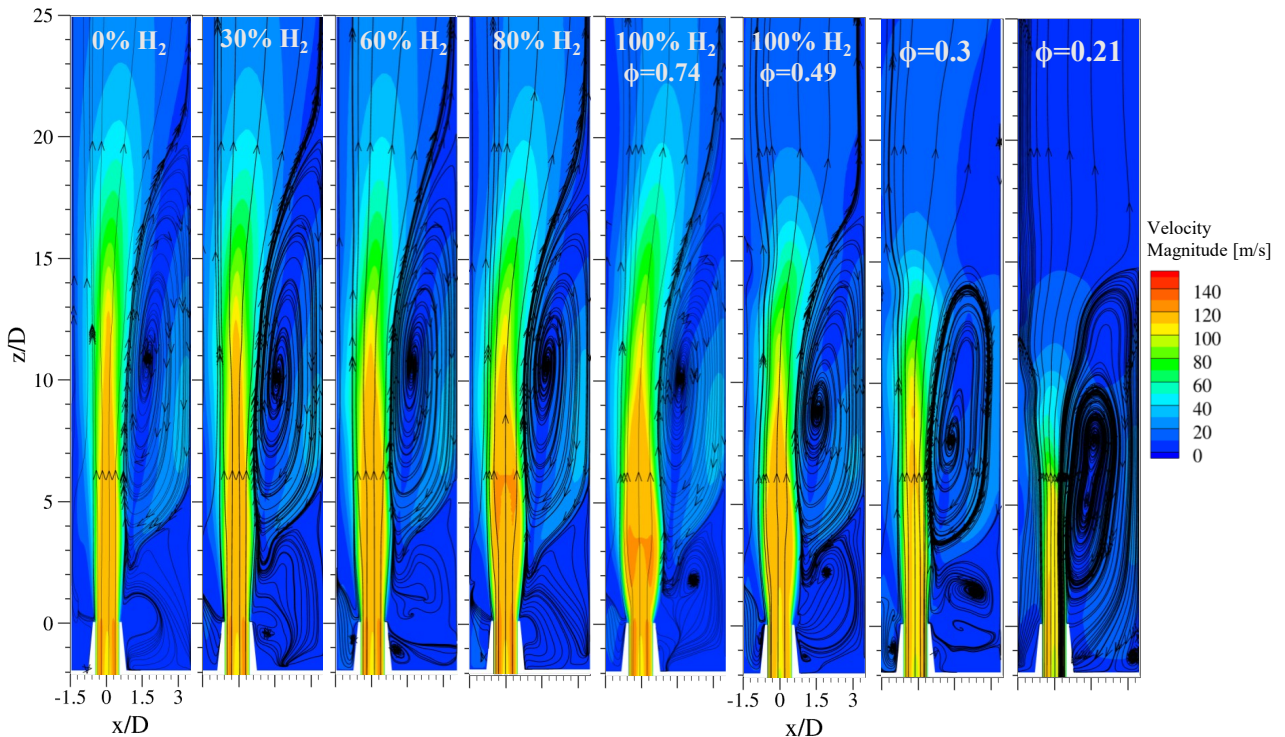


Figure 5.9: Flow field characteristics in FP configuration, showcasing the effect of varying vol.% H₂ and equivalence ratio (Φ) on recirculation zones and velocity magnitude near the nozzle exit.

the combusted gases with the fresh fuel and air mixture, enhancing flashback resistance by avoiding low velocity zones, thereby making the burner adaptable to a diverse spectrum of fuels. The IRZ is depicted by broad regions with elliptical streamlines, contrasting with the straight streamlines at $x/D = 0$ that signify the high-momentum jet. At lower vol.%

H_2 , the streamlines demonstrate a stable jet profile with relatively straight trajectories emanating from the nozzle, which is attributed to methane's lower reactivity and elevated LOH. As the hydrogen content increases, the IRZ becomes more prominent, with a centre that moves progressively closer to the nozzle exit. This shift aligns with the increasing reactivity of hydrogen, which stabilizes the flame at lower heights, as depicted by the shrinking LOH across the FF series. It also suggests that the flow field transitions from a jet-dominated regime to one where recirculation and premixing dynamics are predominant.

Furthermore, the presence of shear layers, visible as regions with gradients in velocity between the jet and IRZ, is pivotal for flame stability and mixing efficiency. The shear layers become pronounced as the hydrogen concentration rises, indicative of the intense mixing required to sustain combustion at higher reaction rates associated with hydrogen. As Φ decreases, the flames show a higher LOH, and the streamlines become more dispersed. This dispersion points to the decreased stability and increased likelihood of flame blow-off. At $\Phi=0.21$, the IRZ's distorted shape suggests the flame is moving up and down, behaviour that RANS simulations can't model. The flame, struggling due to cooler temperatures and less fuel, leads to a higher LOH and a more unstable burning process.

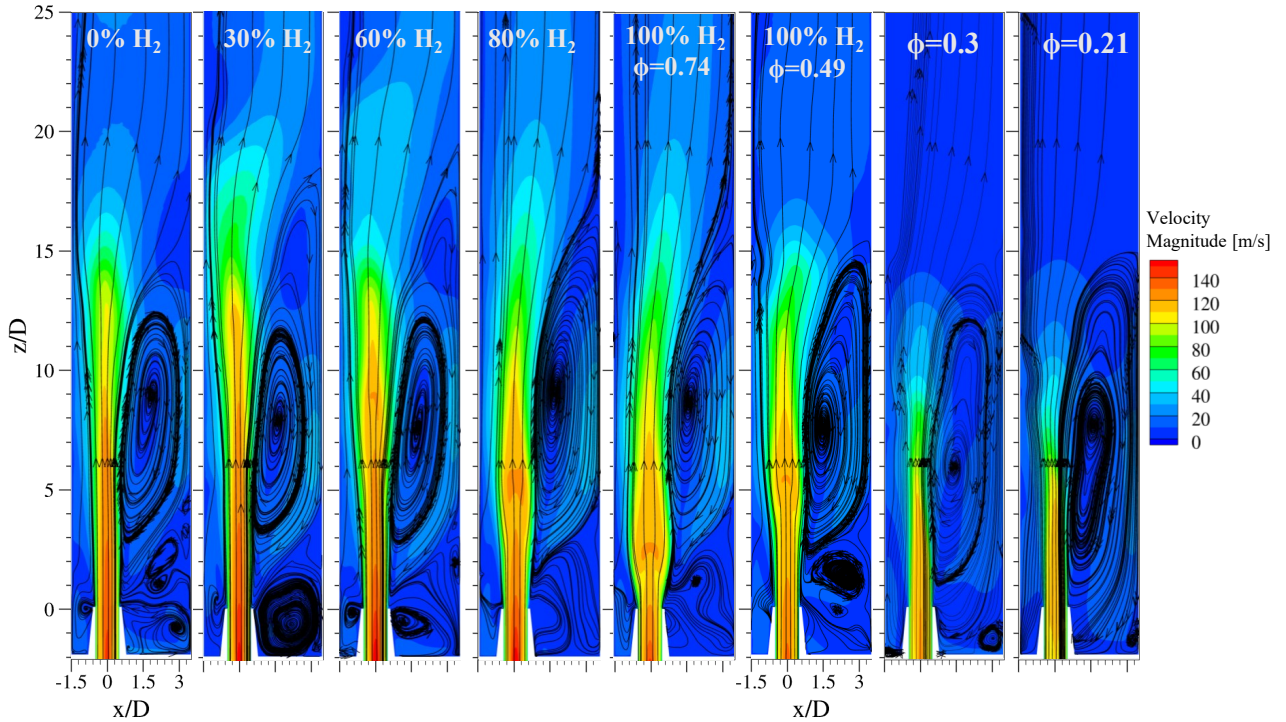


Figure 5.10: Flow field characteristics in TP configuration, showcasing the effect of varying vol.% H_2 and equivalence ratio (Φ) on recirculation zones and velocity magnitude near the nozzle exit.

In the TP combustion scenario, the velocity fields depicted in figure 5.10 resonate with the characteristics observed experimentally. Streamlines at $x/D = 0$ maintain their straight path, indicative of a high-velocity jet emanating from the nozzle. The gradual bending and expansion of these streamlines, particularly visible as hydrogen concentration escalates, point to the IRZ's increased influence. Notably, at 100 vol.% H_2 , the velocity profile suggests a robust momentum that is maintained further downstream, with marked expansion occurring at $z/D=2$, which aligns with the identified region of intensified mixing and flame stabilization. The velocity magnitudes, which peak at approximately 120 m/s

in the vicinity of the nozzle exit for both methane and hydrogen scenarios, hint at the homogenizing effect of the technical premixing approach. The IRZ is closer to the nozzle compared to the NP configuration, illustrating a more confined recirculation zone that supports stable combustion. As the equivalence ratio diminishes, the streamlines in the TP configuration depict a discernible deformation, especially at $\Phi = 0.21$, reflecting a challenging environment for flame stabilization.

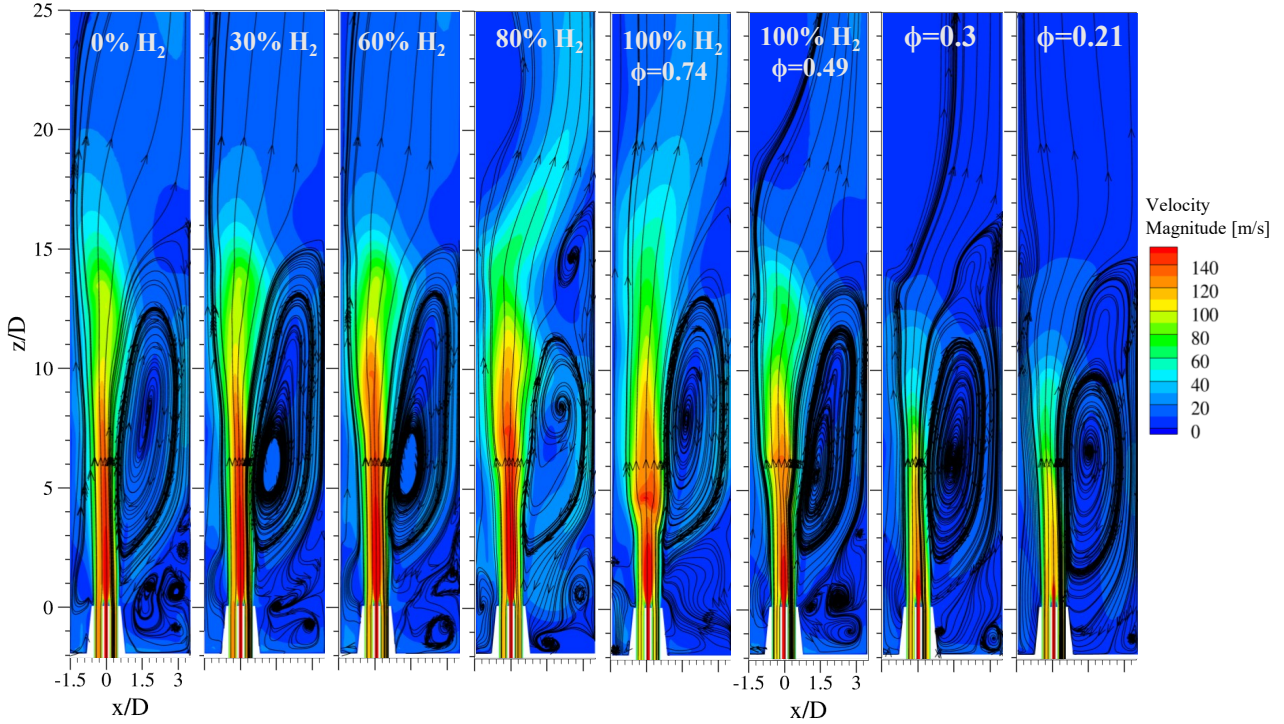


Figure 5.11: Flow field characteristics in NP configuration, showcasing the effect of varying vol.% H₂ and equivalence ratio (Φ) on recirculation zones and velocity magnitude near the nozzle exit.

For the NP case, as visualized in Figure 5.11, the flow field presents a stark distinction from the previously discussed FP and TP cases. The flow fields are characterized by high momentum with a clear core where the streamlines remain notably straight, indicative of the unreacted fuel as it exits the nozzle. The straight streamlines are observed to persist until approximately $x/D = 10$, beyond which a gradual diversion, marks the onset of recirculation processes. As we progress through the series from 0% to 100% H₂, the momentum of the jet is observed to remain substantial, that is likely due to the low density and high reactivity of hydrogen. The shear layers, evident by the gradient in velocity between the jet and IRZ, showcase the critical zones of intense mixing. The flow field appears more turbulent, especially as the H₂ content rises, with greater fluctuations indicating robust mixing necessary for the sustenance of combustion in the NP configuration. At a decreased Φ , the flow field reveals increased instability, a trend that complies with the experimental findings of heightened LOH and unstable flame characteristics near the LBO limit.

In conclusion, the NP flow field portrays the classical behaviour of non-premixed flames, with a prominent jet structure and a clear segregation between fuel and oxidizer prior to mixing and combustion. The simulations capture the essential features observed experimentally, reaffirming the utility of computational methods in predicting flow behaviours

and offering insights into the mixing and combustion processes.

5.3.2 Velocity profiles for fuel flexibility investigations

This subsection is dedicated to the analysis of velocity profiles obtained through line sampling across the computational domain at axial distances $z/D = 0.1$, $z/D = 7.5$, and $z/D = 15$ from the nozzle exit. These profiles provide a quantitative understanding of the flow dynamics under different hydrogen enrichment scenarios. At $z/D = 0.1$, close

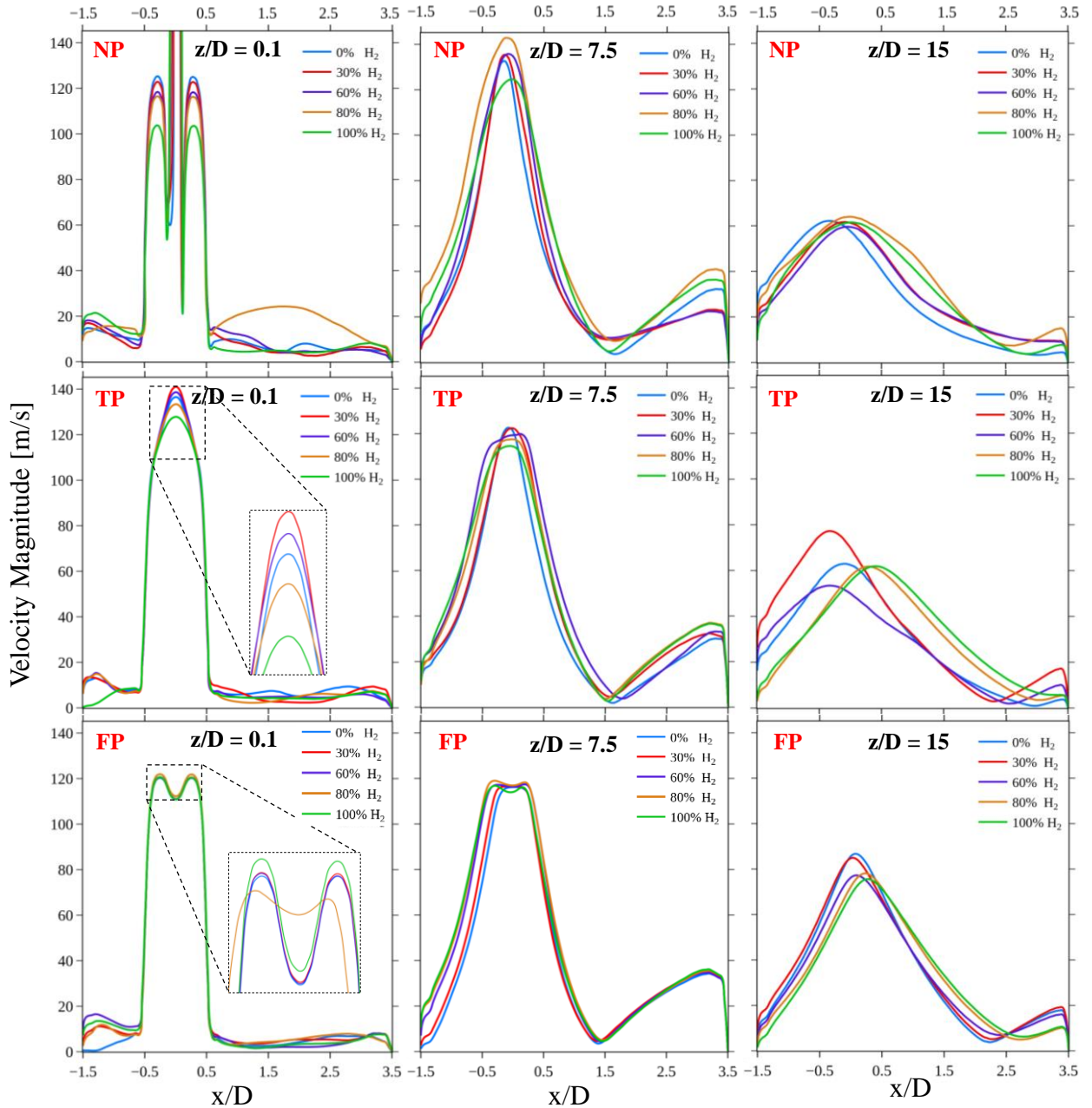


Figure 5.12: Velocity profiles at axial distances of $0.1D$, $7.5D$ and $15D$ for FF investigation on NP, TP and FP configurations. The x-axis represents the combustor width, and the y-axis represents the velocity magnitude.

to the nozzle exit, the profiles reflect the initial momentum distribution of the jet as it

enters the combustion chamber. The velocity peak indicates the jet's core momentum, which is pivotal for flame stabilization and mixing efficacy. With increasing hydrogen content, a notable shift in the velocity peaks is observed, indicative of the higher reactivity and faster mixing rates associated with hydrogen flames. At a distance of $z/D = 7.5$, the velocity profiles capture the evolution of the flow as it interacts with the recirculation zones. The shear layers, identifiable by the gradient in velocity across the jet's boundary, become more pronounced with higher hydrogen percentages, signalling enhanced mixing processes critical for flame stabilization. Further downstream, at $z/D = 15$, the profiles are indicative of the flow's adjustment to the combustor's conditions. The decay in velocity magnitudes, along with the dispersion of the velocity peaks, reflects the jet's momentum dissipation and the increasing influence of the recirculation dynamics.

For the NP configuration, at $z/D = 0.1$, the profiles are sharply peaked, indicating a high momentum jet velocity near the nozzle exit, and a clear segregation between fuel and oxidizer prior to mixing. At greater distances from the nozzle ($z/D = 7.5$ and 15), the profiles become flatter and wider, demonstrating the jet's dispersion. For 100 vol.%H₂ the maximum velocity at the nozzle outlet is significantly lower, which suggests a reduced LOH and confined reaction zone. The TP configuration shows a similar trend, but with less pronounced peaks and homogeneous velocity distribution even at $z/D = 0.1$. This is likely a result of the premixing, which facilitates a uniform fuel-air mixture before combustion. The velocity profiles at $z/D = 7.5$ exhibit a flow reversal which marks the presence of the IRZ, aligning with an increased degree of mixing. In the FP case, the profiles at $z/D = 0.1$ exhibit double peaks, indicating a complex flow structure likely influenced by the interaction between the fuel-air mixture. Further downstream, the profiles at $z/D = 7.5$ and 15 show a significant reduction in magnitude.

This line sampling approach substantiates the observations from contour plots by providing a precise quantitative measure of the velocity field, allowing for a robust analysis of the flow dynamics under varying fuel compositions. The data underscores the impact of hydrogen enrichment on the velocity profiles and, by extension, the operational flexibility of the burner to accommodate a wide spectrum of fuel mixtures.

5.4 Evaluation of Temperature field

The temperature profiles extracted from line probes at $x/D = 0$ provide vital insights into the thermal characteristics within the combustion chamber for FF investigation. These profiles are crucial for understanding the temperature distribution, reaction zone characteristics, and the potential zones for formation of thermal NO_x. In the NP configuration, the temperature profile demonstrates a notable variation with increasing distance along the burner's length. Initial temperatures near the nozzle are relatively lower, indicating cooler inflow mixtures. As the probe extends further from the nozzle, there is a gradual increase in temperature, reaching a peak where the combustion is most intense before tapering off. This peak correlates with the primary reaction zone, where fuel and oxidizer mix optimally under high-temperature conditions conducive to vigorous combustion reactions.

5.4. EVALUATION OF TEMPERATURE FIELD

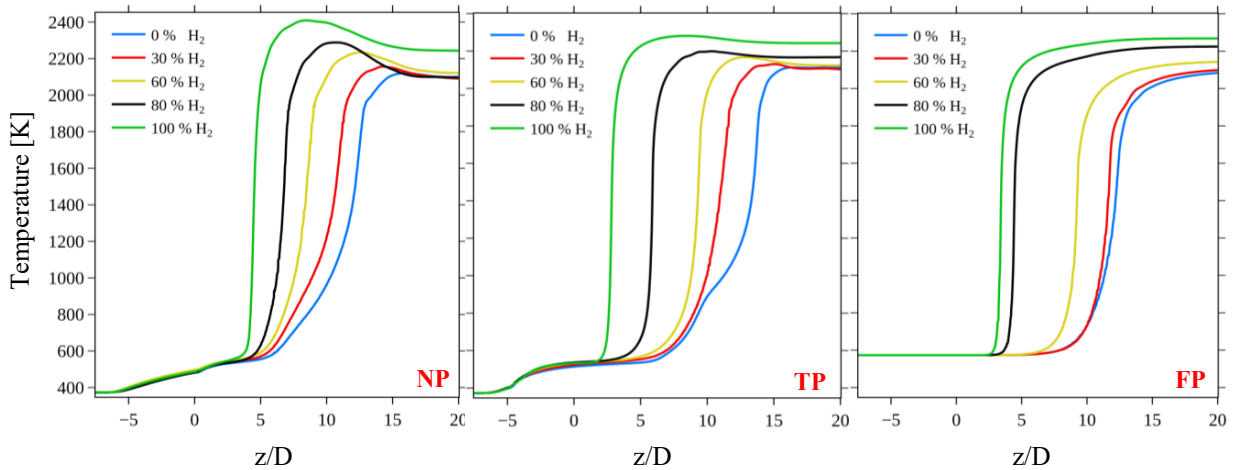


Figure 5.13: Temperature distribution for NP, TP, and FP configurations at varying vol.% H₂.

Switching to the FP setup, the fuel enters the combustion temperature at 573K, reflecting the uniform pre-mixture of fuel and air which facilitates more immediate combustion upon ignition. The peak temperatures are observed closer to the nozzle compared to the NP setup, suggesting a more compact and intense combustion zone. This configuration minimizes the formation of unburnt hydrocarbons and potentially reduces emissions, owing to the efficient use of the fuel-air mixture and rapid achievement of peak combustion temperatures.

The TP scenario exhibits a temperature profile that blends characteristics of both NP and FP setups. Initial temperatures rise moderately, indicating a controlled mixing process that prevents premature ignition but ensures that the combustion zone remains compact and well-defined. The temperature peak, while not as pronounced as in the FP configuration, occurs earlier than in the NP setup, illustrating the effectiveness of technical premixing in achieving a balance between emission control and combustion efficacy. In each configuration, the observed temperature trends are consistent with quantitative evaluation of LOH (refer subsection 5.1.2)

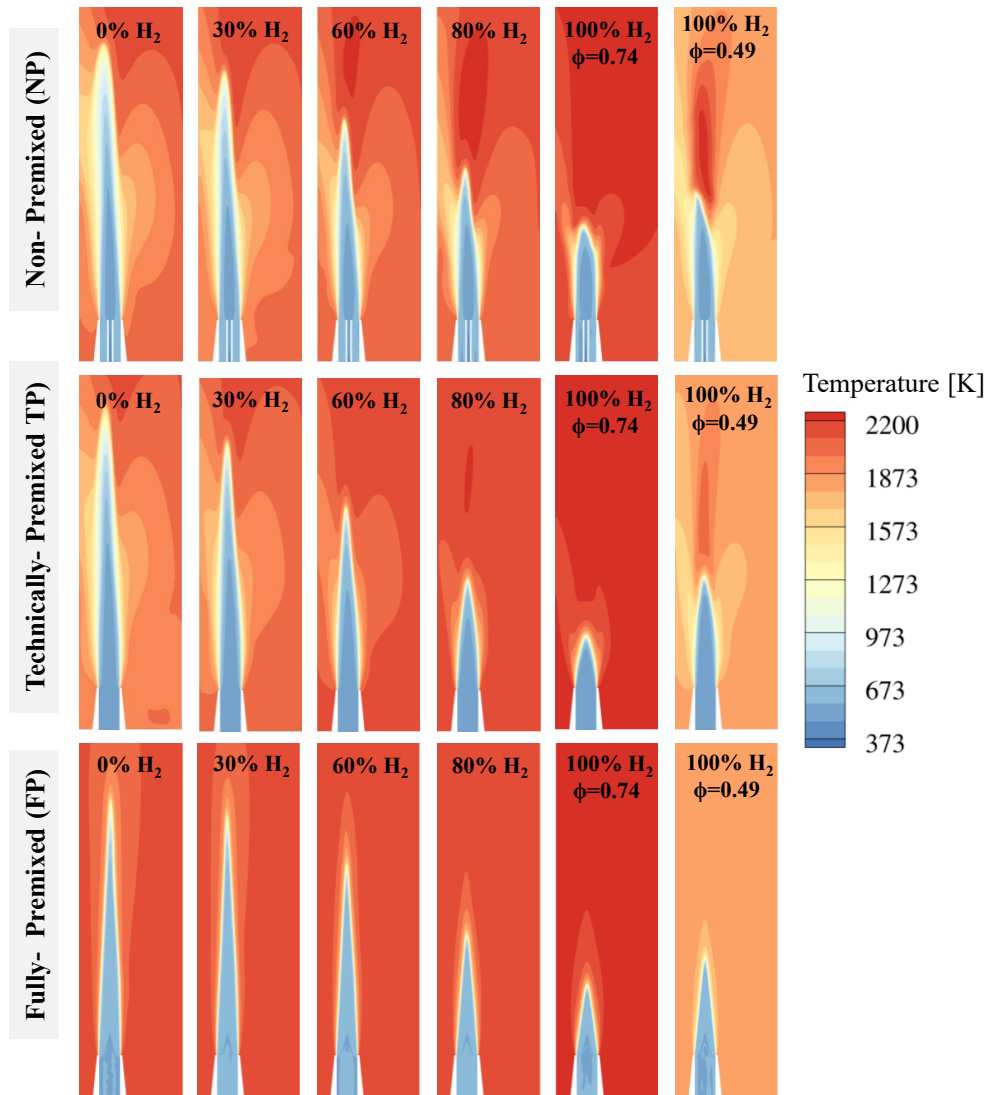


Figure 5.14: Contours of temperature distribution in NP, TP, and FP configurations under FF and LF investigations.

The temperature distribution within the NP configuration, as depicted in the above figure, shows the commencement of the reaction zone through the transition from cool to warm hues away from the nozzle. The progression to higher temperatures suggests active combustion, with the reaction zone moving closer to the nozzle as the hydrogen content increases. These temperature shifts align with the previously discussed compact reaction zones and are in agreement with the flame shape and lift-off height analysis, as well as the observations regarding flow recirculation and velocity profiles.

The TP configuration temperature fields balance between the pronounced stratification observed in NP and the uniformity characteristic of FP. For FP scenarios, the contours consistently present a uniform temperature distribution, especially notable at higher H₂ content. This homogeneity in thermal profiles across the combustor for FP is demonstrative of the successful integration of fuel and oxidizer, leading to a controlled and immediate combustion response upon ignition. The pronounced thermal zones close to the nozzle in the FP setup also imply the potential for higher wall heat fluxes, which might necessitate additional considerations in burner design to manage thermal stresses. Lower equivalence ratios present across the configurations reflect in reduced temperatures,

supporting earlier inferences regarding leaner mixtures leading to cooler combustion and bigger flame stabilization challenges.

This analysis supports the idea that premixing levels are intrinsically tied to the temperature distribution within the combustion chamber. It affirms the combustion characteristics deduced from the velocity and LOH studies. Contour analysis thus offers a nuanced comprehension of how variations in hydrogen content and premixing strategies can be manipulated to tailor combustion behaviour for optimized burner performance and reduced emission profiles. RANS simulations, by their steady-state nature, inherently provide an average picture of the temperature distribution. This is evident from the extensive high-temperature regions indicating that over time, the combustor operates within a relatively steady thermal environment, which is important for understanding the overall heat management within the system and is essential for designing burners capable of withstanding sustained high temperatures, thus ensuring structural integrity and operational safety.

Chapter 6

Summary and outlook

The primary purpose of this thesis is to conduct a comprehensive benchmark analysis of the combustion dynamics within a single-nozzle FLOX[®] burner, scrutinizing its behaviour under diverse fuel compositions and operating conditions (refer 4.1) across non-premixed (NP), technically premixed (TP), and fully premixed (FP) configurations.

This work aims to enhance the accuracy and applicability of DLR's hydrogen combustion simulations, specifically addressing fuel and load flexibility, by using experimental measurements and findings [20] to validate the RANS simulations. The simulation workflow is managed through parameter files in ThetaCOM (DLR's combustion CFD code), which streamline the setup of pre-processing and solver settings. Steady-state RANS simulations begin with a cold-flow setup, then progress to EDM and FRC models, using a specific variant of the DLR Concise Version 1 detailed reaction mechanism and the Standard $k-\omega$ turbulence model. Mesh quality and refinement significantly influence the fidelity of simulations, impacting factors like accuracy, convergence rates, and computational resource utilization. This thesis leverages ANSYS Meshing and a rigorous mesh dependency study to identify the ideal mesh refinement level within the reaction zone, focusing on flame lift-off height (LOH) and NO_x emissions. In summary, the mesh convergence study reveals that all meshes yield closely aligned solutions, corroborated by the low GCI values in Tables 4.3. This investigation identifies a cell size range of 0.45 mm to 0.70 mm in the reaction zone as optimal for both FF and LF investigations, balancing the trade-offs between computational demand and compliance to produce practically meaningful results.

The results of RANS simulations engage in a detailed comparative analysis across the NP, FP, and TP configurations. Central to these insights are the flame shape and LOH, whose variations underscore the combustors adaptability and the interplay between fuel composition, mixedness, and combustion dynamics. Through a combination of visual analysis using OH^* -CL contour plots and quantitative LOH measurements, the study reveals that increasing hydrogen content dramatically shortens LOH, creates more compact flames, and anchors them closer to the nozzle due to hydrogen's high reactivity and flame speed. Premixing, both technical (TP) and full (FP), also enhances flame stability and reduces LOH compared to the non-premixed (NP) case. In load flexibility scenarios, decreasing the equivalence ratio (Φ) leads to an increased LOH as heat release decreases, causing flames to become less stable and approach LBO. While RANS simulations generally replicate these trends, they tend to slightly underestimate flame width compared to experiments, particularly near LBO. This finding highlights the importance of considering

both hydrogen content and premixing strategies in fuel-flexible combustor design, and suggests that transient modelling techniques (like LES) may be needed to fully capture flame dynamics in very lean conditions.

The integration of hydrogen as a primary fuel component represents a pivotal shift towards environmentally conscious combustion practices. This transition, however, introduces new complexities in the emission profiles of nitrogen oxides (NO_x), pollutants that are the focus of stringent emission standards due to their adverse environmental and health effects. Increasing hydrogen content generally leads to higher NO_x emissions due to hydrogen's faster combustion and associated higher temperatures. Premixing fuel and air (both TP and NP) reduces NO_x compared to NP cases by creating more uniform combustion conditions and minimizing localized hot spots. Leaner mixtures also result in lower NO_x emissions due to decreased flame temperatures. Interestingly, there's a trade-off between CO and NO_x emissions: increasing hydrogen reduces CO (promoting more complete combustion) but can increase NO_x due to higher temperatures. While RANS simulations capture the general trends in NO_x emissions, some discrepancies with experimental data arise, especially at very high hydrogen content or near the lean blow-off limit. This emphasizes the challenges of accurately modelling emissions at the ppm level.

The flow field contours offer valuable insights into jet stabilization, where high-momentum fuel jets create strong recirculation zones within the combustion chamber. This recirculation enhances mixing and flashback resistance, making the burner adaptable to various fuels. Direct comparison with experimental data is limited due to field-of-view and seeding challenges. In FP operation, the IRZ becomes prominent and moves closer to the nozzle as hydrogen content increases. This reflects hydrogen's higher reactivity and shorter LOH. Additionally, shear layers between the jet and IRZ become more pronounced, indicating intense mixing. In technical premixing, a similar trend is observed, while in NP the flow field shows classic jet behaviour with clear fuel/oxidizer segregation before mixing. Lower equivalence ratios lead to increased instability and dispersed streamlines for all configurations. Velocity profiles along the combustor's length support these observations. Close to the nozzle, velocity peaks reflect the jet's initial momentum. With increasing hydrogen content, these peaks broaden, indicating faster mixing rates. Further downstream, the decay in velocity and broader peaks highlight the dissipation of jet momentum and the growing influence of recirculation. In the NP case, sharp peaks near the nozzle show clear fuel/oxidizer segregation, while premixing leads to even profiles, promoting uniform combustion conditions.

Temperature distributions within premixing configurations (both full and technical) leads to higher initial temperatures and faster combustion compared to NP, resulting in more compact combustion zones closer to the nozzle. Increasing hydrogen content generally raises peak temperatures due to hydrogen's high reactivity, aligning with observations of shorter LOH for high-hydrogen fuels. Leaner mixtures expectedly result in lower overall temperatures, reflecting the challenges of flame stabilization at LBO. Temperature profiles and contour plots reveal the location and intensity of reaction zones, providing valuable insights into heat release patterns and identifying potential hotspots for thermal NO_x formation. Importantly, RANS simulations offer an averaged view of the temperature field, aiding in the understanding of overall heat management within the system. This understanding is crucial for designing combustors capable of withstanding the sustained high temperatures associated with hydrogen combustion.

While RANS simulations offer valuable insights into time-averaged flame behaviour and

trends, it is important to acknowledge their limitations. These include challenges in modelling transient phenomena, particularly near the LBO limit, and the over-prediction of NO_x emissions at the ppm level emphasize the necessity for more advanced modelling, such as LES or URANS, to accurately capture transient flame behaviour. Additionally, the current simulations assume adiabatic wall conditions for the combustor, which may lead to artificially high temperatures within the combustion chamber. Implementing accurate heat flux values for each operating condition would likely improve the simulation's ability to replicate experimental results, particularly regarding emissions, temperature distributions and LOH.

Bibliography

- [1] *The german electricity mix in 2022*. <https://www.unendlich-viel-energie.de/media-library/charts-and-data/german-electricity-mix>, 2024
- [2] LAMBERT, M.: THETA-Code Developer's Guide / German Aerospace Center (DLR), Institute of Aerodynamics and Flow Technology. 2011 (1). – Forschungsbericht. – Release 8.2
- [3] TUCCILLO, Raffaele ; CAMERETTI, MARIA C. u. a.: Combustion and combustors for MGT applications. In: *VKI/RTO Lecture Series on" Micro Gas Turbines* (2005), S. 5–1
- [4] GRIMM, Felix: Low-Order Reactor-Network-Based Prediction of Pollutant Emissions Applied to FLOX® Combustion. In: *Energies* 15 (2022), Nr. 5, S. 1740
- [5] KREJCI, Michael C. ; MATHIEU, Olivier ; VISSOTSKI, Andrew J. ; SANKARANARAYANAN, Ravi: Laminar Flame Speed and Ignition Delay Time Data for the Kinetic Modeling of Hydrogen and Syngas Fuel Blends. In: *Journal of Engineering for Gas Turbines and Power* 135 (2013), 01, Nr. 2, 021503. <http://dx.doi.org/10.1115/1.4007737>. – DOI 10.1115/1.4007737. – ISSN 0742–4795
- [6] DONOHOE, Nicola ; HEUFER, Alexander ; METCALFE, Wayne K.: Ignition delay times, laminar flame speeds, and mechanism validation for natural gas/hydrogen blends at elevated pressures. In: *Combustion and Flame* 161 (2014), Nr. 6, 1432-1443. <http://dx.doi.org/https://doi.org/10.1016/j.combustflame.2013.12.005>. – DOI <https://doi.org/10.1016/j.combustflame.2013.12.005>. – ISSN 0010–2180
- [7] LAW, C.K. ; MAKINO, A. ; LU, T.F.: On the off-stoichiometric peaking of adiabatic flame temperature. In: *Combustion and Flame* 145 (2006), Nr. 4, 808-819. <http://dx.doi.org/https://doi.org/10.1016/j.combustflame.2006.01.009>. – DOI <https://doi.org/10.1016/j.combustflame.2006.01.009>. – ISSN 0010–2180
- [8] ZELDOVICH, Y. B.: The Oxidation of Nitrogen in Combustion and Explosions. In: *Acta Physicochim. SSSR* (1946), S. 577–625
- [9] GLASSMAN, Irvin ; YETTER, Richard A. ; GLUMAC, Nick G.: *Combustion*. Academic press, 2014
- [10] *Hydrogen data (2018), Presented by HyWeb*. <http://www.h2data.de/>. Version: 2018
- [11] LACKNER, Maximilian ; PALOTÁS, Árpád ; WINTER, Franz: *Combustion: from basics to applications*. John Wiley & Sons, 2013

-
- [12] IEA *World Energy outlook*. <https://www.iea.org/reports/world-energy-outlook-2023>, Accessed: March 15, 2024
- [13] GATZEN, Christoph: *The economics of power storage: theory and empirical analysis for central europe*. Bd. 63. Oldenbourg Industrieverlag, 2008
- [14] STOLTEN, Detlef ; EMONTS, Bernd: *Hydrogen Science and Engineering, 2 Volume Set: Materials, Processes, Systems, and Technology*. Bd. 1. John Wiley & Sons, 2016
- [15] NOBLE, David ; WU, David ; EMERSON, Benjamin ; SHEPPARD, Scott ; LIEUWEN, Tim ; ANGELLO, Leonard: Assessment of Current Capabilities and Near-Term Availability of Hydrogen-Fired Gas Turbines Considering a Low-Carbon Future. In: *Journal of Engineering for Gas Turbines and Power* 143 (2021), 02, Nr. 4, 041002. <https://doi.org/10.1115/1.4049346>. – ISSN 0742–4795
- [16] TAAMALLAH, Soufien ; VOGIATZAKI, Konstantina ; ALZHRANI, Fahad M. ; MOKHEIMER, Esmail M. ; HABIB, MA ; GHONIEM, Ahmed F.: Fuel flexibility, stability and emissions in premixed hydrogen-rich gas turbine combustion: Technology, fundamentals, and numerical simulations. In: *Applied energy* 154 (2015), S. 1020–1047
- [17] ALHUYI NAZARI, Mohammad ; FAHIM ALAVI, Morteza ; SALEM, Mohamed ; ASSAD, Mamdouh El H.: Utilization of hydrogen in gas turbines: A comprehensive review. In: *International Journal of Low-Carbon Technologies* 17 (2022), S. 513–519
- [18] ZHANG, Y. ; DAVIS, D. ; BREAR, M. J.: The role of hydrogen in decarbonizing a coupled energy system. In: *Journal of Cleaner Production* 346 (2022), 04. <http://dx.doi.org/10.1016/J.JCLEPRO.2022.131082>. – DOI 10.1016/J.JCLEPRO.2022.131082
- [19] LELLEK, S ; SATTELMAYER, T: NO_x-formation and CO-burnout in water-injected, premixed natural gas flames at typical gas turbine combustor residence times. In: *Journal of Engineering for Gas Turbines and Power* 140 (2018), Nr. 5, S. 051504
- [20] PETRY, Niklas ; MANNAZHI, Manu ; YIN, Zhiyao ; LAMMEL, Oliver ; GEIGLE, Klaus P. ; HUBER, Andreas: Investigation of Fuel and Load Flexibility of an Atmospheric Single Nozzle Jet-Stabilized FLOX® Combustor with Hydrogen/methane-Air Mixtures. In: *Journal of Engineering for Gas Turbines and Power* (2024), S. 1–11
- [21] WÜNNING, Joachim A. ; WÜNNING, Joachim G.: Flameless Oxidation to Reduce Thermal NO-Formation. In: *Progress in Energy and Combustion Science* 23 (1997), Nr. 1, S. 81–94
- [22] AIGNER, Manfred ; SEITZ, Arne ; HASEGAWA, Tatsuya: Flameless Combustion and its Application Towards Gas Turbines. In: *Energy Procedia* 37 (2013), S. 1180–1186
- [23] KELLER, Jay O. ; BRAMLETTE, T T. ; SWEENEY, Mark S. ; TREE, Dale R.: Flameless Combustion: A Contribution Towards Clean Combustion Technology. In: *Journal of Engineering for Gas Turbines and Power* 131 (2009), Nr. 2, S. 021506
- [24] ZORNEK, T. ; MONZ, T. ; AIGNER, M.: A micro gas turbine combustor for the use of product gases from biomass gasification. In: *Proceedings of the 6th European Combustion Meeting*, 2013, S. 5–19

- [25] ZANGER, Jan ; THOMAS, Monz ; MANFRED, Aigner: Experimental Investigation of the Influence of Combustor Cooling on the Characteristics of a FLOXI-Based Micro Gas Turbine Combustor. Version: 2013. <https://doi.org/10.5772/54405>. In: BENINI, Ernesto (Hrsg.): *Progress in Gas Turbine Performance*. Rijeka : IntechOpen, 2013, Kapitel 7
- [26] IZADI, S ; ZANGER, J ; KISLAT, O ; ENDERLE, B ; GRIMM, F ; KUTNE, P ; AIGNER, M: Experimental investigation of the combustion behavior of single-nozzle liquid-FLOX-based burners on an atmospheric test rig. In: *Journal of Engineering for Gas Turbines and Power* 143 (2021), Nr. 7, S. 071021
- [27] FORTENBACH, R.: *Mehrskalenmodellierung von aeroakustischen Quellen in schwach kompressibler Strömungen*, University of Stuttgart, Institute of Aerodynamics and Gasdynamics, Ph.D. thesis, 2006. – In German
- [28] DI DOMENICO, M.: *Numerical Simulation of Soot Formation in Turbulent Flows*, University of Stuttgart, Institute of Combustion Technology for Aerospace Engineering, Ph.D. thesis, 2008
- [29] SETZWEIN, F.: *Untersuchungen zu Verbrennungslärm in einer Modellbrennkammer unter Berücksichtigung verschiedener Verbrennungsparameter*, Universität Stuttgart, Institut für Feuerungs- und Kraftwerkstechnik, Diplomarbeit, 2016
- [30] MÜHLBAUER, B.: *Numerische Simulation von Verbrennungslärm*, Universität Stuttgart, Institut für Verbrennungstechnik der Luft- und Raumfahrt, Dissertation, 2012. <http://elib.uni-stuttgart.de/opus/volltexte/2012/7137/>
- [31] REICHLING, G.: *Development of numerical methods for the calculation of thermo-acoustic interactions in gas turbine combustion chambers*, University of Stuttgart, Institute of Combustion Technology for Aerospace Engineering, Diss., 2015. <http://dx.doi.org/http://dx.doi.org/10.18419/opus-3961>. – DOI <http://dx.doi.org/10.18419/opus-3961>
- [32] LECHELER, S.: *Numerische Strömungsberechnung: Schneller Einstieg in ANSYS CFX 18 durch einfache Beispiele*. Springer Fachmedien Wiesbaden, 2017 <https://books.google.de/books?id=kx0-DwAAQBAJ>. – ISBN 9783658191924
- [33] KIMMERLE, W. ; STROPPEL, M.: *Analysis für Ingenieure, Mathematiker und Physiker*. edition delkhofen, 2009 <https://books.google.de/books?id=d1JYcgAACAAJ>. – ISBN 9783936413236
- [34] GERLINGER, P.: *Numerische Verbrennungssimulation, Effiziente numerische Simulation turbulenter Verbrennung*. Springer, 2005 <https://books.google.de/books?id=Su4mBAAQBAJ>. – ISBN 9783540233374. – In German
- [35] POPE, S. B.: PDF Methods for Turbulent Reactive Flows. In: *Progress in Energy and Combustion Science* 11 (1985), S. 119–192
- [36] ROLLER, S.: *Ein numerisches Verfahren zur Simulation schwach kompressibler Strömungen*, University of Stuttgart, Institute of Aerodynamics and Gasdynamics, Ph.D. thesis, 2005. – In German

- [37] LOURIER, J. M.: *Numerische Simulation von thermoakustischen Instabilitäten in Gasturbinenbrennkammern mithilfe von Impedanzrandbedingungen*, Deutsches Zentrum für Luft- und Raumfahrt, Institut für Verbrennungstechnik, Dissertation, 2016. http://elib.dlr.de/105654/1/Dissertation_Lourier_20290616.pdf
- [38] OUMERACI, Hocine: *Vorlesungsskript Hydromechanik*. 2015. – Lecture notes by Prof. Dr.-Ing. Hocine Oumeraci
- [39] SCHWARZE, R.: *CFD-Modellierung: Grundlagen und Anwendungen bei Strömungsprozessen*. Springer Berlin Heidelberg, 2012 https://books.google.de/books?id=vFGEkds_zY0C. – ISBN 9783642243776
- [40] VERSTEEG, W. ; MALALASEKERA, H. K.: *An Introduction to Computational Fluid Dynamics: The Finite Volume Method*. Pearson Education Limited, 2007 <https://books.google.de/books?id=RvBZ-UMpGzIC>. – ISBN 9780131274983
- [41] OBERLACK, M. ; KHUJADZE, G. ; AVSARKISOV, V. ; WANG, Y.: Direkte Numerische Simulation der Turbulenz. In: *Wissenschaftsmagazin forschen 2* (2011), S. 32–35
- [42] CHEN, C. J.: *Fundamentals Of Turbulence Modelling*. Taylor & Francis, 1997 <https://books.google.de/books?id=HSCUGJ1n8tgC>. – ISBN 9781560324058
- [43] BÖCKH, P. ; SAUMWEBER, C.: *Fluidmechanik: Einführendes Lehrbuch*. Springer Berlin Heidelberg, 2013 <https://books.google.de/books?id=D1kEMpNa3wC>. – ISBN 9783642338922
- [44] GRIMM, F.: *Effiziente, stochastische Vorhersage von turbulentem Brennkammerlärm*, Deutsches Zentrum für Luft- und Raumfahrt, Institut für Verbrennungstechnik, Dissertation, 2017. <https://elib.uni-stuttgart.de/handle/11682/9600>
- [45] SANNA, G. ; TOMASSETTI, G.: *Introduction to molecular beams gas dynamics*. World Scientific, 2005
- [46] JONES, W. P. ; LAUNDER, B.: The prediction of laminarization with a two-equation model of turbulence. In: *International Journal of Heat and Mass Transfer* 15 (1972), Nr. 2, S. 301–314
- [47] BOUSSINESQ, J.: *Essai sur la théorie des eaux courantes*. Imprimerie Nationale, 1877 <https://books.google.de/books?id=4NdQAAAAYAAJ>
- [48] SAGAUT, P. ; DECK, D. ; TERRACOL, M.: *Multiscale and Multiresolution Approaches in Turbulence*. Imperial College Press, 2006
- [49] TAY WO CHONG HILARES, Luis R.: *Numerical Simulation of the Dynamics of Turbulent Swirling Flames*, Lehrstuhl für Thermodynamik, Technische Universität München, Diss., 2012. <https://mediatum.ub.tum.de/doc/1093223/1093223.pdf>
- [50] MENTER, F. R. ; EGOROV, Y.: The scale-adaptive simulation method for unsteady turbulent flow predictions. Part 1: Theory and model description. In: *Flow, Turbulence and Combustion* 85 (2010), Nr. 1, S. 113–138. <http://dx.doi.org/10.1007/s10494-010-9264-5>. – DOI 10.1007/s10494-010-9264-5

- [51] KNACKE, T.: *Numerische Simulation des Geräusches massiv abgelöster Strömung bei großer Reynoldszahl und kleiner Machzahl*. Universitätsverlag TU Berlin, 2015 https://books.google.de/books?id=D_XyBgAAQBAJ. – ISBN 9783798327351
- [52] KUNZ, O.: *PDF-Simulation von Verbrennungsvorgängen in praxisnahen Brennkammern*, Universität Stuttgart, Institut für Verbrennungstechnik, Diss., 2003
- [53] LAUNDER, B. E. ; SPALDING, D. B.: *The Numerical Computations of Turbulent Flows*. Imperial College of Science and Technology, 1973 <https://books.google.de/books?id=DUCKtgAACAAJ>
- [54] LAUNDER, B. E. ; REECE, G. J. ; RODI, W.: Progress in the development of a reynolds-stress turbulence closure. In: *Journal of Fluid Mechanics* 68 (1975), Nr. 3, S. 537–566
- [55] LAUNDER, B. E. ; SPALDING, D. B.: *Mathematical Models of Turbulence*. Academic Press, 1972 <https://books.google.de/books?id=CEGrGwAACAAJ>
- [56] LAUNDER, B. E. ; SHARMA, B. I.: Application of the Energy-dissipation Model of Turbulence to the Calculation of Flow Near a Spinning Disc / Imperial College of Science and Technology, Department of Mechanical Engineering. Version: 1974. <https://books.google.de/books?id=jwlemwEACAAJ>. 1974 (2). – Forschungsbericht. – HTS
- [57] WILCOX, D. C.: Multiscale model for turbulent flows. In: *AIAA Journal* 26 (1988), Nr. 11, S. 1311–1320
- [58] REICHLING, G. ; NOLL, B. ; AIGNER, M.: Numerical simulation of the non-reactive and reactive flow in a swirled model gas turbine combustor. In: *21st AIAA Computational Fluid Dynamics Conference*, 2013, S. 6–47
- [59] WILCOX, D. C.: *Turbulence Modeling for CFD*. DCW Industries, 2006 (Bd. 1 in Turbulence Modeling for CFD). <https://books.google.de/books?id=q4ypAQAAACAAJ>. – ISBN 9781928729082
- [60] MENTER, F. R.: Two-equation eddy-viscosity turbulence models for engineering applications. In: *AIAA Journal* 32 (1994), Nr. 8, S. 1598–1605
- [61] MENTER, F. R. ; KUNTZ, M. ; LANGTRY, R.: Ten years of industrial experience with the sst turbulence model. In: *Turbulence, Heat and Mass Transfer* 4 (2003), Nr. 1, S. 625–632
- [62] POPE, S. B.: Turbulent premixed flames. In: *Annual Review of Fluid Mechanics* 19 (1987), Nr. 1, S. 237–270
- [63] JOOS, F.: *Technische Verbrennung: Verbrennungstechnik, Verbrennungsmodellierung, Emissionen*. Springer Berlin Heidelberg, 2006 <https://books.google.de/books?id=NC4iBAAAQBAJ>. – ISBN 9783540343349
- [64] IMTEYAZ, B. A. ; NEMITALLAH, M. A. ; ABDELHAFEZ, A. A. ; HABIB, M. A.: Combustion behavior and stability map of hydrogen-enriched oxy-methane premixed flames in a model gas turbine combustor. In: *International Journal of Hydrogen Energy* 43 (2018), 08, Nr. 34, S. 16652–16666. <http://dx.doi.org/10.1016/J.IJHYDENE.2018.07.087>. – DOI 10.1016/J.IJHYDENE.2018.07.087

- [65] POINSOT, Thierry ; VEYNANTE, Denis: *Theoretical and Numerical Combustion*. R.T. Edwards, Inc., 2005
- [66] BAUKAL, C. E. ; ELEAZER, P. B.: Quantifying NO_x for industrial combustion processes. In: *Journal of the Air and Waste Management Association* 48 (1998), Nr. 1. <http://dx.doi.org/10.1080/10473289.1998.10463664>. – DOI 10.1080/10473289.1998.10463664. – ISSN 10473289
- [67] GUO, H. ; SMALLWOOD, G. J. ; LIU, F. ; JU, Y. ; GÜLDER, Ö. L.: The effect of hydrogen addition on flammability limit and NO_x emission in ultra-lean counterflow CH₄/air premixed flames. In: *Proceedings of the Combustion Institute* 30 (2005), 01, Nr. 1, S. 303–311. <http://dx.doi.org/10.1016/J.PROCI.2004.08.177>. – DOI 10.1016/J.PROCI.2004.08.177
- [68] LIEUWEN, T. C.: *Unsteady Combustor Physics*. Cambridge University Press, 2012
- [69] WARNATZ, J. ; MAAS, U. ; DIBBLE, R. W.: *Combustion: Physical and Chemical Fundamentals, Modeling and Simulation, Experiments, Pollutant Formation*. Springer Berlin Heidelberg, 2012 <https://books.google.de/books?id=DdnzCAAAQBAJ>. – ISBN 9783642980275
- [70] BORGHI, R. ; BRUNO, C. ; CASCI, C.: *Recent Advances in Aeronautical Science*. London, UK : Pergamon, 1984
- [71] PETERS, Norbert: *Turbulent Combustion*. Cambridge University Press, 2001
- [72] WILLIAMS, F. A.: Criteria for existence of wrinkled laminar flame structure of turbulent premixed flames. (1976)
- [73] RAJU, Darshan: *CFD Study on Flame Flashback in Low Swirl Premixed Burners*, Delft University of Technology (TU Delft), Mechanical, Maritime and Materials Engineering, Masters thesis, 08 2022. <http://resolver.tudelft.nl/uuid:4d0ab9d6-b6e4-4e48-92d9-4e6cda34f712>
- [74] EUROPEAN UNION: *Directive (EU) 2015/2193 of the European Parliament and of the Council on the limitation of emissions of certain pollutants into the air from medium combustion plants*. Official Journal of the European Union EN, 2014
- [75] SHIH, H. Y. ; LIU, C. R.: A computational study on the combustion of hydrogen/methane blended fuels for a micro gas turbines. In: *International Journal of Hydrogen Energy* 39 (2014), 09, Nr. 27, S. 15103–15115. <http://dx.doi.org/10.1016/J.IJHYDENE.2014.07.046>. – DOI 10.1016/J.IJHYDENE.2014.07.046
- [76] LEFEBVRE, A. H. ; BALLAL, D. R.: *Gas Turbine Combustion: Alternative Fuels and Emissions*. Taylor & Francis, 2010
- [77] TURNS, S. R.: *An Introduction to Combustion: Concepts and Applications*. McGraw-Hill, 2012 (McGraw-Hill Series in Mechanical Engineering). <https://books.google.de/books?id=idM8twAACAAJ>. – ISBN 9780071086875
- [78] KUO, K. K.: *Principles of Combustion*. John Wiley, 2005 <https://books.google.de/books?id=jAYoAQAAAJ>. – ISBN 9780471046899

- [79] MEISTER, A.: *Numerik linearer Gleichungssysteme: Eine Einführung in moderne Verfahren*. Springer Fachmedien Wiesbaden, 2014 https://books.google.de/books?id=Z_5MBQAAQBAJ. – ISBN 9783658072001
- [80] MAGNUSSEN, B. ; HJERTAGER, B.: On mathematical modeling of turbulent combustion with special emphasis on soot formation and combustion. In: *Symposium (International) on Combustion* Bd. 16, Elsevier, 1977, S. 719–729
- [81] MAGNUSSEN, B.: On the structure of turbulence and a generalized eddy dissipation concept for chemical reaction in turbulent flow. In: *19th Aerospace Sciences Meeting*, 1981, S. 6–21
- [82] SPALDING, D. B.: Mixing and chemical reaction in steady confined turbulent flames. In: *Symposium (International) on Combustion* Bd. 13, Elsevier, 1971, S. 649–657
- [83] GRAN, I. R. ; MAGNUSSEN, B.: A numerical study of a bluff-body stabilized diffusion flame. Part 2. Influence of combustion modeling and finite-rate chemistry. In: *Combustion Science and Technology* 119 (1996), Nr. 1-6, S. 191–217
- [84] MAGNUSSEN, B.: The eddy dissipation concept a bridge between science and technology. In: *ECCOMAS Thematic Conference on Computational Combustion*, 2005, S. 21–24
- [85] EPPLE, B. ; LEITHNER, R. ; LINZER, W. ; WALTER, H.: *Simulation von Kraftwerken und wärmetechnischen Anlagen*. Springer Vienna, 2009 <https://books.google.de/books?id=F7gmBAAAQBAJ>. – ISBN 9783211296974
- [86] ANSYS: *ANSYS® Academic Research*. Bd. 15317. 2013. – 23 S.
- [87] HACKBUSCH, W.: *Multigrid Methods and Applications*. Springer, 1985
- [88] YIN, Zhiyao ; BOXX, Isaac ; STÖHR, Michael ; LAMMEL, Oliver ; MEIER, Wolfgang: Confinement-induced instabilities in a jet-stabilized gas turbine model combustor. In: *Flow, Turbulence and Combustion* 98 (2017), S. 217–235
- [89] LAMMEL, Oliver ; STÖHR, Michael ; KUTNE, Peter ; DEM, Christoph ; MEIER, Wolfgang ; AIGNER, Manfred: Experimental analysis of confined jet flames by laser measurement techniques. In: *Combustion Science and Technology* 184 (2012), Nr. 6, S. 827–848
- [90] YIN, Zhiyao ; LAMMEL, Oliver ; GEIGLE, Klaus P. ; HUBER, Andreas: Investigation of Fuel and Load Flexibility of an Atmospheric Single Nozzle Jet-Stabilized FLOXVR Combustor With Hydrogen/Methane-Air Mixtures. In: *Journal of Engineering for Gas Turbines and Power* 146 (2024), Nr. 6, S. 061004–1
- [91] LÜCKERATH, R ; MEIER, W ; AIGNER, M: FLOX® combustion at high pressure with different fuel compositions. In: *Unknown* (Year not provided). – Paper details not provided
- [92] LAMMEL, O. ; SCHÜTZ, H. ; SCHMITZ, G. ; LÜCKERATH, R. ; STÖHR, M. ; NOLL, B. ; AIGNER, M. ; HASE, M. ; KREBS, W.: FLOX® combustion at high power density and high flame temperatures. In: *Journal of Engineering for Gas Turbines and Power* 132 (2010), Nr. 12

- [93] ROEDIGER, T. ; LAMMEL, O. ; AIGNER, M. ; BECK, C. ; KREBS, W.: Part-load operation of a piloted FLOX combustion system. 135 (2013), S. 031503
- [94] SELIGER, H. ; HUBER, A. ; AIGNER, M.: Experimental investigation of a FLOX-based combustor for a small-scale gas turbine based chp system under atmospheric conditions. In: *ASME Turbo Expo 2015: Turbine Technical Conference and Exposition* American Society of Mechanical Engineers, 2015, S. V04BT04A004
- [95] ZIZIN, A. ; LAMMEL, O. ; SEVERIN, M. ; AX, H. ; AIGNER, M.: Development of a jet-stabilized low-emission combustor for liquid fuels. In: *ASME Turbo Expo 2015: Turbine Technical Conference and Exposition* American Society of Mechanical Engineers, 2015, S. V04AT04A050
- [96] YIN, Z. ; NAU, P. ; BOXX, I. ; MEIER, W.: Characterization of a single-nozzle FLOX model combustor using kHz laser diagnostics. In: *ASME Turbo Expo 2015: Turbine Technical Conference and Exposition* American Society of Mechanical Engineers, 2015, S. V04BT04A017
- [97] SEMERARO, Onofrio ; BELLANI, Gabriele ; LUNDELL, Fredrik: Analysis of time-resolved PIV measurements of a confined turbulent jet using POD and Koopman modes. In: *Experiments in Fluids* 53 (2012), S. 1203–1220
- [98] HASEMANN-SEEGER, Stefan: *Entwicklung eines Brennkammersystems mit Abgasrückführung für den Einsatz in Mikrogasturbinen*, University of Stuttgart, Diss., 01 2019. https://elib.uni-stuttgart.de/bitstream/11682/10849/3/VT-FB_2020-01_StefanHasemann-Seeger.pdf
- [99] WANG, James F. Driscoll Jacqueline H. Chen Aaron W. Skiba Campbell D. Carter Evatt R. Hawkes H.: Premixed flames subjected to extreme turbulence: Some questions and recent answers. In: *Progress in Energy and Combustion Science* 76 (2020), 100802. <https://www.sciencedirect.com/science/article/pii/S036012851930036X>. – ISSN 0360–1285
- [100] SCHULZ, Oliver ; KEMPF, Andreas M. ; MEIER, Wolfgang: A criterion to distinguish autoignition and propagation applied to a lifted methane–air jet flame. In: *Proceedings of the Combustion Institute* 36 (2017), Nr. 2, S. 1637–1644
- [101] STEINBERG, Adam M. ; HAMLINGTON, Peter E. ; ZHAO, Xinyu: Structure and dynamics of highly turbulent premixed combustion. In: *Progress in Energy and Combustion Science* 85 (2021), 100900. <http://dx.doi.org/https://doi.org/10.1016/j.pecs.2020.100900>. – DOI <https://doi.org/10.1016/j.pecs.2020.100900>. – ISSN 0360–1285
- [102] CAVALIERE, Antonio ; DE JOANNON, Mara: Mild Combustion. In: *Progress in Energy and Combustion Science* 30 (2004), Nr. 4, 329–366. <https://www.sciencedirect.com/science/article/pii/S0360128504000127>. – ISSN 0360–1285
- [103] MI, Jianchun ; ZHAO, Yanping ; HU, Erqiang ; LI, Zhi ; LIU, Yuhao: Review on MILD combustion of gaseous fuel: its definition, ignition, evolution, and emissions. In: *Energy & Fuels* 35 (2021), Nr. 9, S. 7572–7607

- [104] PLANKE, Karl ; FARISCO, Federica ; GRIMM, Felix ; HUBER, Andreas: A Numerical Study on Hydrogen Jet Flame Combustion in MILD Conditions. In: *AIAA Scitech 2023 Forum*, 2023, S. 1098
- [105] NOH, D. ; NAVARRO-MARTINEZ, S.: Investigation of the Jet-Flame Interaction by Large Eddy Simulation and Proper Decomposition Method. In: *Combustion Science and Technology* 191 (2019), Nr. 5-6, 956-978. <http://dx.doi.org/10.1080/00102202.2019.1581775>. – DOI 10.1080/00102202.2019.1581775
- [106] SI, Jicang ; WANG, Guochang ; MI, Jianchun: Characterization of MILD Combustion of a Premixed CH₄/Air Jet Flame versus Its Conventional Counterpart. In: *ACS Omega* 4 (2019), Nr. 27, 22373-22384. <http://dx.doi.org/10.1021/acsomega.9b02711>. – DOI 10.1021/acsomega.9b02711. – PMID: 31911958
- [107] SCHÜTZ, H. u. a.: Analysis of the Pollutant Formation in the FLOX Combustion. In: *Proceedings of the ASME Turbo Expo: Power for Land, Sea and Air*, 2006, S. 5–31
- [108] SEVERIN, Michael ; LAMMEL, Oliver ; MEIER, Wolfgang: Laser diagnostic investigation of a confined premixed turbulent jet flame stabilized by recirculation. In: *Combustion and Flame* 243 (2022), S. 112061
- [109] MCKINSEY & COMPANY FOR THE CLEAN SKY 2 AND FUEL CELLS AND HYDROGEN 2 JOINT UNDERTAKING: *Hydrogen-Powered Aviation: A Fact-Based Study of Hydrogen Technology, Economics, and Climate Impact by 2050*. Publications Office, Luxembourg, 2020. – Available online: <https://op.europa.eu/en/publication-detail/-/publication/55fe3eb1-cc8a-11ea-adf7-01aa75ed71a1/language-en>
- [110] WILLIAMS, F. A.: *Combustion Theory: the fundamental theory of chemical reacting flow systems*. Addison-Wesley, 1965
- [111] SANKARAN, Ramanan ; G., Hong: Effects of hydrogen addition on the markstein length and flammability limit of stretched methane/air premixed flames. In: *Combustion Science and Technology* 178 (2006), Nr. 9, 1585-1611. <http://dx.doi.org/10.1080/00102200500536217>. – DOI 10.1080/00102200500536217
- [112] KELLER, J. O. ; VANEVELD, L. ; KORSCHULT, D. u. a.: Mechanism of Instabilities in Turbulent Combustion Leading to Flashback. In: *AIAA Journal* 20 (1982), 02, Nr. 2, S. 254–262. <http://dx.doi.org/10.2514/3.51073>. – DOI 10.2514/3.51073
- [113] LIEUWEN, T. ; McDONELL, V. ; SANTAVICCA, D. ; SATTELMAYER, T.: Burner Development and Operability Issues Associated with Steady Flowing Syngas Fired Combustors. In: *Combustion Science and Technology* 180 (2008), Nr. 6, S. 1169–1192. <http://dx.doi.org/10.1080/00102200801963375>. – DOI 10.1080/00102200801963375
- [114] TERRIE, P. ; BOGUSKI, K.: *Understanding units of measurement*. Environmental Science and Technology Briefs for Citizens, 2006
- [115] FÜRI, Marc ; PAPAS, Paul ; MONKEWITZ, Peter A.: Non-premixed jet flame pulsations near extinction. In: *Proceedings of the Combustion Institute* 28 (2000), Nr. 1, 831-838. [http://dx.doi.org/https://doi.org/10.1016/S0082-0784\(00\)80287-8](http://dx.doi.org/https://doi.org/10.1016/S0082-0784(00)80287-8). – DOI [https://doi.org/10.1016/S0082-0784\(00\)80287-8](https://doi.org/10.1016/S0082-0784(00)80287-8). – ISSN 1540-7489

- [116] CHAUDHURI, Swetaprovo ; KOSTKA, Stanislav ; RENFRO, Michael W. ; CETEGEN, Baki M.: Blowoff dynamics of bluff body stabilized turbulent premixed flames. In: *Combustion and Flame* 157 (2010), Nr. 4, 790-802. <http://dx.doi.org/https://doi.org/10.1016/j.combustflame.2009.10.020>. – DOI <https://doi.org/10.1016/j.combustflame.2009.10.020>. – ISSN 0010–2180
- [117] Turbo Expo: Power for Land, Sea, and Air (Veranst.): *Impacts of Hydrogen Addition on Near-Lean Blowout Dynamics in a Swirling Combustor*. Bd. *Volume 2: Turbo Expo 2007*. 2007 . – 189–198 S.
- [118] ZHU, Shengrong ; ACHARYA, Sumanta: An Experimental Study of Lean Blowout With Hydrogen-Enriched Fuels. In: *Journal of Engineering for Gas Turbines and Power* 134 (2012), 02, Nr. 4, 041507. <http://dx.doi.org/10.1115/1.4004742>. – DOI 10.1115/1.4004742. – ISSN 0742–4795
- [119] HOFERICHTER, V. ; SATTELMAYER, T.: *Boundary Layer Flashback in Premixed Hydrogen-Air Flames With Acoustic Excitation*
- [120] BURMBERGER, S. ; SATTELMAYER, T.: Optimization of the Aerodynamic Flame Stabilization for Fuel Flexible Gas Turbine Premix Burners. In: *Journal of Engineering for Gas Turbines and Power* 133 (2011), Nr. 10, S. 101501. <http://dx.doi.org/10.1115/1.4003066>. – DOI 10.1115/1.4003066
- [121] EICHLER, C. ; SATTELMAYER, T.: Experiments on Flame Flashback in a Quasi-2D Turbulent Wall Boundary Layer for Premixed Methane-Hydrogen-Air Mixtures. In: *Journal of Engineering for Gas Turbines and Power* 133 (2010), 09, Nr. 1. <http://dx.doi.org/10.1115/1.4001985>. – DOI 10.1115/1.4001985
- [122] FRITZ, J. ; KRÖNER, M. ; SATTELMAYER, T.: Flashback in a Swirl Burner With Cylindrical Premixing Zone. In: *Proceedings of ASME Turbo Expo 2001*, New Orleans, Louisiana, 2001, S. 06. – Paper No. 2001-GT-0054
- [123] BELLENOUE, B. Boust J. Sotton S.A. Labuda M.: A thermal formulation for single-wall quenching of transient laminar flames. In: *Combustion and Flame* 149 (2007), Nr. 3, 286-294. <http://dx.doi.org/https://doi.org/10.1016/j.combustflame.2006.12.019>. – DOI <https://doi.org/10.1016/j.combustflame.2006.12.019>. – ISSN 0010–2180
- [124] GRUBER, A. ; CHEN, J. H. ; VALIEV, D. ; LAW, C. K.: Direct numerical simulation of premixed flame boundary layer flashback in turbulent channel flow. In: *Journal of Fluid Mechanics* 709 (2012), S. 516–542. <http://dx.doi.org/10.1017/jfm.2012.345>. – DOI 10.1017/jfm.2012.345
- [125] LAPEYRE, C. J. ; MAZUR, M. ; SCOUFLAIRE, P. u. a.: Acoustically Induced Flashback in a Staged Swirl-Stabilized Combustor. In: *Flow, Turbulence and Combustion* 98 (2017), 01, Nr. 1, S. 265–282. <http://dx.doi.org/10.1007/s10494-016-9745-2>. – DOI 10.1007/s10494-016-9745-2
- [126] SREENIVASAN, K.R. ; RAGHU, S.: The control of combustion instability: A perspective. In: *Current Science* 79 (2000), Nr. 6, 867–883. <https://www.scopus.com/inward/record.uri?eid=2-s2.0-0039250465&partnerID=40&md5=6c210e0f50702d3ebe8da6f3e36e623f>. – Cited by: 17

- [127] ANSYS, INC.: *Ansys Workbench Meshing User Guide*. Online. <https://www.ansys.com/>. Version: 2023
- [128] PATANKAR, S. V. ; SPALDING, D. B.: A calculation procedure for heat, mass, and momentum transfer in three-dimensional parabolic flow. In: *International Journal of Heat and Mass Transfer* 15 (1972), Nr. 1, S. 787–806
- [129] SIEBER, R.: *Numerische Simulation technischer Strömungen mit Fluid-Struktur-Kopplung*, Technische Universität Darmstadt, Diss., 2002
- [130] NICOL, D. G. ; MALTE, P. C. ; HAMER, A. J. ; ROBY, R. J. ; STEELE, R. C.: Development of a Five-Step Global Methane Oxidation-NO Formation Mechanism for Lean-Premixed Gas Turbine Combustion. In: *Journal of Engineering for Gas Turbines and Power* 121 (1999), 04, Nr. 2, S. 272–280. <http://dx.doi.org/10.1115/1.2817117>. – DOI 10.1115/1.2817117
- [131] KATHROTIA, Trupti ; OSSWALD, Patrick ; NAUMANN, Clemens ; RICHTER, Sandra ; KÖHLER, Markus: Combustion kinetics of alternative jet fuels, Part-II: Reaction model for fuel surrogate. In: *Fuel* 302 (2021), 120736. <http://dx.doi.org/https://doi.org/10.1016/j.fuel.2021.120736>. – DOI <https://doi.org/10.1016/j.fuel.2021.120736>. – ISSN 0016–2361
- [132] CELIK, I. ; GHIA, U. ; ROACHE, P.: Procedure of Estimation and Reporting of Uncertainty Due to Discretization in CFD Application. In: *Journal of Fluids Engineering* 130 (2008), Nr. 7, S. 078001–1–078001–4. <http://dx.doi.org/10.1115/1.4004762>. – DOI 10.1115/1.4004762
- [133] RUMSEY, C. L. ; THOMAS, J. L.: Application of FUN3D and CFL3D to the Third Workshop on CFD Uncertainty Analysis / NASA. 2008 (11). – Forschungsbericht. – Techn. Ber.
- [134] TECPLOT, INC.: *Tecplot 360*. 2023r1. Bellevue WA 98015: Tecplot, Inc., 2023. <https://www.tecplot.com/products/tecplot-360/#docs>
- [135] LEE, J.G. ; SANTAVICCA, D.A.: Experimental diagnostics for the study of combustion instabilities in lean premixed combustors. In: *Journal of Propulsion and Power* 19 (2003), Nr. 5, S. 735–750
- [136] XIANG, L. ; JIANG, H. ; REN, F. ; CHU, H. ; WANG, P.: Numerical study of the physical and chemical effects of hydrogen addition on laminar premixed combustion characteristics of methane and ethane. In: *International Journal of Hydrogen Energy* 45 (2020), 08, Nr. 39, S. 20501–20514. <http://dx.doi.org/10.1016/J.IJHYDENE.2019.11.040>. – DOI 10.1016/J.IJHYDENE.2019.11.040

Appendix

A.1 Parameter file structure

A.1.1 Parameter file for phase 6

PREPROCESSING

Files/IO -----: -
Restart-data prefix: Results/HF1_v005-m045-op10-DC1S30N18.5
Primary grid filename: Grids/HF1_v005-m045.grid
Grid prefix: Grids/Dualgrids/HF1_v005-m045.grid
Output files prefix: Results/HF1_v005-m045-op10-DC1S30N18.6
Boundary mapping filename: Inputs/HF1_v005-m045-op10-adiabatic.bmap
Automatic parameter update (0/1): 0
Output initial field (0/1): 0
Include time stamp in file name (0/1): 0
Enable logfile output on all domains (0/1): 0

Preprocessing -----: -
Number of domains: 1024
Number of multigrid levels: 5
Cache-coloring (0/max_faces in color): 200000
Output level: 5
Point fusing reward: 1.4
Structured grid coarsening: 0.5
Preprocessing for incompressible solver (0/1): 1

SOLVER

Computational quantities -----: -
Discretization scheme for momentum (UDS/CDS/LUDS/QUDS): QUDS
Use gradient limiter for momentum (0/1): 1
NVD blending factor for momentum equations (0.-0.5): 0.4
4th order dissipation scaling factor (0.-1.): 0
Time discretization scheme (Steady/EU_E/EU_I/TPB/CN): Steady
Use LDU decomposition (0/1): 0
Degree of stabilization: 1
Velocity pressure coupling method (Projection/SIMPLE): SIMPLE
Pressure multigrid type (STD/PFM/AMG): PFM

Timestepping Start/Stop -----: -
Output period: 10000

SIMPLE -----: -
Max no of SIMPLE iterations: 170000 #
Under-relaxation factor for momentum equation: 0.7

A.1. PARAMETER FILE STRUCTURE

```
Under-relaxation factor for pressure equation: 0.3
Unsteady SIMPLE exit criterion (0/1/2): 0
Use extended Laplace operator (0/1): 1

Pressure equation solver -----: -
    Type of solver for pressure equation: FGMRES
    GMRES restart length for pressure solver: 20 #only if GMRES is chosen!
    Maximal number of iterations for pressure solver: 20
    Minimum number of iterations for pressure solver: 2
        Epsilon for pressure solver: 0.01
    Stopping criterion for pressure solver (0/1): 0
        Preconditioning of pressure solver: MG
        MG description filename for pressure solver: v5+
    Use linear interpolation for MG pressure solver (0/1): 1
    Under-relaxation factor for MG pressure smoother: 0.9
    Averaging parameter value for MG pressure solver: 1.2
    Max. number of iterations for coarse grid pressure solver: -1
    Min. number of iterations for coarse grid pressure solver: -1
        Epsilon for coarse grid pressure solver: -1
    Type of solver for coarse grid pressure equation: BCGS
Momentum equation solver -----: -
    Type of solver for momentum equation: BCGS
    GMRES restart length for momentum solver: 50 #only if GMRES is chosen!
    Maximal number of iterations for momentum solver: 50
    Minimum number of iterations for momentum solver: 2
        Epsilon for momentum solver: 0.01
    Stopping criterion for momentum solver (0/1): 0
        Preconditioning of momentum solver: Jacobi
        MG description filename for momentum solver: sg
Scalar equation solver -----: -
    Type of solver for scalar equation: BCGS
    GMRES restart length for scalar solver: 50 #only if GMRES is chosen!
    Maximal number of iterations for scalar solver: 50
    Minimum number of iterations for scalar solver: 2
        Epsilon for scalar solver: 0.01
    Stopping criterion for scalar solver (0/1): 0
        Preconditioning of scalar solver: Jacobi
        MG description filename for scalar solver: sg
Reference quantities -----: -
    Reference density: 0.615 ### initial solution with air at T=571K,
    Reference velocities: 0 0 50
    Reference pressure: 101325
    Reference viscosity: 1.82e-05
    Reference point coordinates: 0 0 0
Optional output parameters -----: -
### List of monitoring variables: all,TEMP
### Coordinates for monitoring point(s): (none)
Write header in monitor/residual files (Gen/Xmgr): Xmgr
    Field output values: (none)
    Surface output values: yplus
Write starting/final residuals to file (0/1/2): 1
    Add residuals of scalar equations (0/1): 1
    Calculate adaptation indicator (0/1): 0
    Starting time for statistics computation: -1
    List of averaged quantities: (none)
    List of fluctuation quantities: (none)
-----
MODELS
-----
Activated models -----: -
    Names of models to use: STD_KOM SPC_TRA AUX_VARS SPC_DIF COM_FRC
    Turbulence equation solver -----: -
    Under-relaxation factor for turbulence equation: 0.4
    Discretization scheme for turbulence (UDS/CDS/LUDS/QUDS): QUDS
```

```

Use gradient limiter for turbulence quantities (VENK/NVD): VENK
  NVD blending factor for turbulent quantities (0.-0.5): 0.4
    Output level for turbulence (0/1): 1
      SST version: 2003
        Species transport equation solver -----: -
          Under-relaxation factor for species equations: 0.2
Discretization scheme for species equations (UDS/CDS/LUDS/QUDS): QUDS
  Use gradient limiter for species quantities (VENK/NVD): VENK
    NVD blending factor for species quantities (0.-0.5): 0.4
      Chemistry filename: Kinetics/DLRconcisev1/DC1S30N18_ThetaCOM-1atm.frc
        Reference species (O2 N2 ...): O2 N2
          Reference mass fractions: 0.23 0.77
            Calculate heat release (0/1): 1
Heat radiation model -----: -
  Heat radiation species (CO2 ... SOOT): CO2 H2O
  Auxiliary variables parameters -----: -
    Calculate heat release (0/1): 1
    Write global heat release to file (0/1): 1

```

A.1.2 Boundary mapping file

```

-----
BOUNDARY MAPPING
-----

```

```

Use Theta (0/1): 1
# Marker information for Grids/HF1_v005-m045.uns
#Marker      Name                # of s. elements
# 4          INLET_AIR          1799
# 5          INLET_FUEL         132
# 6          OUTLET             3070
# 7          WALLS_T_AIR        4908
# 8          WALLS_T_FUEL       2490
# 9          WALLS_ADIABATIC     1844
# 10         WALLS_ISOLATION     62393
# 11         WALLS_GLASS        69492
# --- AIR INFLOW ---
      Type: inflow
      Name: INLET_AIR
      Markers: 4
      Velocity: 0 0 0
      Mass flux: 4.010000e-03 # op10
      Turb. degree: 0.01
      Turb. length scale: 0.005
      Temperature: 573
      Species: O2 N2
      Mass fractions: 0.23 0.77
Write surface data (0/1): 1
block end
# --- FUEL INFLOW ---
      Type: inflow
      Name: INLET_FUEL
      Markers: 5
      Velocity: 0 0 0
      Mass flux: 0.086667e-03 # op10, phi ~ 0.74, lambda ~ 1.35, Pth ~ 10.5 kW
      Turb. degree: 0.01
      Turb. length scale: 0.001
      Temperature: 373 # calculated from measurements with Helium
      Species: H2
      Mass fractions: 1.000000
Write surface data (0/1): 1
block end
# --- OUTFLOW ---

```

A.1. PARAMETER FILE STRUCTURE

```

                Type: outflow
                Name: OUTLET
                Markers: 6
Write surface data (0/1): 1
block end
# --- INNER WALLS OF THE AIR CHANNEL ---
                Type: wall
                Name: WALLS_T_AIR
                Markers: 7
                Subtype: turbulent
                Thermal type: isotherm
                Temperature: 573
Write surface data (0/1): 1
block end
# --- (OUTER) WALLS OF THE FUEL CHANNEL (TUBE) ---
                Type: wall
                Name: WALLS_T_FUEL
                Markers: 8
                Subtype: turbulent
                Thermal type: isotherm
                Temperature: 573
Write surface data (0/1): 1
block end
# --- "BASE PLATE" OF THE COMBUSTION CHAMBER ---
                Type: wall
                Name: WALLS_ADIABATIC
                Markers: 9
                Subtype: turbulent
                Thermal type: fixed flux
                Heat flux: 0
Write surface data (0/1): 1
block end
# --- ISOLATED OUTER WALLS OF THE AIR CHANNEL ---
                Type: wall
                Name: WALLS_ISOLATION
                Markers: 10
                Subtype: turbulent
                Thermal type: fixed flux
                Heat flux: 0 # adiabatic wall
Write surface data (0/1): 1
block end
# --- QUARTZ GLASS "WINDOWS" (WALLS OF THE COMBUSTION CHAMBER) ---
                Type: wall
                Name: WALLS_GLASS
                Markers: 11
                Subtype: turbulent
                Thermal type: fixed flux
                Heat flux: 0 # adiabatic wall
Write surface data (0/1): 1
block end
```

A.2 Contour plots

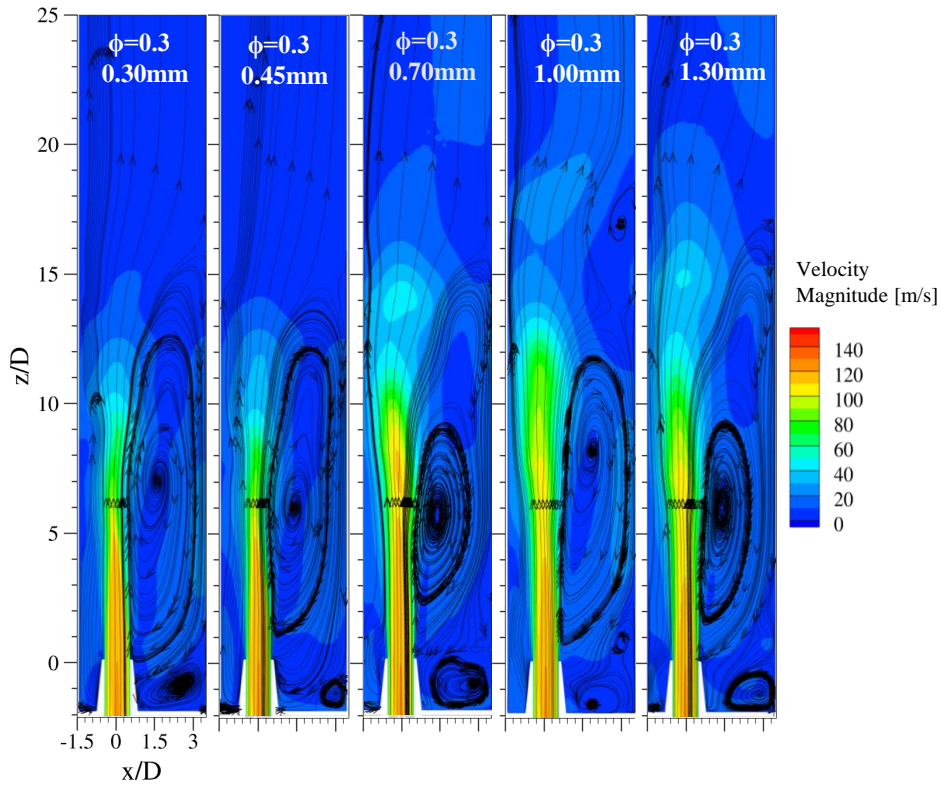


Figure A.1: Flow field characteristics in TP configuration, showcasing different mesh resolutions for the 100 vol.% H_2 and $\Phi = 0.3$ scenario.

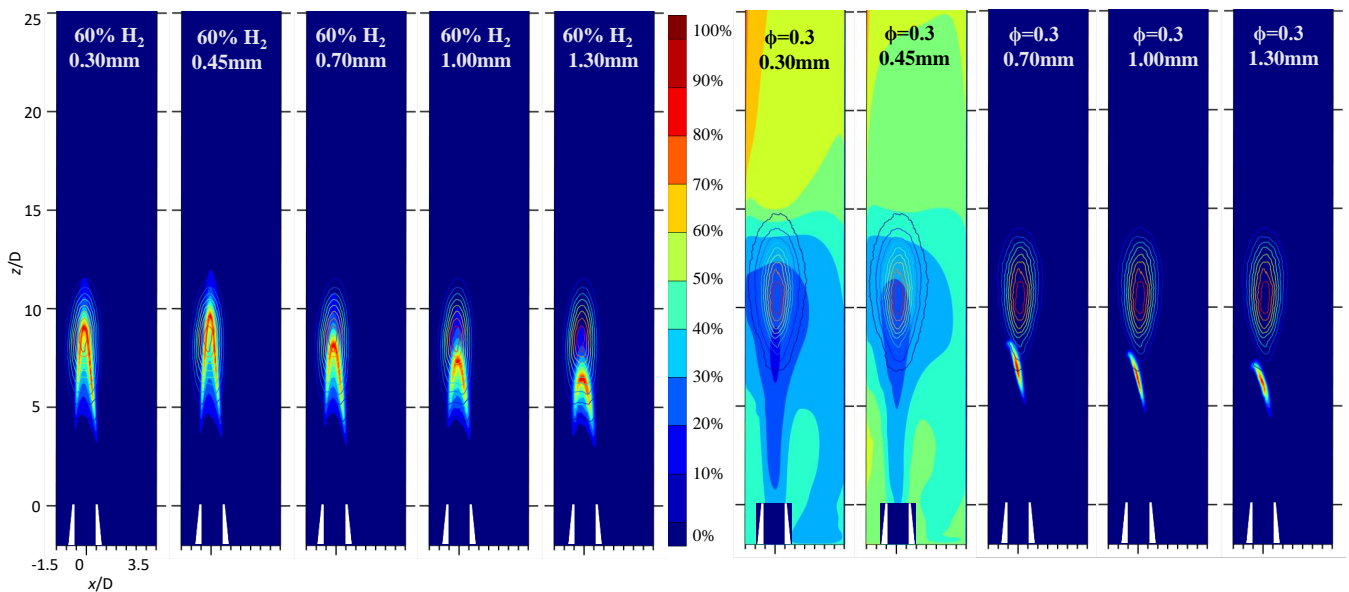


Figure A.2: OH^* -CL visualisation for TP configuration (60vol.% H_2 on left and 100vol.% H_2 on right) across different mesh resolutions. LOH of the experimental results are compared with simulations. The fines meshes are unable to model LOH for leaner conditions.

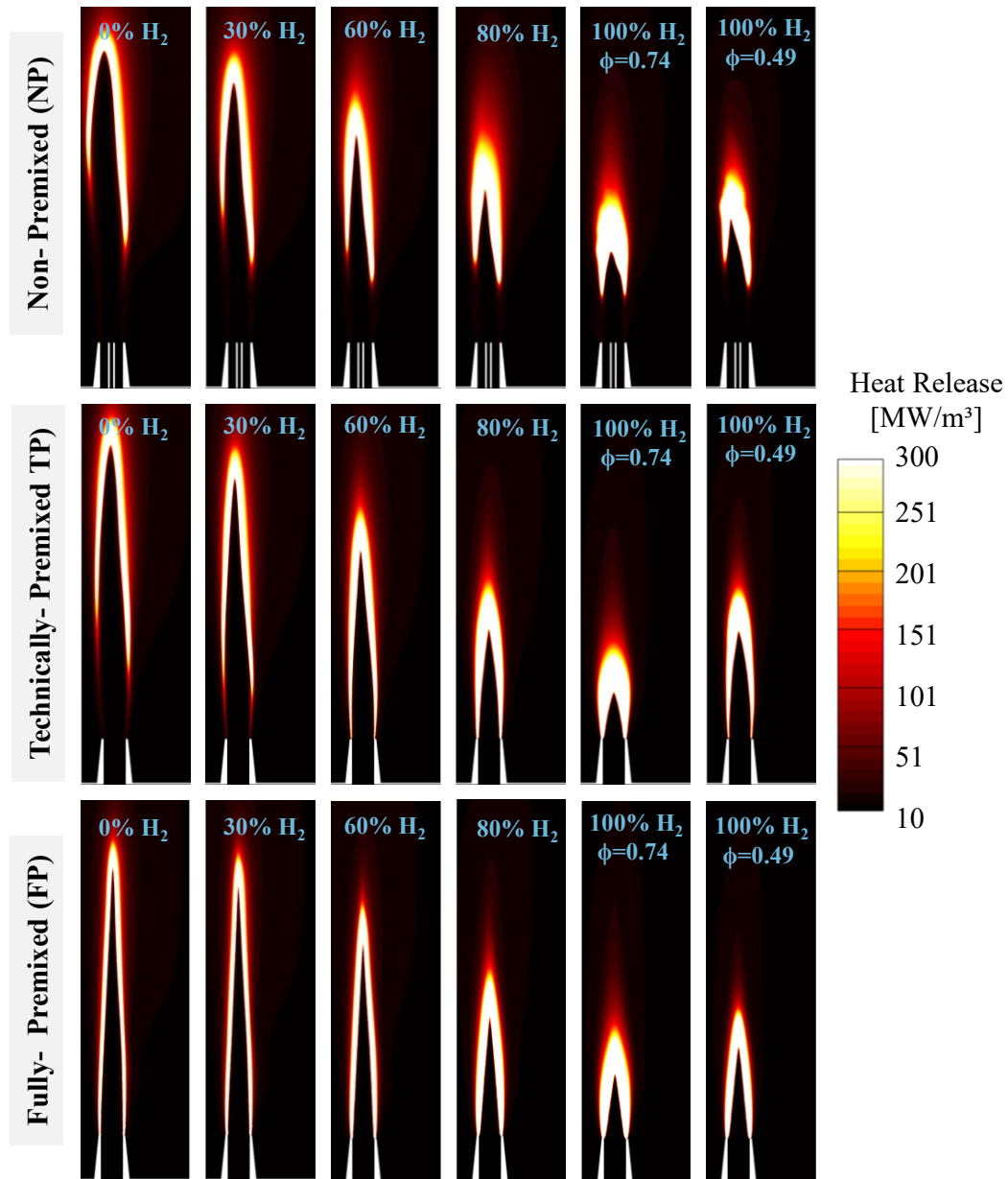


Figure A.3: Contours of heat release in NP, TP, and FP configurations under FF and LF investigations.

Heat release contours for different burner configurations and hydrogen levels complement the temperature distribution insights from the subsection 5.4. These contours reveal the combustion intensity and flame stability.

For the NP configuration, increasing hydrogen shows a higher and more focused heat release, transitioning from a broad methane flame to a concentrated hydrogen flame. The TP configuration displays a steady and balanced heat release, while the FP configuration exhibits intense combustion close to the nozzle, reflecting the immediate reaction due to full premixing. At the lower equivalence ratio of 0.49, the heat release is more spread out, indicating lean mixtures and unstable combustion, aligning with the high LOH and flame instability observed.

A.3 Tecplot macros

A.3.1 Post-processing script for NO_x emissions

```

1  #!MC 1410
2  #working with MOLE FRACTIONS (ThetaCOM uses "X" to designate mole
   fractions)
3  #The command $ frcpost is needed to convert mole fractions into mass
   fractions
4  # NOx (NO and NO2) mole fraction:
5  $!AlterData
6     IgnoreDivideByZero = Yes
7     Equation = '{XNOx} = {XNO} + {XNO2}'
8  # dry values (mole fractions):
9  $!AlterData
10     IgnoreDivideByZero = Yes
11     Equation = '{XNOx_dry} = {XNOx} / (1-{XH2O})'
12 $!AlterData
13     IgnoreDivideByZero = Yes
14     Equation = '{XCO_dry} = {XCO} / (1-{XH2O})'
15 $!AlterData
16     IgnoreDivideByZero = Yes
17     Equation = '{XO2_dry} = {XO2} / (1-{XH2O})'
18 # emissions calculated from dry mole fractions:
19 # (numerator of correction factor: 0.0595 = 0.2095 - 0.1500)
20 $!AlterData
21     IgnoreDivideByZero = Yes
22     Equation = '{XNOx_15} = {XNOx_dry} * 0.0595/(0.2095-{XO2_dry})'
23 $!AlterData
24     IgnoreDivideByZero = Yes
25     Equation = '{XCO_15} = {XCO_dry} * 0.0595/(0.2095-{XO2_dry})'
26 # For comparison purposes, "Massflow-Weighted Average" integral is
   recommended (e.g. at the outlet of the CFD geometry), yielding a "NOx
   in ppm"-style value with 1e-6 corresponding to 1 ppm, e.g. for
   comparison against measurement results from experiments:
27 # (... as opposed to using Tecplot's "Mass-Weighted Flow Rate"
   integration mode when working with mass fractions ("Y...")!)
28 # [ Set Field Variables in Tecplot: x_velocity (6), y_velocity (7),
   z_velocity (8), density (4) ]
29 $!ExtendedCommand
30 CommandProcessorID = 'CFDAnalyzer4'
31 Command = 'SetFieldVariables ConvectionVarsAreMomentum=\`F\` UVarNum=6
   VVarNum=7 WVarNum=8 ID1=\`Density\` Variable1=4 ID2=\`NotUsed\`
   Variable2=0'
32 # [ Perform Integration: ]
33 $!ExtendedCommand
34 CommandProcessorID = 'CFDAnalyzer4'
35 Command = 'Integrate [6] VariableOption=\`MassFlowWeightedAverage\`
   XOrigin=0 YOrigin=0 ZOrigin=0 ScalarVar=129 Absolute=\`F\`
   ExcludeBlanked=\`F\` XVariable=1 YVariable=2 ZVariable=3
   IntegrateOver=\`Cells\` IntegrateBy=\`Zones\` IRange={MIN =1 MAX = 0
   SKIP = 1} JRange={MIN =1 MAX = 0 SKIP = 1} KRange={MIN =1 MAX = 0
   SKIP = 1} PlotResults=\`F\` PlotAs=\`Result\` TimeMin=0 TimeMax=0'
36 # [ Save Integration Result to text file: ]
37 $!ExtendedCommand
38 CommandProcessorID = 'CFDAnalyzer4'
39 Command = 'SaveIntegrationResults FileName=\`you file name.txt\`

```

A.3.2 Line of sight integration to visualize OH*-CL

```

1  $!NewLayout
2  # spatial limits for LoS integration, in "m"
3  $!VarSet |x_lo| = -0.015
4  $!VarSet |x_hi| = 0.035
5  $!VarSet |y_lo| = -0.020
6  $!VarSet |y_hi| = 0.020
7  $!VarSet |z_lo| = -0.020
8  $!VarSet |z_hi| = 0.300
9  # spatial discretization for each dimension, in "cells per mm"
10 $!VarSet |disc_x| = 2
11 $!VarSet |disc_y| = 2
12 $!VarSet |disc_z| = 2
13 # Values for IMax, JMax and KMax of the rectangular zone, "+1" is needed
    against the "fencepost error"
14 $!VarSet |rect_IMax| = ( ( 1000 * ( |x_hi| - |x_lo| ) * |disc_x| ) + 1 )
15 $!VarSet |rect_JMax| = ( ( 1000 * ( |y_hi| - |y_lo| ) * |disc_y| ) + 1 )
16 $!VarSet |rect_KMax| = ( ( 1000 * ( |z_hi| - |z_lo| ) * |disc_z| ) + 1 )
17 #
18 $!VarSet |PerformInterpolation| = 1
19 $!VarSet |PerformLoSIntegration| = 1
20 #
21 $!VarSet |currentscriptpath| = "/home/plan_ka/ws_register/scratch/
    plan_ka-THETA-ws_230109/H2FLOX1D/v004/Results/_tecplot/"
22 $!VarSet |ResultsRelativePath| = "../HF1_v005-m045-op10-DC1S30N18.6/"
23 $!VarSet |ResultNamePrefix| = "HF1_v005-m045-op10-DC1S30N18.6.pval
    .200000"
24 $!IF |PerformInterpolation| == 1
25   $!ReadDataSet '|currentscriptpath||ResultsRelativePath||
    ResultNamePrefix|.plt'
26     ReadDataOption = New
27     ResetStyle = Yes
28     VarLoadMode = ByName
29     AssignStrandIDs = Yes
30     VarNameList = '"X" "Y" "Z" "Y0" "YH"'
31   $!AlterData [1-2]
32     Equation = '{YOH_mult} = {Y0} * {YH}'
33   $!CreateRectangularZone
34     IMax = |rect_IMax|
35     JMax = |rect_JMax|
36     KMax = |rect_KMax|
37     X1 = |x_lo|
38     X2 = |x_hi|
39     Y1 = |y_lo|
40     Y2 = |y_hi|
41     Z1 = |z_lo|
42     Z2 = |z_hi|
43     XVar = 1
44     YVar = 2
45     ZVar = 3
46   $!LinearInterpolate
47     SourceZones = [1-2]
48     DestinationZone = 11
49     VarList = [6]
50     LinearInterPConst = 0
51     LinearInterpMode = DontChange
52   $!WriteDataSet "|currentscriptpath||ResultNamePrefix|-rect2.plt"

```

```

53     IncludeText = No
54     IncludeGeom = No
55     IncludeCustomLabels = No
56     IncludeDataShareLinkage = Yes
57     AssociateLayoutWithDataFile = No
58     VarList = [1-6]
59     Binary = Yes
60     UsePointFormat = No
61     Precision = 9
62     TecplotVersionToWrite = TecplotCurrent
63 $!ENDIF
64 $!IF |PerformInterpolation| == 0
65     $!IF |PerformLoSIntegration| == 1
66         $!ReadDataSet '|currentscriptpath||ResultNamePrefix|-rect2.plt'
67         ReadDataOption = New
68         ResetStyle = Yes
69         VarLoadMode = ByName
70         AssignStrandIDs = Yes
71         VarNameList = 'X" "Y" "Z" "YO" "YH" "YOH_mult'
72     $!ENDIF
73 $!ENDIF
74 $!IF |PerformLoSIntegration| == 1
75     # LoS integration of variable "YOH_mult"
76     $!ExtendedCommand
77         CommandProcessorID = 'CFDAnalyzer4'
78         Command = 'Integrate [11] VariableOption=\`Scalar\` XOrigin=0
YOrigin=0 ZOrigin=0 ScalarVar=6 Absolute=\`F\` ExcludeBlanked=\`F\`
XVariable=1 YVariable=2 ZVariable=3 IntegrateOver=\`JLines\`
IntegrateBy=\`Zones\` IRange={MIN =1 MAX = 0 SKIP = 1} JRange={MIN =1
MAX = 0 SKIP = 1} KRange={MIN =1 MAX = 0 SKIP = 1} PlotResults=\`T\`
PlotAs=\`LoS_YOH_mult\` TimeMin=0 TimeMax=0'
79     $!FrameControl ActivateByNumber
80         Frame = 2
81     $!AlterData
82         Equation = '{X} = |x_lo| + ( |x_hi| - |x_lo| ) / ( |rect_IMax| - 1
) * ( {I} - 1 )'
83     $!AlterData
84         Equation = '{Y} = 0.0'
85     $!AlterData
86         Equation = '{Z} = |z_lo| + ( |z_hi| - |z_lo| ) / ( |rect_KMax| - 1
) * ( {K} - 1 )'
87     $!DeleteVars [5-12]
88     $!WriteDataSet "|currentscriptpath||ResultNamePrefix|-LoS2-YOH_mult
.plt.plt"
89         IncludeText = No
90         IncludeGeom = Yes
91         IncludeCustomLabels = No
92         IncludeDataShareLinkage = Yes
93         AssociateLayoutWithDataFile = No
94         VarList = [1-7]
95         Binary = Yes
96         UsePointFormat = No
97         Precision = 9
98         TecplotVersionToWrite = TecplotCurrent
99 $!ENDIF
100 $!QUIT

```